

**AD-A267 498****DOCUMENTATION PAGE**Form Approved  
OMB No. 0704-0188

ion is estimated to average 1 hour per response, including the time for reviewing instructions, searching existing data sources, gathering and reviewing the collection of information. Send comments regarding this burden estimate or any other aspect of this collection of information, including this burden estimate, to Washington Headquarters Services, Directorate for Information Operations and Reports, 1215 Jefferson Davis Highway, Suite 1204, Arlington, VA 22202-4302, and to the Office of Management and Budget, Paperwork Reduction Project (0704-0188), Washington, DC 20503.

<b>2. REPORT DATE</b> MAY 1993		<b>3. REPORT TYPE AND DATES COVERED</b> THESIS/DISSERTATION	
<b>4. TITLE AND SUBTITLE</b> A Guidance and Navigation System For Two Spacecraft Rendezvous in Translunar Halo Orbit		<b>5. FUNDING NUMBERS</b>	
<b>6. AUTHOR(S)</b> Brian Leigh Jones		<b>8. PERFORMING ORGANIZATION REPORT NUMBER</b> AFIT/CI/CIA- 93-011D	
<b>7. PERFORMING ORGANIZATION NAME(S) AND ADDRESS(ES)</b> AFIT Student Attending: Univ of Texas at Austin		<b>10. SPONSORING / MONITORING AGENCY REPORT NUMBER</b>	
<b>9. SPONSORING / MONITORING AGENCY NAME(S) AND ADDRESS(ES)</b> DEPARTMENT OF THE AIR FORCE AFIT/CI 2950 P STREET WRIGHT-PATTERSON AFB OH 45433-7765		<b>11. SUPPLEMENTARY NOTES</b>	
<b>12a. DISTRIBUTION / AVAILABILITY STATEMENT</b> Approved for Public Release IAW 190-1 Distribution Unlimited MICHAEL M. BRICKER, SMSgt, USAF Chief Administration		<b>12b. DISTRIBUTION CODE</b>	
<b>13. ABSTRACT (Maximum 200 words)</b>			
<b>14. SUBJECT TERMS</b>			
<b>15. NUMBER OF PAGES</b> 176			
<b>16. PRICE CODE</b>			
<b>17. SECURITY CLASSIFICATION OF REPORT</b>	<b>18. SECURITY CLASSIFICATION OF THIS PAGE</b>	<b>19. SECURITY CLASSIFICATION OF ABSTRACT</b>	<b>20. LIMITATION OF ABSTRACT</b>

**93 8 05 144****93-18091**

93-011D

**A GUIDANCE AND NAVIGATION SYSTEM  
FOR TWO SPACECRAFT RENDEZVOUS  
IN TRANSLUNAR HALO ORBIT**

APPROVED BY

DISSERTATION COMMITTEE:

R. Brining  
V. Weber

David G. Hall

Chirald D. Epp

Wallace J. Fowler

DTIC QUALITY INSPECTED 3

Accession For	
NTIS CRA&I	<input checked="checked" type="checkbox"/>
DTIC TAB	<input type="checkbox"/>
Unannounced	<input type="checkbox"/>
Justification	
By	
Distribution /	
Availability Codes	
Dist	Avail and/or Special
A-1	

*To my S. & S. Express*

**A GUIDANCE AND NAVIGATION SYSTEM  
FOR TWO SPACECRAFT RENDEZVOUS  
IN TRANSLUNAR HALO ORBIT**

by

**BRIAN LEIGH JONES, B.S.A.E., M.S.A.E.**

**DISSERTATION**

Presented to the Faculty of the Graduate School of

The University of Texas at Austin

in Partial Fulfillment

of the Requirements

for the Degree of

**DOCTOR OF PHILOSOPHY**

**THE UNIVERSITY OF TEXAS AT AUSTIN**

May, 1993



## Acknowledgments

I would like to first thank my dissertation committee for their collective comments, many suggestions, probing questions and careful review of this research; the end product is much better because of their efforts. I would like to extend my sincere appreciation to Dr. Robert Bishop, my advisor, for his guidance and encouragement throughout this project. His insight, support and patience during the multitudes of questions asked have been invaluable to me. I also wish to thank Dr. David Hull who introduced me to the study of optimal control and who taught me to "think" about the problem solution before blindly applying equations. Additionally, I want to thank Dr. Victor Szebehely for his insightful lectures and exposing me to the beauty of orbital mechanics. Further, I am indebted to Drs. Wallace Fowler and Chirold Epp whose support and good cheer have been a source of enthusiasm and comfort to me. Finally, I would like to thank Dr. Jeff Shamma for several helpful technical discussions.

I haven't the space to mention my colleagues individually, but to each I say thank you! You have had to put up with countless questions and endless hogging of the computers, but your understanding and patience did not go unnoticed. You have been true friends. In addition, my family, extended family, and church family have been a continual source of support and encouragement; they each have "loved" me through the completion of these studies. My heartfelt thanks goes to each of them.

Lastly and most important, to my wife, I thank her for her constant

encouragement, unbounded understanding and limitless love. The completion of this project would not have occurred if not for her moral support. And to my precious little girl who understood only that Daddy had to work a lot, my deepest gratitude is expressed for her unconditional love.

BRIAN LEIGH JONES

*The University of Texas at Austin*

*May, 1993*

**A GUIDANCE AND NAVIGATION SYSTEM  
FOR TWO SPACECRAFT RENDEZVOUS  
IN TRANSLUNAR HALO ORBIT**

Publication No. \_\_\_\_\_

Brian Leigh Jones, Ph.D.

The University of Texas at Austin, 1993

Supervisor: Robert H. Bishop

This research considers the design of a representative end-to-end guidance and navigation system for the terminal phase rendezvous of two spacecraft in the circular restricted three-body problem. It assumes the target vehicle is in a small radius translunar halo orbit; the target vehicle remains passive with respect to the rendezvous profile. The chaser vehicle is in an independent small radius translunar halo orbit and executes all rendezvous maneuvers. First, the halo orbit guidance problem is formulated in the frequency-domain from which an output feedback guidance law is developed using  $\mathcal{H}_2$  control theory. Linear simulation results validate the guidance law and provide data which quantify the effect of control inputs, noise characteristics and halo orbit characteristics

on the steady state halo orbit station-keeping costs. Secondly, a two spacecraft terminal phase rendezvous targeting law is derived; nonlinear simulation results validate the targeting law. Using these results, the three-body terminal phase rendezvous problem is further characterized and contrasted with the two-body problem. Thirdly, a rendezvous navigation filter is constructed to supply the targeting law with chaser vehicle state information. Nonlinear simulation results validate the filter design and provide data to assess the filter performance. Lastly, two rendezvous scenarios are examined to demonstrate the complete system design.

## Table of Contents

<b>Acknowledgments</b>	<b>iv</b>
<b>Abstract</b>	<b>vi</b>
<b>Table of Contents</b>	<b>viii</b>
<b>List of Tables</b>	<b>xii</b>
<b>List of Figures</b>	<b>xiv</b>
<b>List of Symbols</b>	<b>xix</b>
<b>1. Introduction</b>	<b>1</b>
1.1 Research Premise . . . . .	4
1.2 Previous Work . . . . .	6
1.2.1 Halo Orbit Guidance . . . . .	6
1.2.2 Rendezvous Targeting . . . . .	8
1.2.3 Rendezvous Navigation . . . . .	9
1.3 Dissertation Organization . . . . .	10
<b>2. The Circular Restricted Problem of Three-Bodies</b>	<b>12</b>
2.1 Nonlinear Equations of Motion . . . . .	13
2.2 Equilibrium Point Location . . . . .	17
2.3 Linearized Equations of Motion . . . . .	19
2.4 Periodic Orbits . . . . .	21

<b>3. Halo Orbit Guidance Law</b>	<b>25</b>
3.1 Problem Statement . . . . .	25
3.2 System Models . . . . .	28
3.3 State Space $\mathcal{H}_2$ Solution . . . . .	31
3.4 Simulation Results . . . . .	32
3.4.1 State Equation Formulation . . . . .	32
3.4.2 Typical $\mathcal{H}_2$ Guidance Laws . . . . .	33
3.4.3 Control Input Parametric Study . . . . .	38
3.4.4 Noise Characteristics Parametric Study . . . . .	42
3.4.5 Halo Orbit Characteristics Parametric Study . . . . .	44
<b>4. Rendezvous Targeting</b>	<b>47</b>
4.1 State Equations . . . . .	47
4.2 Targeting Law . . . . .	49
4.3 Simulation Results . . . . .	50
4.3.1 $TI$ Targeting Law Error Parametric Study . . . . .	51
4.3.2 Constant Incline Angle Parametric Study . . . . .	54
4.3.3 Constant Transfer Time Parametric Study . . . . .	55
4.3.4 Representative Relative Trajectories . . . . .	58
<b>5. Rendezvous Navigation</b>	<b>62</b>
5.1 Continuous-Discrete Kalman Filter . . . . .	63
5.1.1 Dynamical System . . . . .	63
5.1.2 Propagation and Update Equations . . . . .	65
5.1.3 Measurement-State Relationships . . . . .	68
5.2 Simulation Results . . . . .	75

5.2.1	Navigation Errors Parametric Study . . . . .	79
5.2.2	Final Position Error Sensitivity Parametric Study . . .	84
<b>6.</b>	<b>Applications</b>	<b>87</b>
6.1	Planar Circular Orbit Demonstration . . . . .	88
6.2	$\mathcal{H}_2$ Guided Halo Orbit Demonstration . . . . .	94
<b>7.</b>	<b>Nonlinear Simulation Package</b>	<b>100</b>
7.1	General Capabilities . . . . .	100
7.2	Main Simulation Functional Description . . . . .	102
7.2.1	Target Vehicle Environment Module . . . . .	102
7.2.2	Chaser Vehicle Environment Module . . . . .	107
7.2.3	Proximity Sensor Module . . . . .	109
7.2.4	Rendezvous Navigation Module . . . . .	111
7.2.5	Rendezvous Targeting Module . . . . .	113
7.2.6	Support Modules . . . . .	115
7.3	Pre-Processor Program . . . . .	116
7.4	Post-Processor Program . . . . .	116
<b>8.</b>	<b>Conclusions</b>	<b>120</b>
<b>Appendix A.</b>	<b>State Transition Matrices</b>	<b>123</b>
A.1	Linearized Equations of Motion . . . . .	123
A.2	Rendezvous Targeting Law . . . . .	125
<b>Appendix B.</b>	<b>Halo Orbit Guidance Law Data</b>	<b>129</b>
B.1	Representative $\mathcal{H}_2$ Guidance Law . . . . .	129
B.2	Representative Time Histories . . . . .	130

B.3 Representative Halo Orbits . . . . .	130
B.4 Noise Statistics . . . . .	131
B.5 Halo Orbit Frequency Parametric Study . . . . .	131
B.6 Control Weighting Factors Parametric Study . . . . .	131
<b>Appendix C. Rendezvous Navigation Filter Monte Carlo Data</b>	<b>145</b>
C.1 Individual Error Vector Plots . . . . .	145
C.2 Sensitivity Matrix Data . . . . .	145
<b>Appendix D. Applications Monte Carlo Data</b>	<b>162</b>
D.1 Planar Circular Orbit (Profile 1) . . . . .	162
D.2 Planar Circular Orbit (Profile 2) . . . . .	162
D.3 $\mathcal{H}_2$ Guided Halo Orbit (Profile 1) . . . . .	162
D.4 $\mathcal{H}_2$ Guided Halo Orbit (Profile 2) . . . . .	162
<b>Bibliography</b>	<b>171</b>
<b>Vita</b>	<b>177</b>



## List of Tables

2.1	Appropriate Signs for Collinear Equilibrium Points . . . . .	18
2.2	Equilibrium Point Locations . . . . .	19
3.1	Simulation Noise Statistics . . . . .	34
3.2	$\Delta V_{TOT}$ Comparison . . . . .	35
3.3	Three vs. Two Axes Control . . . . .	38
3.4	$\xi$ vs. $\eta$ Axis Control . . . . .	39
5.1	Measurement - State Relationships . . . . .	75
5.2	Parameters used by Measurement - State Relationships . . . .	76
6.1	Propulsion Requirements Summary . . . . .	91
6.2	Final Miss Distance Summary . . . . .	94
7.1	Pre-Processor Program Main Menu . . . . .	117
7.2	Post-Processor Program Main Menu . . . . .	119
D.1	Planar Circular Orbit Propulsion Requirement (IC=46.08 deg, INC=22.85 deg, TT=9 hrs) . . . . .	163
D.2	Planar Circular Orbit Final Miss Distance (IC=46.08 deg, INC=22.85 deg, TT=9 hrs) . . . . .	164

D.3 Planar Circular Orbit Propulsion Requirements (IC=180.00 deg, INC=22.85 deg, TT=9 hrs) . . . . .	165
D.4 Planar Circular Orbit Final Miss Distance (IC=180.00 deg, INC=22.85 deg, TT=9 hrs) . . . . .	166
D.5 $\mathcal{H}_2$ Guided Halo Orbit Propulsion Requirements (IC=46.08 deg, TT=9 hrs) . . . . .	167
D.6 $\mathcal{H}_2$ Guided Halo Orbit Final Miss Distance (IC=46.08 deg, TT=9 hrs) . . . . .	168
D.7 $\mathcal{H}_2$ Guided Halo Orbit Propulsion Requirements (IC=180.00 deg, TT=9 hrs) . . . . .	169
D.8 $\mathcal{H}_2$ Guided Halo Orbit Final Miss Distance (IC=180.00 deg, TT=9 hrs) . . . . .	170

## List of Figures

1.1	Telecommunications Satellite in Translunar Halo Orbit . . . . .	3
1.2	System Design Continuum . . . . .	4
1.3	Rendezvous Scenario . . . . .	5
2.1	Force Diagram : . . . . .	14
2.2	Equilibrium Point Locations . . . . .	20
2.3	Uncontrolled Periodic Orbit . . . . .	24
3.1	$\mathcal{H}_2$ System Model . . . . .	26
3.2	Desired System Model . . . . .	28
3.3	Expanded System Model . . . . .	29
3.4	Halo Orbit Geometry (Zero Noise) . . . . .	36
3.5	Halo Orbit Geometry ( $3\sigma$ Noise) . . . . .	37
3.6	Representative Example Block Diagram . . . . .	39
3.7	Control Acceleration Transfer Function ( $\frac{u}{r_\eta}$ ) for the Three and Two Axes Control Example . . . . .	40
3.8	Closed-Loop Transfer Function ( $\frac{\eta}{r_\eta}$ ) for the Three and Two Axes Control Example . . . . .	41
3.9	Effect of Noise on Halo Orbit Station-keeping Cost . . . . .	43

3.10 Effect of Increasing Frequency on Halo Orbits with Clockwise Orbital Rotation . . . . .	45
4.1 Incline and Initial Condition Angle Definitions . . . . .	51
4.2 <i>TI</i> Targeting Law Error . . . . .	53
4.3 Midcourse Correction Maneuver Placement . . . . .	54
4.4 Constant Incline Angle Characteristics . . . . .	56
4.5 Constant Transfer Time Characteristics . . . . .	57
4.6 Representative Relative Motion . . . . .	59
4.7 Relative Trajectory Torsion and Rate of Change of Torsion at Terminal Phase Rendezvous Initiation . . . . .	60
5.1 Angle Measurements . . . . .	71
5.2 Computed Angles . . . . .	72
5.3 Position Error Vectors for Monte Carlo Analysis . . . . .	77
5.4 Velocity Error Vectors for Monte Carlo Analysis . . . . .	78
5.5 Average Chaser Vehicle State Estimation Error . . . . .	80
5.6 Covariance Position Error Ellipsoid Magnitude and Orientation	82
5.7 Covariance Velocity Error Ellipsoid Magnitude and Orientation	83
5.8 Sensitivity Matrix Largest Singular Value . . . . .	85
6.1 Planar Circular Orbit Reference Relative Trajectory (IC=46.08 deg, INC=22.85 deg, TT=9 hrs) . . . . .	89

6.2	Planar Circular Orbit Reference Relative Trajectory (IC=180.00 deg, INC=22.85 deg, TT=9 hrs) . . . . .	90
6.3	Planar Circular Orbit Average Chaser Vehicle State Estimation Error (IC=46.08 deg, INC=22.85 deg, TT=9 hrs) . . . . .	92
6.4	Planar Circular Orbit Average Chaser Vehicle State Estimation Error (IC=180.00 deg, INC=22.85 deg, TT=9 hrs) . . . . .	93
6.5	$\mathcal{H}_2$ Guided Halo Orbit Reference Relative Trajectory (IC=46.08 deg, TT=9 hrs) . . . . .	95
6.6	$\mathcal{H}_2$ Guided Halo Orbit Reference Relative Trajectory (IC=180.00 deg, TT=9 hrs) . . . . .	96
6.7	$\mathcal{H}_2$ Guided Halo Orbit Average Chaser Vehicle State Estima- tion Error (IC=46.08 deg, TT=9 hrs) . . . . .	98
6.8	$\mathcal{H}_2$ Guided Halo Orbit Average Chaser Vehicle State Estima- tion Error (IC=180.00 deg, TT=9 hrs) . . . . .	99
7.1	Guidance and Navigation System Functional Description . . .	103
7.2	$\mathcal{H}_2$ Guided Halo Orbit Trajectories . . . . .	104
7.3	Planar Circular Orbit Trajectories . . . . .	105
7.4	Target Vehicle Environment Functional Description . . . . .	106
7.5	Chaser Vehicle Environment Functional Description . . . . .	108
7.6	Proximity Sensor Functional Description . . . . .	110
7.7	Rendezvous Navigation Functional Description . . . . .	112
7.8	Rendezvous Targeting Functional Description . . . . .	114

B.1	Steady State Position and Velocity . . . . .	132
B.2	Position and Velocity Estimation Error . . . . .	133
B.3	Steady State Control Acceleration . . . . .	134
B.4	Halo Orbit Geometry as a Function of Noise . . . . .	135
B.5	Halo Orbit Orientation as a Function of Noise . . . . .	136
B.6	Noise Statistics . . . . .	137
B.7	Halo Orbit Geometry as a Function of Frequency . . . . .	138
B.8	Halo Orbit Orientation as a Function of Frequency . . . . .	139
B.9	Velocity Required in the $\xi$ -Axis . . . . .	140
B.10	Velocity Required in the $\zeta$ -Axis . . . . .	141
B.11	Total Velocity Required . . . . .	142
B.12	$\rho_\eta$ Parametric Study . . . . .	143
B.13	$\rho_\zeta$ Parametric Study . . . . .	144
C.1	Chaser Vehicle State Estimation Error (Error Vector 1) . . . . .	146
C.2	Chaser Vehicle State Estimation Error (Error Vector 2) . . . . .	147
C.3	Chaser Vehicle State Estimation Error (Error Vector 3) . . . . .	148
C.4	Chaser Vehicle State Estimation Error (Error Vector 4) . . . . .	149
C.5	Chaser Vehicle State Estimation Error (Error Vector 5) . . . . .	150
C.6	Chaser Vehicle State Estimation Error (Error Vector 6) . . . . .	151
C.7	Chaser Vehicle State Estimation Error (Error Vector 7) . . . . .	152
C.8	Chaser Vehicle State Estimation Error (Error Vector 8) . . . . .	153

C.9 Chaser Vehicle State Estimation Error (Error Vector 9) . . . .	154
C.10 Chaser Vehicle State Estimation Error (Error Vector 10) . . .	155
C.11 Chaser Vehicle State Estimation Error (Error Vector 11) . . .	156
C.12 Chaser Vehicle State Estimation Error (Error Vector 12) . . .	157
C.13 Chaser Vehicle State Estimation Error (Error Vector 13) . . .	158
C.14 Final Position Error Sensitivity to a Change in Downtrack Ve- locity . . . . .	159
C.15 Final Position Error Sensitivity to a Change in Out-of-Plane Velocity . . . . .	160
C.16 Final Position Error Sensitivity to a Change in Radial Velocity	161

## List of Symbols

### English Symbols

$A_a$	= Unmodeled accelerations dynamics
$A_b$	= Measurement biases dynamics
$A_G, B_G, C_G, D_G$	= State space realization of the linearized equations of motion
$A_K, B_K, C_K, D_K$	= State space realization of the $\mathcal{H}_2$ guidance law
$A_p$	= Target vehicle dynamics
$A, B_1, B_2, C_1, C_2, D_{11}, D_{12}, D_{21}, D_{22}$	= State Space realization of the $\mathcal{H}_2$ system plant
$a$	= Distance from the barycenter to the Moon, m
$\mathbf{a}$	= Unmodeled accelerations on the chaser vehicle
$\mathbf{a}_S$	= Internal propulsion acceleration vector, $\frac{\text{m}}{\text{sec}^2}$
$a_x, a_y, a_z$	= Dimensional components of the internal propulsion acceleration vector, $\frac{\text{m}}{\text{sec}^2}$
$b$	= Rendezvous navigation filter measurement biases
$b$	= Distance from the barycenter to the Earth, m
$C_1, C_2, C_3, C_4, C_5$	= Constant vectors
$C_1, C_2, C_3, C_4$	= Constants of integration
$e$	= $\mathcal{H}_2$ guidance law error vector
$F$	= Rendezvous navigation filter partial derivative matrix
$F_E$	= Gravitational attraction of the Earth, N
$F_{\mathcal{H}_2}$	= $\mathcal{H}_2$ state feedback gain matrix



$F_l$	= Lower linear fractional transformation
$F_M$	= Gravitational attraction of the Moon, N
$F_p$	= Control force generated by internal propulsion, N
$f$	= Non-dimensional frequency of halo orbit
$f_1, f_2$	= Nonlinear equations of motion
$G$	= Linearized system plant
$G_x$	= Linearized system plant dynamics
$G_r$	= Gravitational constant, $\frac{m^3}{kg \text{ sec}^2}$
$g$	= Gravity, $\frac{m}{\text{sec}^2}$
$g_1$	= Nonlinear control function
$H_k$	= Rendezvous navigation filter measurement partial derivative matrix
$h_1, h_2$	= Rendezvous navigation filter measurement-state relationships
$I$	= Identity matrix
IC	= Initial condition
INC	= Incline angle
$I_{sp}$	= Specific impulse, sec
$\hat{i}_I, \hat{j}_I, \hat{k}_I$	= Inertial coordinate frame
$\hat{i}_R, \hat{j}_R, \hat{k}_R$	= Rotating coordinate frame
$\hat{i}_S, \hat{j}_S, \hat{k}_S$	= Sensor coordinate frame
$J$	= Linear Quadratic Gaussian performance index
$K_{halo}$	= $\mathcal{H}_2$ guidance law
$K_k$	= Rendezvous navigation filter Kalman gain matrix
$L_{\mathcal{H}_2}$	= $\mathcal{H}_2$ observer gain matrix

$L_1, L_2, L_3, L_4, L_5$	= Earth-Moon equilibrium points
LVIR	= Local vertical inertial rectangular
MCC	= Midcourse correction
$m_E$	= Mass of the Earth, kg
$m_M$	= Mass of the Moon, kg
$m_S$	= Mass of the third body, kg
$n$	= Mean motion, $\frac{\text{rad}}{\text{sec}}$
$P$	= Rendezvous navigation filter error covariance matrix
$P_G$	= $\mathcal{H}_2$ system plant
$Q$	= Rendezvous navigation filter process noise fixed power spectrum
$Q_a$	= Unmodeled accelerations fixed power spectrum
$Q_b$	= Measurement biases fixed power spectrum
$Q_{LQG}$	= Linear Quadratic Gaussian weighting matrix
$R$	= Relative position vector
$R$	= Relative range measurement
$\dot{R}$	= Relative range rate measurement
$R_k$	= Rendezvous navigation filter measurement noise covariance matrix
RCS	= Reaction control system
$r$	= $\mathcal{H}_2$ guidance law reference input
$r_c$	= Chaser vehicle position vector
$r_{ES}$	= Position of the third body with respect to the Earth, m
$r_{MS}$	= Position of the third body with respect to the

	Moon, m
$r_s$	= Position of the third body with respect to the barycenter, m
$r_t$	= Target vehicle position vector
$T_{BL}$	= Transformation matrix from the LVIR coordinate frame to the body coordinate frame
TIG	= Time-of-ignition
$T_{IL}$	= Transformation matrix from the LVIR coordinate frame to the inertial coordinate frame
$T_{LI}$	= Transformation matrix from the inertial coordinate frame to the LVIR coordinate frame
$T_{SB}$	= Transformation matrix from the body coordinate frame to the sensor coordinate frame
TT	= Transfer time
$T_{zw}$	= Closed loop transfer function between regulated variables and exogenous inputs
TI	= Terminal phase initiation
TF	= Terminal phase final
$t$	= Non-dimensional time
$t^*$	= Dimensional time, sec
$t_1$	= Non-dimensional time of rendezvous initiation
$t_2$	= Non-dimensional time of rendezvous
$U$	= Non-dimensional internal propulsion acceleration vector
$U_x, U_y, U_z$	= Non-dimensional components of the internal

	propulsion acceleration vector
$u$	= Non-dimensional linearized internal propulsion acceleration vector
$u_\xi, u_\eta, u_\zeta$	= Non-dimensional components of the linearized internal propulsion acceleration vector
$V$	= Relative velocity vector
$v$	= Rendezvous navigation filter measurement noise
$v_c$	= Chaser vehicle velocity vector
$v_t$	= Target vehicle velocity vector
$w_2$	= $\mathcal{H}_2$ guidance law exogenous inputs
$w$	= Rendezvous navigation filter process noise
$w_a$	= Unmodeled accelerations process noise
$w_b$	= Measurement biases process noise
$w_d$	= $\mathcal{H}_2$ guidance law plant disturbances
$w_m$	= $\mathcal{H}_2$ guidance law measurement noise
$w_o$	= Initial spacecraft weight, lbs
$w_p$	= Weight of propellant consumed, lbs
$X$	= Non-dimensional state vector of the third body in the rotating coordinate system
$X_K$	= $\mathcal{H}_2$ guidance law states
$X_2$	= $\mathcal{H}_2$ solution to state feedback Ricatti equation
$XL, YL, ZL$	= Non-dimensional components of the third body position vector in the LVIR coordinate frame
$x, y, z$	= Non-dimensional components of the third body position vector in the rotating coordinate frame

$x^*, y^*, z^*$	= Dimensional components of the third body position vector in the rotating coordinate frame, m
$Y_2$	= $\mathcal{H}_2$ solution to observer Ricatti equation
$y$	= Rendezvous navigation filter measurement vector
$Z$	= Rendezvous navigation filter estimation state vector
$z_{reg}$	= $\mathcal{H}_2$ guidance law regulated variables

## Greek Symbols

$\alpha$	= Sensor shaft angle measurement
$\alpha_\eta, \alpha_\zeta$	= Constant matrices
$\beta$	= Sensor trunnion angle measurement
$\Gamma$	= States used in the $\mathcal{H}_2$ linear simulation
$\Delta V$	= Change in velocity
$\delta_p$	= Relative position vector between target and chaser vehicles
$\delta_s$	= Position vector of the sensor in the body coordinate frame
$\delta_v$	= Relative velocity vector between target and chaser vehicles
$\theta$	= Pitch angle computed measurement
$\mu$	= Non-dimensional mass ratio
$\xi, \eta, \zeta$	= Non-dimensional components of the linearized third body position vector in the rotating coordinate system
$\Pi_d$	= Non-dimensional standard deviation matrix of

	plant disturbances
$\Pi_m$	= Non-dimensional standard deviation matrix of measurement noise
$\pi$	= 3.141592654
$\pi_a$	= Non-dimensional acceleration standard deviation
$\pi_p$	= Non-dimensional position standard deviation
$\pi_v$	= Non-dimensional velocity standard deviation
$\rho_{ES}$	= Non-dimensional position of the third body with respect to the Earth
$\rho_{MS}$	= Non-dimensional position of the third body with respect to the Moon
$\rho_\eta, \rho_\zeta$	= $\mathcal{H}_2$ guidance law weighting parameters
$\sigma$	= Standard deviation
$\tau$	= Torsion, $\frac{1}{\text{km}}$
$\Phi$	= State transition matrix associated with rendezvous targeting
$\Phi_G$	= State transition matrix associated with the linearized equations of motion
$\phi$	= Roll angle computed measurement
$\Psi_{ip}$	= Target vehicle position vector for rendezvous targeting
$\Psi_{iv}$	= Target vehicle velocity vector for rendezvous targeting
$\psi_\xi, \psi_\eta, \psi_\zeta$	= Phase angles
$\Omega$	= Non-dimensional linearized state vector of the

third body in the rotating coordinate system

$\Omega_{cp}$  = Chaser vehicle position vector for rendezvous  
targeting

$\Omega_{cv}$  = Chaser vehicle velocity vector for rendezvous  
targeting

## Chapter 1

### Introduction

*"...for the next century, back to the Moon, back to the future, and this time, back to stay. And then a journey into tomorrow, a journey to another planet, a manned mission to Mars."*

*President George Bush*

In his speech on July 20, 1989, President Bush launched what has become known as the Space Exploration Initiative. The goals outlined in his speech were to return man to the Moon, establish a permanent presence on the Moon and then proceed on to Mars. The concept of human exploration of Mars did not originate with the Space Exploration Initiative; initial mission scenarios were proposed by von Braun and Ryan [1] in 1954. The Space Exploration Initiative just rejuvenated national enthusiasm for a manned mission to Mars. Its significance was further strengthened by the "Report of the Advisory Committee On the Future of the U.S. Space Program" [2]. One of the 15 specific recommendations of the Advisory Committee was to establish the long-term goal of the U. S. Space Program to be the human exploration of Mars.

In support of this project, NASA conducted a 90-day study of the main elements of a Human Exploration Initiative [3]. Included in NASA's

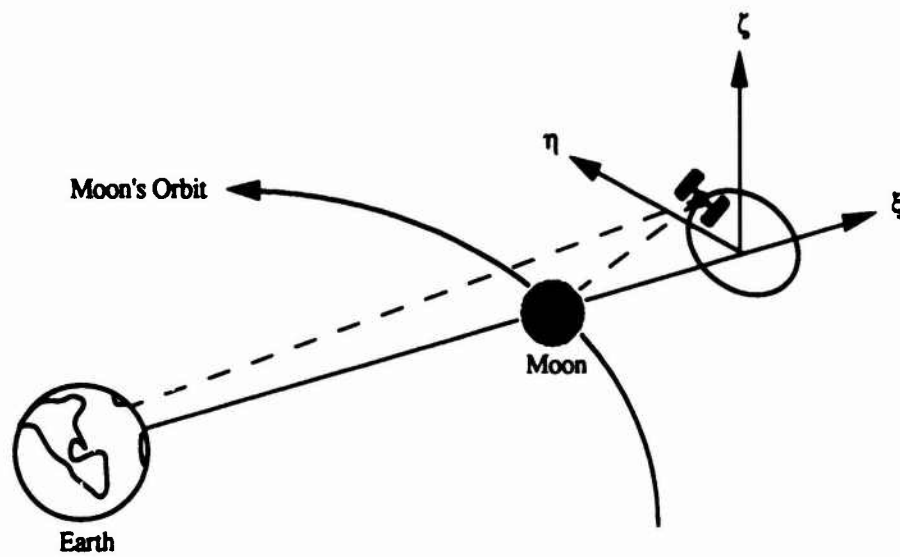


report were four approaches to a manned mission to Mars. Common to all four approaches was the deployment of a telecommunications satellite in halo orbit about the translunar equilibrium point to support farside lunar communications. Figure 1.1 shows the geometry of a telecommunication satellite in translunar halo orbit.

In parallel with the Advisory Committee and at the request of the National Space Council, the Synthesis Group was formed to specifically examine the Space Exploration Initiative. Their report [4] was similar to the NASA 90-day study in that they also proposed four architectures to a manned mission to Mars depending on the chosen scientific objectives. Although a telecommunications satellite in translunar halo orbit was not specifically mentioned in any of their four architectures, the Synthesis Group did reference traveling to and from the cislunar equilibrium point and even possible staging operations from this point. Further, they validated the need for new or additional rendezvous techniques if a equilibrium point was to be used for staging operations to Mars.

Navigation capabilities were also addressed by the Synthesis Group as a supporting technology. They concluded that navigation from onboard systems would satisfy the real time navigation requirements during critical operations such as rendezvous. In addition, NASA's lead center for the Space Exploration Initiative has identified translunar equilibrium point navigation as a potential study issue [5].

In this chapter, the basic premise of this research is put forth and specific goals are detailed. Previous work relating to this research is then summarized and followed by an brief outline of this manuscript.



or viewing from the Earth

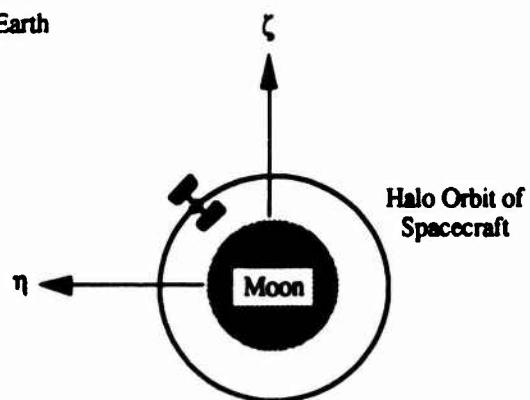


Figure 1.1: Telecommunications Satellite in Translunar Halo Orbit

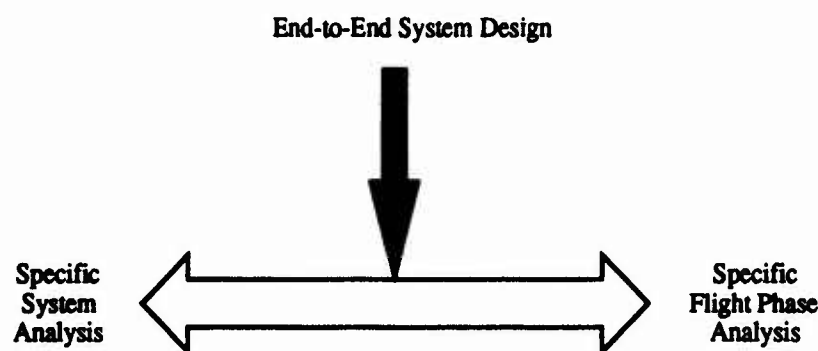


Figure 1.2: System Design Continuum

## 1.1 Research Premise

The primary objective of this research is to design a representative end-to-end guidance and navigation system (see Fig. 1.2) for the terminal phase rendezvous of two spacecraft in the three-body problem. Further, this system is demonstrated using a realistic and practical application; the major characteristics and trends associated with this application are detailed. The application chosen was the rendezvous of two spacecraft in translunar halo orbit; the translunar halo orbit was chosen because it combines the mission concepts introduced in the NASA 90-day study [3] and the proposed architectures of the Synthesis Group's report [4]. Figure 1.3 illustrates the rendezvous scenario. The secondary objective of this research is to develop an interactive nonlinear simulation package for terminal phase rendezvous guidance and navigation system evaluation in the three-body problem.

Specific goals have been established for this research:

1. Develop a frequency-domain approach to the translunar halo orbit guidance problem.

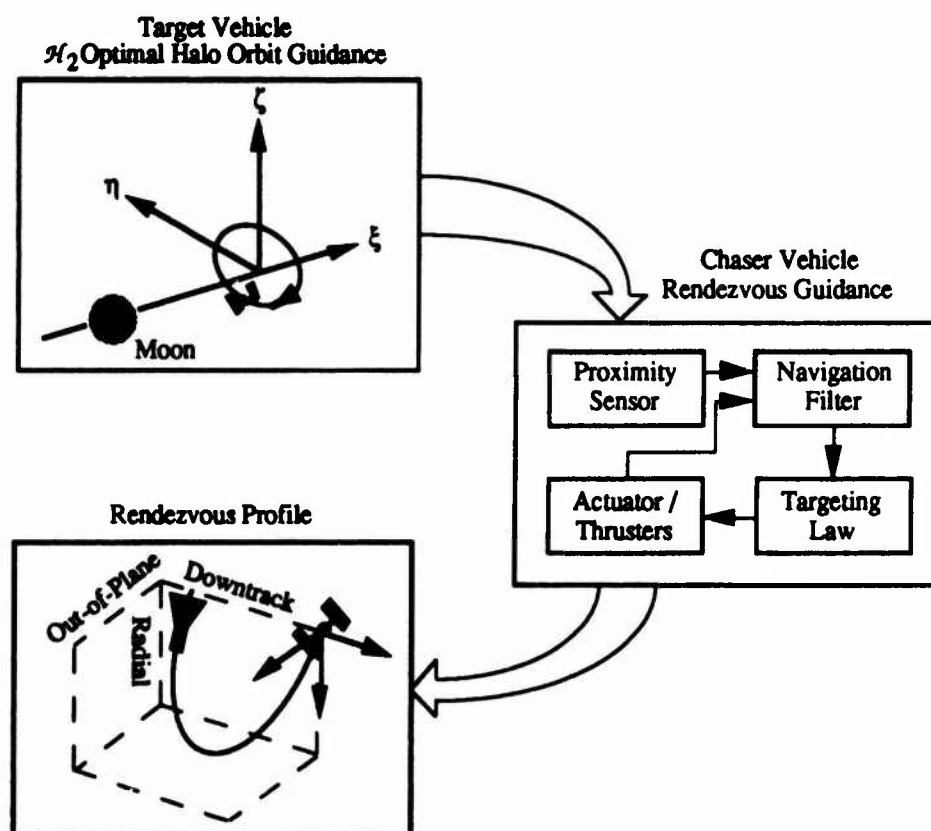


Figure 1.3: Rendezvous Scenario

2. Formulate the system model for the translunar halo orbit guidance problem in a general manner applicable to both  $\mathcal{H}_2$  and  $\mathcal{H}_\infty$  control theory design techniques.
3. Investigate the effect of system parameters on the resultant translunar halo orbit geometry and station-keeping cost.
4. Develop a two spacecraft terminal phase rendezvous targeting law for the three-body problem.
5. Characterize the three-body terminal phase rendezvous problem and contrast it with the well-known two-body problem.
6. Develop a rendezvous navigation filter to supply chaser state information to the rendezvous targeting law.
7. Characterize navigational aspects of the three-body terminal phase rendezvous problem.
8. Develop a nonlinear simulation package to be used interactively.
9. Construct the simulation package in a modular manner.
10. Fully document all simulation source code.
11. Provide simulation processing status messages at regular intervals.

## **1.2 Previous Work**

### **1.2.1 Halo Orbit Guidance**

In the late 1960's, NASA began examining follow-on lunar exploration opportunities to the the Apollo program. In an effort to open up the

farside of the Moon to exploration, studies were undertaken to determine if continuous communications or staging operations with a farside lunar base could be accomplished. Three main concepts were examined:

1. A translunar halo orbit.

A translunar halo orbit is an pseudo-circular orbit about the translunar equilibrium point which has continuous line-of-sight with the Earth. The term "halo" comes from the trajectory as seen from the Earth; the orbital path looks like a halo around the Moon (see Fig. 1.1).

2. A hummingbird orbit.

A hummingbird orbit is a stationary orbit at an offset point from the translunar equilibrium point. This orbit is similar to a hummingbird in stationary flight.

3. A polar lunar orbit.

This trajectory is a classical polar orbit around the Moon.

Many investigators [6] - [26] have examined the general halo orbit guidance problem; this section will summarize only those sources which directly apply to the translunar halo orbit guidance problem.

Farquhar [12] [13] and Farquhar and Kamel [15] provided an extensive review of previous work done on controlling an orbit about an equilibrium point. They showed that using a simple proportional plus derivative controller provided asymptotic stability while minimizing the control acceleration required. Deviations from the desired orbit were not considered in the minimization. Breakwell, et al [7] formulated the halo orbit guidance problem as a periodic system. They used the classical optimal control approach with

the addition of an observer to the system model. Position deviations were considered in their problem formulation, but only results for a large halo orbit radius were given.

Subsequently, the General Electric Company completed a flight dynamics study [24] of both the halo and hummingbird concepts. They found both concepts feasible, but preferred the halo orbit due to less propulsion requirements for station-keeping. Their formulation used a frequency matching guidance law with discrete impulses applied twice an orbit. Heppenheimer [18] used phase-plane methods to construct a family of locally fuel-optimal out-of-plane period controls. More recently, Fraietta and Bond [17] computed station-keeping costs for orbits about both the cislunar and translunar equilibrium points. Vonbun [26] investigated using a hummingbird orbit rather than a halo orbit and found in general it required ten percent more acceleration to maintain the desired position.

Finally, Farquhar [14] compared the use of a polar lunar orbit and halo orbit for lunar exploration staging operations. He concluded that a halo orbit space station could offer important operational and performance advantages compared to a polar lunar orbit station. Among these advantages were increased communication opportunities with the lunar surface and increased launch windows for transfers between the space station and the lunar surface.

### **1.2.2 Rendezvous Targeting**

Rendezvous with a spacecraft in translunar halo orbit consists of a preliminary and a terminal phase. The preliminary phase guides the chaser vehicle from its origin to the halo orbit in relatively close proximity to the target vehicle. A typical final state to the preliminary phase places the chaser

vehicle 15-20 km behind the target vehicle with its velocity vector pointing in the direction of the target vehicle. Subsequently, the terminal phase guides the chaser vehicle to a small specified relative position and velocity with respect to the target vehicle. The Space Shuttle program targets terminal phase rendezvous to place the chaser vehicle 300 m in front of the target vehicle with zero relative velocity.

This research does not consider the preliminary phase. Many investigators [27] - [34] have already examined how to optimally guide a spacecraft from low-Earth or low-lunar orbit to the translunar equilibrium point or to a halo orbit about the translunar equilibrium point. By contrast, published literature on terminal phase rendezvous targeting has been limited solely to the two-body problem.

### 1.2.3 Rendezvous Navigation

The rendezvous targeting law is dependent on accurate state information of the chaser and target vehicles. Therefore, a rendezvous navigation filter is required to provide such information. No published papers were found concerning terminal phase rendezvous navigation in the three-body problem; only two publications were found on the orbit determination of a single spacecraft about an equilibrium point in the Earth-Moon three-body system [24], [35].

The General Electric flight dynamics study [24] previously cited in the halo orbit guidance section also contained an initial tracking accuracy study of a spacecraft in translunar halo orbit. This study used measurements from Earth-based sensors. More recently, Gingiss [35] investigated the feasibility of using current radiometric techniques for the navigation of a spacecraft



to, from, or at the Earth-Moon equilibrium points using various navigation infrastructures, but not including onboard navigation systems. These two publications showed consistent results with the minor differences being attributed to the advance of sensor capabilities in the last 20 years.

### 1.3 Dissertation Organization

Chapter 2 discusses the circular restricted problem of three-bodies. The relevant equations of motion are derived and the location and stability of the equilibrium points determined. Periodic orbits about the translunar equilibrium point are discussed and the need for active halo orbit guidance established.

Chapter 3 presents the halo orbit guidance problem. The system models are developed and a  $\mathcal{H}_2$  optimal guidance law computed. A linear simulation is formulated to validate the guidance law. Several parametric studies were conducted and the results are summarized.

Chapter 4 develops the rendezvous targeting law. The target and chaser vehicle's state equations are presented. The terminal phase initiation and terminal phase final targeting laws are derived. The nonlinear simulation described in Chapter 7 was used to verify this law and the results from several parametric studies are given.

Chapter 5 is devoted to the development of the navigation filter. The dynamical system is discussed and the continuous-discrete extended Kalman filter presented. The results of several parametric studies are given; these data were generated using the nonlinear simulation given in Chapter 7.

Chapter 6 contains the application of the entire guidance and navigation system to the two spacecraft rendezvous problem in translunar halo

orbit. Two specific cases are examined; the first case is an entirely "in-plane" relative trajectory for the rendezvous profile while the second case is contains some out-of-plane relative motion.

Chapter 7 details the functional description of the nonlinear simulation package. This simulation package was developed for terminal phase rendezvous guidance and navigation system evaluation. Each module associated with a mission function is outlined.

Finally, Chapter 8 summaries this research and draws general conclusions about two spacecraft terminal phase rendezvous in the circular restricted three-body problem.

## Chapter 2

### The Circular Restricted Problem of Three-Bodies

Investigation into the problem of three-bodies dates back to the eighteenth century. In 1772, Lagrange showed the existence of equilibrium points in the restricted three-body problem. The three-body problem has been the focus of much research in classical celestial mechanics; Szebehely [36] devoted an entire volume to just this subject. The restricted three-body problem defines a system where two primary bodies revolve around their barycenter in circular orbits under the influence of their mutual gravitational attraction and the third body, which has significantly less mass, is attracted by the two primary bodies but does not influence their motion. The restricted problem of three-bodies mathematically describes the motion of the third body.

Certain approximations are made when using the restricted problem. For the Earth-Moon system, Szebehely [36] makes precise statements of these approximations:

1. The motion of the primaries (Earth and Moon) takes place approximately in a plane;
2. The motion of the third body takes place essentially in the same plane;
3. The effect of a typical probe on the motion of the primaries is of the order  $10^{-16}$  as compared to the forces acting between the primaries;
4. The motion of the primaries is essentially circular.

The first approximation is satisfied by noting that the oscillation of the Earth-Moon orbital plane is only a few minutes ( $1 \text{ min} = 0.0167 \text{ deg}$ ) each year. The restricted problem used in this research will be modified to include three-dimensional motion; thus, the second approximation will be eliminated. The third approximation restricts the third body to less than 13,000 lbs which this research will assume to be satisfied. Finally, the Moon's orbit has an eccentricity of 0.055; hence, the last approximation is met.

In this chapter, the nonlinear equations of motion are developed in both dimensional and non-dimensional units. The equilibrium points for the Earth-Moon system are identified and the non-dimensional equations of motion are linearized about the translunar equilibrium point. Lastly, the linearized equations are solved analytically and it is shown that a small radius halo orbit can not exist without active guidance.

## 2.1 Nonlinear Equations of Motion

Consider the motion of a third body in the gravitational field of two primary bodies of spherically symmetric mass distribution. These two primary bodies revolve about their barycenter in circular orbits. Figure 2.1 shows the force diagram for this problem. An inertial coordinate system ( $\hat{i}_I, \hat{j}_I, \hat{k}_I$ ) and a rotating coordinate system ( $\hat{i}_R, \hat{j}_R, \hat{k}_R$ ) with their origins at the barycenter are shown in Fig. 2.1. The relative positions of the third body with respect to the Earth and Moon are given by  $\mathbf{r}_{ES}$  and  $\mathbf{r}_{MS}$ , respectively. Three forces act on the third body: the gravitational attraction of the Moon ( $\mathbf{F}_M$ ), the gravitational attraction of the Earth ( $\mathbf{F}_E$ ), and the control force generated by internal propulsion ( $\mathbf{F}_p$ ). The positions of the Moon and Earth in the rotating coordinate system are given by  $\mathbf{a}$  and  $\mathbf{b}$ . The orbital motion of the Moon is

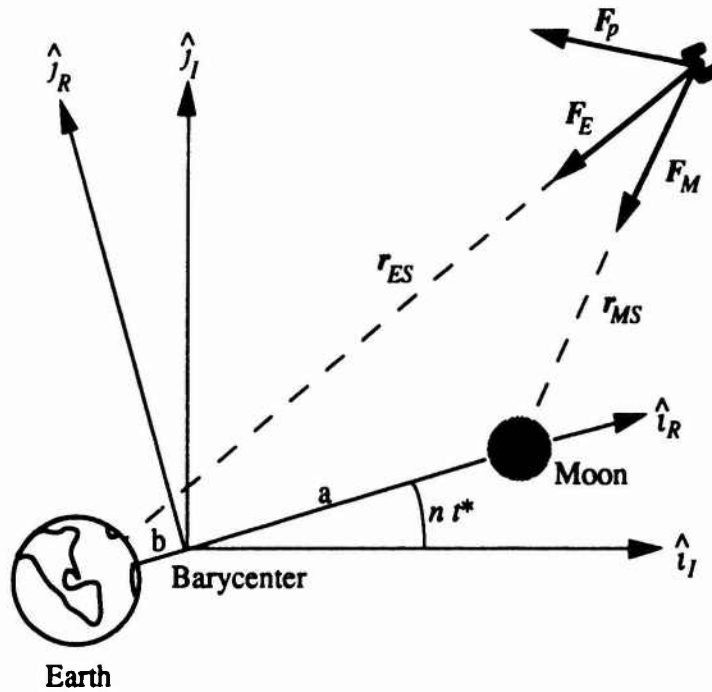


Figure 2.1: Force Diagram

described by the mean motion ( $n$ ) and dimensional time ( $t^*$ ).

For the rotating coordinate system, summing the external forces yields

$$\sum \mathbf{F} = \mathbf{F}_M + \mathbf{F}_E + \mathbf{F}_p \quad (2.1)$$

$$= - \left\{ \frac{G_r m_M m_S \mathbf{r}_{MS}}{|\mathbf{r}_{MS}|^3} \right\} - \left\{ \frac{G_r m_E m_S \mathbf{r}_{ES}}{|\mathbf{r}_{ES}|^3} \right\} + m_S \mathbf{a}_S \quad (2.2)$$

$$= - \left\{ \frac{G_r m_M m_S [(x^* - a)\hat{i}_R + y^* \hat{j}_R + z^* \hat{k}_R]}{|\mathbf{r}_{MS}|^3} \right\} \\ - \left\{ \frac{G_r m_E m_S [(x^* + b)\hat{i}_R + y^* \hat{j}_R + z^* \hat{k}_R]}{|\mathbf{r}_{ES}|^3} \right\} \\ + \{ m_S [a_x \hat{i}_R + a_y \hat{j}_R + a_z \hat{k}_R] \} \quad (2.3)$$

where  $(x^*, y^*, z^*)$  are the dimensional position components of the third body

in each axis of the rotating coordinate system  $(\hat{i}_R, \hat{j}_R, \hat{k}_R)$ , respectively. Differentiating  $\mathbf{r}_S$  twice in the rotating coordinate system yields

$$\begin{aligned} \frac{d^2 \mathbf{r}_S}{dt^{*2}} = & \left\{ \frac{d^2 x^*}{dt^{*2}} - 2n \frac{dy^*}{dt^*} - n^2 x^* \right\} \hat{i}_R \\ & + \left\{ \frac{d^2 y^*}{dt^{*2}} + 2n \frac{dx^*}{dt^*} - n^2 y^* \right\} \hat{j}_R \\ & + \left\{ \frac{d^2 z^*}{dt^{*2}} \right\} \hat{k}_R. \end{aligned} \quad (2.4)$$

Applying Newton's second law of motion for a constant mass system

$$\sum \mathbf{F} = m_S \frac{d^2 \mathbf{r}_S}{dt^{*2}} \quad (2.5)$$

yields the three second-order scalar differential equations of motion in dimensional coordinates

$$\frac{d^2 x^*}{dt^{*2}} - 2n \frac{dy^*}{dt^*} - n^2 x^* = -G_r \left\{ \frac{m_M (x^* - a)}{|\mathbf{r}_{MS}|^3} + \frac{m_E (x^* + b)}{|\mathbf{r}_{ES}|^3} \right\} + a_x \quad (2.6)$$

$$\frac{d^2 y^*}{dt^{*2}} + 2n \frac{dx^*}{dt^*} - n^2 y^* = -G_r y^* \left\{ \frac{m_M}{|\mathbf{r}_{MS}|^3} + \frac{m_E}{|\mathbf{r}_{ES}|^3} \right\} + a_y \quad (2.7)$$

$$\frac{d^2 z^*}{dt^{*2}} = -G_r z^* \left\{ \frac{m_M}{|\mathbf{r}_{MS}|^3} + \frac{m_E}{|\mathbf{r}_{ES}|^3} \right\} + a_z \quad (2.8)$$

where

$$|\mathbf{r}_{MS}| = \sqrt{(x^* - a)^2 + y^{*2} + z^{*2}} \quad (2.9)$$

$$|\mathbf{r}_{ES}| = \sqrt{(x^* + b)^2 + y^{*2} + z^{*2}}. \quad (2.10)$$

The non-dimensional equations of motion result after substituting the non-dimensional variables

$$t \triangleq nt^* \quad (2.11)$$

$$x \triangleq \frac{x^*}{(a+b)} \quad (2.12)$$

$$y \triangleq \frac{y^*}{(a+b)} \quad (2.13)$$

$$z \triangleq \frac{z^*}{(a+b)} \quad (2.14)$$

$$\mu \triangleq \frac{m_M}{(m_E + m_M)} \quad (2.15)$$

$$U_x \triangleq \frac{a_x}{(a+b)n^2} \quad (2.16)$$

$$U_y \triangleq \frac{a_y}{(a+b)n^2} \quad (2.17)$$

$$U_z \triangleq \frac{a_z}{(a+b)n^2} \quad (2.18)$$

into Eqs. (2.6 - 2.8)

$$\frac{d^2x}{dt^2} - 2\frac{dy}{dt} - x = -\left\{ \frac{\mu[x - (1-\mu)]}{\rho_{MS}^3} + \frac{(1-\mu)[x + \mu]}{\rho_{ES}^3} \right\} + U_x \quad (2.19)$$

$$\frac{d^2y}{dt^2} + 2\frac{dx}{dt} - y = -y \left\{ \frac{\mu}{\rho_{MS}^3} + \frac{(1-\mu)}{\rho_{ES}^3} \right\} + U_y \quad (2.20)$$

$$\frac{d^2z}{dt^2} = -z \left\{ \frac{\mu}{\rho_{MS}^3} + \frac{(1-\mu)}{\rho_{ES}^3} \right\} + U_z \quad (2.21)$$

where

$$\rho_{MS} = \sqrt{[x - (1-\mu)]^2 + y^2 + z^2} \quad (2.22)$$

$$\rho_{ES} = \sqrt{[x + \mu]^2 + y^2 + z^2}. \quad (2.23)$$

Equations (2.19 - 2.21) are the preferred equations of motion since specific information about the two primary bodies (other than the mass ratio) is not required. Also, the non-dimensional equations have better numerical conditioning since all terms are of the order one.

Define the nonlinear state and control as

$$X(t) \triangleq \begin{bmatrix} x(t) \\ y(t) \\ z(t) \\ \dot{x}(t) \\ \dot{y}(t) \\ \dot{z}(t) \end{bmatrix} \quad (2.24)$$

and

$$U(t) \triangleq \begin{bmatrix} U_x(t) \\ U_y(t) \\ U_z(t) \end{bmatrix}. \quad (2.25)$$

Writing Eqs. (2.19 - 2.21) in first order functional matrix form gives

$$\dot{X} = f_1(X(t)) + g_1(U(t)) \quad (2.26)$$

where

$$f_1(X(t)) = \begin{bmatrix} \dot{x} \\ \dot{y} \\ \dot{z} \\ x + 2y - \left\{ \frac{\mu[x - (1 - \mu)]}{\rho_{MS}^3} + \frac{(1 - \mu)[x + \mu]}{\rho_{ES}^3} \right\} \\ -2\dot{x} - y \left\{ \frac{\mu}{\rho_{MS}^3} + \frac{(1 - \mu)}{\rho_{ES}^3} - 1 \right\} \\ -z \left\{ \frac{\mu}{\rho_{MS}^3} + \frac{(1 - \mu)}{\rho_{ES}^3} \right\} \end{bmatrix} \quad (2.27)$$

$$g_1(U(t)) = \begin{bmatrix} 0 \\ 0 \\ 0 \\ U_x \\ U_y \\ U_z \end{bmatrix} \quad (2.28)$$

$$(\dot{\phantom{x}}) \triangleq \frac{d}{dt}. \quad (2.29)$$

## 2.2 Equilibrium Point Location

Equilibrium points occur when all external forces are balanced. Mathematically, they occur when all derivatives in the differential equations are zero or undefined. In Eq. (2.27), setting all derivatives to zero yields

$$x - \frac{\mu[x - (1 - \mu)]}{\rho_{MS}^3} - \frac{(1 - \mu)[x + \mu]}{\rho_{ES}^3} = 0 \quad (2.30)$$

$$y \left\{ 1 - \frac{\mu}{\rho_{MS}^3} - \frac{(1 - \mu)}{\rho_{ES}^3} \right\} = 0 \quad (2.31)$$

$$z = 0. \quad (2.32)$$



Equation (2.31) yields two cases for equilibrium points:

$$y = 0 \quad (2.33)$$

$$\left\{ 1 - \frac{\mu}{\rho_{MS}^3} - \frac{(1-\mu)}{\rho_{ES}^3} \right\} = 0. \quad (2.34)$$

The first case, Eq. (2.33), locates the collinear equilibrium points; the second case, Eq. (2.34), locates the triangular equilibrium points.

Equation (2.30) was derived for the third body in the region containing the  $L_1$  equilibrium point. For the third body in the regions containing the other two collinear equilibrium points, the signs on the second and third terms in Eq. (2.30) change. Thus, Eq. (2.30) becomes

$$x \mp \frac{\mu[x - (1-\mu)]}{\rho_{MS}^3} \mp \frac{(1-\mu)[x + \mu]}{\rho_{ES}^3} = 0 \quad (2.35)$$

where the appropriate signs are given in Table 2.1. Equation (2.35) results in a fifth-order equation in  $x$  where the real root locates the equilibrium point.

Table 2.1: Appropriate Signs for Collinear Equilibrium Points

Equilibrium Point	Second Term	Third Term
$L_1$	-	-
$L_2$	+	-
$L_3$	+	+

For the triangular equilibrium points, Eqs. (2.30) and (2.34) are satisfied when

$$\rho_{ES} = 1 \quad (2.36)$$

$$\rho_{MS} = 1. \quad (2.37)$$

Hence, Eqs. (2.36) and (2.37) are used instead of Eqs. (2.30) and (2.34) to locate the these equilibrium points.

For the Earth-Moon system,  $\mu = 0.0121506$  [37], which results in the equilibrium points given in Table 2.2. Figure 2.2 shows the geometry of the restricted three-body problem equilibrium points.

Table 2.2: Equilibrium Point Locations

Equilibrium Point	$x$	$y$	$z$
Translunar ( $L_1$ )	1.155682	0	0
Cislunar ( $L_2$ )	0.836915	0	0
Transearth ( $L_3$ )	-1.005063	0	0
Triangular ( $L_{4,5}$ )	0.487849	$\pm 0.866025$	0

### 2.3 Linearized Equations of Motion

Define the linearized state and control as

$$\Omega \triangleq \begin{bmatrix} \xi \\ \eta \\ \zeta \\ \dot{\xi} \\ \dot{\eta} \\ \dot{\zeta} \end{bmatrix} \triangleq \begin{bmatrix} x - x_{nom} \\ y - y_{nom} \\ z - z_{nom} \\ \dot{x} - \dot{x}_{nom} \\ \dot{y} - \dot{y}_{nom} \\ \dot{z} - \dot{z}_{nom} \end{bmatrix} = \mathbf{X} - \mathbf{X}_{nom} \quad (2.38)$$

and

$$\mathbf{u} \triangleq \begin{bmatrix} u_\xi \\ u_\eta \\ u_\zeta \end{bmatrix} \triangleq \begin{bmatrix} U_x - U_{x_{nom}} \\ U_y - U_{y_{nom}} \\ U_z - U_{z_{nom}} \end{bmatrix} = \mathbf{U} - \mathbf{U}_{nom} \quad (2.39)$$

where  $(\ )_{nom}$  denotes a nominal value. Neglecting the higher order terms in a Taylor series expansion yields

$$\dot{\Omega} = \mathbf{A}_G \Omega + \mathbf{B}_G \mathbf{u} \quad (2.40)$$

where

$$\mathbf{A}_G = \left[ \frac{\partial \mathbf{f}_1}{\partial \mathbf{X}} \right]_{nom} \quad (2.41)$$

$$\mathbf{B}_G = \left[ \frac{\partial \mathbf{g}_1}{\partial \mathbf{U}} \right]_{nom} \quad (2.42)$$



Note the  $\zeta$ -axis can be uncoupled from the  $\xi$  and  $\eta$ -axes after the linearization.

## 2.4 Periodic Orbits

The general solution to Eq. (2.40) is

$$\Omega(t) = \Phi_G(t, 0) \Omega(0) + \int_0^t \Phi_G(t - \tau, 0) B_G u(\tau) d\tau \quad (2.45)$$

where

$$\Phi_G(t, 0) = \exp A_G t \quad (2.46)$$

and satisfies

$$\dot{\Phi}_G(t, 0) = A_G \Phi_G(t, 0). \quad (2.47)$$

The first term in Eq. (2.45) represents the unforced solution to Eq. (2.40) and the second term gives the forced solution. Appendix A.1 details the solution to the state transition matrix,  $\Phi_G(t, 0)$ . Hence, the unforced solution to Eq. (2.40) becomes

$$\begin{aligned} \xi(t) = & 1.586694C_1 \exp^{-2.158677t} - 1.586694C_2 \exp^{2.158677t} \\ & - 0.184326C_3 \cos(1.862647t) + \frac{0.639513C_4}{1.862647} \sin(1.862647t) \end{aligned} \quad (2.48)$$

$$\begin{aligned} \eta(t) = & C_1 \exp^{-2.158677t} + C_2 \exp^{2.158677t} \\ & + C_4 \cos(1.862647t) + \frac{C_3}{1.862647} \sin(1.862647t) \end{aligned} \quad (2.49)$$

$$\zeta(t) = \zeta(0) \cos(1.786178t) + \frac{\dot{\zeta}(0)}{1.786178} \sin(1.786178t) \quad (2.50)$$

where

$$\begin{aligned} C_1 = & 0.420595\xi(0) - 0.123011\dot{\xi}(0) \\ & + 0.0786673\eta(0) + 0.0775267\dot{\eta}(0) \end{aligned} \quad (2.51)$$

$$C_2 = -0.420595\xi(0) - 0.123011\dot{\xi}(0)$$

$$+0.0786673\eta(0) - 0.0775267\dot{\eta}(0) \quad (2.52)$$

$$C_3 = 1.815860\xi(0) + 1.334710\dot{\eta}(0) \quad (2.53)$$

$$C_4 = 0.246022\dot{\xi}(0) + 0.842665\eta(0). \quad (2.54)$$

In general, Eqs. (2.48 - 2.50) are unbounded because of the exponentially increasing terms; thus, the linear system is unstable. However, if the initial conditions are chosen properly, the exponential terms can be eliminated. Selecting

$$\dot{\xi}(0) = 0.639514\eta(0) \quad (2.55)$$

$$\dot{\eta}(0) = -5.425170\xi(0) \quad (2.56)$$

reduces Eqs. (2.48 - 2.50) to purely periodic terms

$$\xi(t) = \xi(0) \cos(1.862647t) + 0.343336\eta(0) \sin(1.862647t) \quad (2.57)$$

$$\eta(t) = \eta(0) \cos(1.862647t) - 2.928719\xi(0) \sin(1.862647t) \quad (2.58)$$

$$\zeta(t) = \zeta(0) \cos(1.786178t) + \frac{\dot{\zeta}(0)}{1.786178} \sin(1.786178t). \quad (2.59)$$

In addition, if the periodic orbit is chosen to be centered about  $L_1$ , that is  $\xi(0) = 0$ , and the initial point of the orbit is selected so that  $\dot{\zeta}(0) = 0$ , Eqs. (2.57 - 2.59) further reduce to

$$\xi(t) = 0.343336\eta(0) \sin(1.862647t) \quad (2.60)$$

$$\eta(t) = \eta(0) \cos(1.862647t) \quad (2.61)$$

$$\zeta(t) = \zeta(0) \cos(1.786178t). \quad (2.62)$$

It is readily apparent that a small radius halo orbit can not exist without active guidance because of the different natural frequencies between the  $\eta$ -axis and the  $\zeta$ -axis. Figure 2.3 graphically illustrates this result by choosing

$\eta(0)$  and  $\zeta(0)$  to be 0.00911 (3500 km) and 90 deg out-of-phase. This Lissajous trajectory clearly shows periods of time when the Moon will block the line-of-sight between the Earth and a third body; this period of blockage equates to a disk with a radius of 0.00806 (3100 km) centered at the origin on Fig. 2.3.

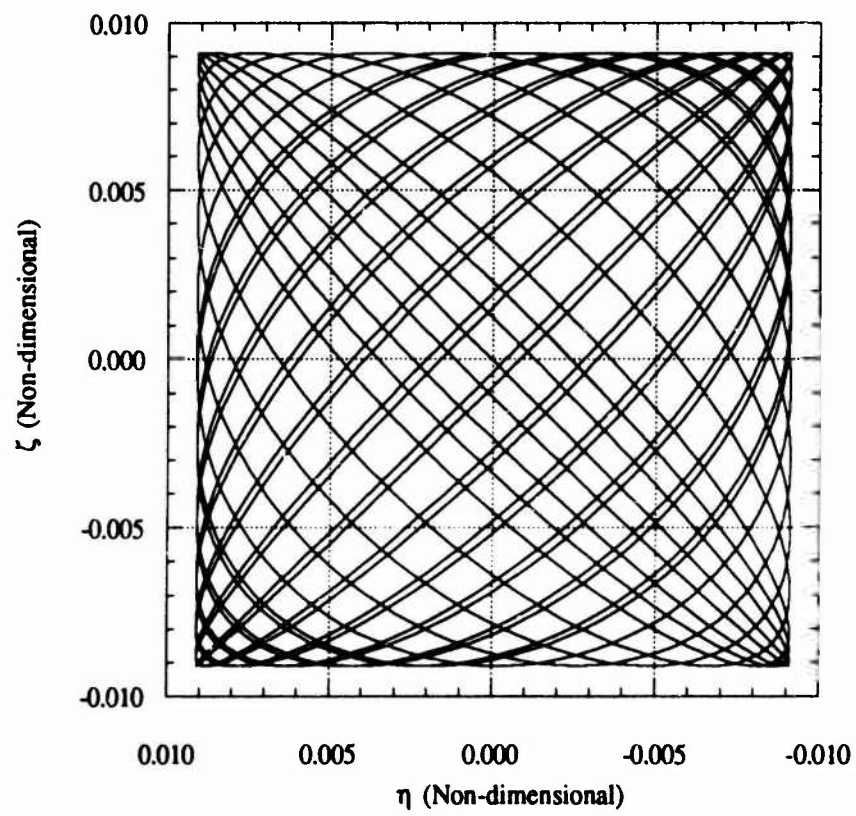


Figure 2.3: Uncontrolled Periodic Orbit

## Chapter 3

### Halo Orbit Guidance Law

Several classical time-domain techniques have been investigated for controlling a halo orbit. In this chapter, a frequency-domain technique will be introduced.  $\mathcal{H}_2$  control theory applies a frequency-domain formulation to the classical time-domain Linear Quadratic Gaussian problem. The advantage to the frequency-domain formulation is that it can be extended to modern control theories, such as  $\mathcal{H}_2$  and  $\mathcal{H}_\infty$  theory, so that the class of plant disturbances and measurement noises considered can be expanded.

This chapter starts with the formulation of the  $\mathcal{H}_2$  problem statement and system models. The state space  $\mathcal{H}_2$  solution is then discussed. A simulation is developed to validate the guidance law and results from two typical guidance laws are presented. Lastly, results from several parametric studies are given.

#### 3.1 Problem Statement

$\mathcal{H}_2$  control theory minimizes the 2-norm of the closed loop transfer function,  $\mathbf{T}_{zw}$ , between the regulated variables,  $\mathbf{z}_{reg}$ , and the exogenous inputs,  $\mathbf{w}_2$ ; the  $\mathcal{H}_2$  system model is shown in Fig. 3.1. This transfer function is the same as the lower linear fractional transformation of the system plant,  $\mathbf{P}_G$ , and the guidance law,  $\mathbf{K}_{halo}$ . Given

$$\mathbf{P}_G = \begin{bmatrix} \mathbf{P}_{G11} & \mathbf{P}_{G12} \\ \mathbf{P}_{G21} & \mathbf{P}_{G22} \end{bmatrix} \quad (3.1)$$



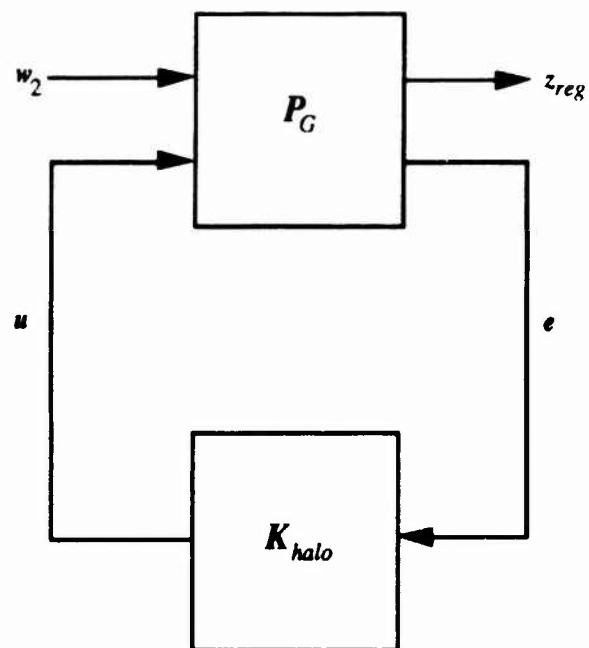


Figure 3.1:  $\mathcal{H}_2$  System Model

then

$$\mathbf{T}_{zw} = \mathbf{P}_{G11} + \mathbf{P}_{G12}\mathbf{K}_{halo}(\mathbf{I} - \mathbf{P}_{G22}\mathbf{K}_{halo})^{-1}\mathbf{P}_{G21} \quad (3.2)$$

$$= \mathbf{F}_l(\mathbf{P}_G, \mathbf{K}_{halo}). \quad (3.3)$$

A precise problem statement is

$$\text{Minimize } \|\mathbf{T}_{zw}\|_2 \quad (3.4)$$

where the regulated variables are chosen to be

$$\mathbf{z}_{reg} = \begin{bmatrix} \rho_\eta \eta \\ \rho_\zeta \zeta \\ \mathbf{u} \end{bmatrix} \quad (3.5)$$

and the exogenous inputs are chosen to be

$$\mathbf{w}_2 = \begin{bmatrix} \mathbf{w}_d \\ \mathbf{w}_m \end{bmatrix}. \quad (3.6)$$

The plant disturbances,  $\mathbf{w}_d$ , and the measurement noise,  $\mathbf{w}_m$ , have a fixed power spectrum. In addition,  $\rho_\eta$  and  $\rho_\zeta$  are selectable constants so that the relative weighting of position deviation and control acceleration can be varied. Since the deviation in the  $\xi$ -axis does not affect the line-of-sight between the halo orbit and Earth,  $\xi$  was not included as a regulated variable.

$\mathcal{H}_2$  minimization is the frequency-domain equivalent to Linear Quadratic Gaussian minimization in the time domain. The equivalent problem statement in the time-domain is

$$\text{Minimize } J = \int_0^\infty (\boldsymbol{\Omega}^T \mathbf{Q}_{LQG} \boldsymbol{\Omega} + \mathbf{u}^T \mathbf{u}) dt \quad (3.7)$$

where

$$\mathbf{Q}_{LQG} = \begin{bmatrix} \mathbf{q}_{LQG11} & \mathbf{0} \\ \mathbf{0} & \mathbf{0} \end{bmatrix} \quad (3.8)$$

$$\mathbf{q}_{LQG11} = \begin{bmatrix} 0 & 0 & 0 \\ 0 & \rho_\eta^2 & 0 \\ 0 & 0 & \rho_\zeta^2 \end{bmatrix} \quad (3.9)$$

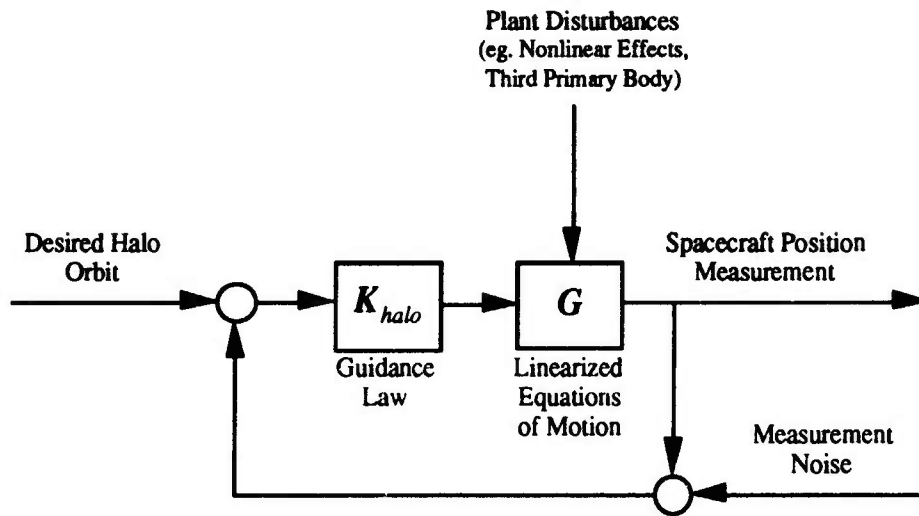


Figure 3.2: Desired System Model

### 3.2 System Models

Figure 3.2 shows the desired system model where  $G$  represents the plant and  $K_{halo}$  represents the guidance law. The plant and guidance law have the general realizations

$$G = \left[ \begin{array}{c|c} A_G & B_G \\ \hline C_G & D_G \end{array} \right] \quad \text{and} \quad K_{halo} = \left[ \begin{array}{c|c} A_K & B_K \\ \hline C_K & D_K \end{array} \right]. \quad (3.10)$$

Figure 3.3 shows an expanded system model where  $G$  has been broken down into its realization parts;  $G_r$  has the realization

$$G_r = \left[ \begin{array}{c|c} A_G & I \\ \hline I & 0 \end{array} \right]. \quad (3.11)$$

For this research, only position measurements are considered. Hence,

$$C_G = \begin{bmatrix} I & 0 \end{bmatrix} \quad \text{and} \quad D_G = 0. \quad (3.12)$$

The environment consists of plant disturbances and measurement noise, both modeled as white gaussian noise with zero mean and identity fixed power

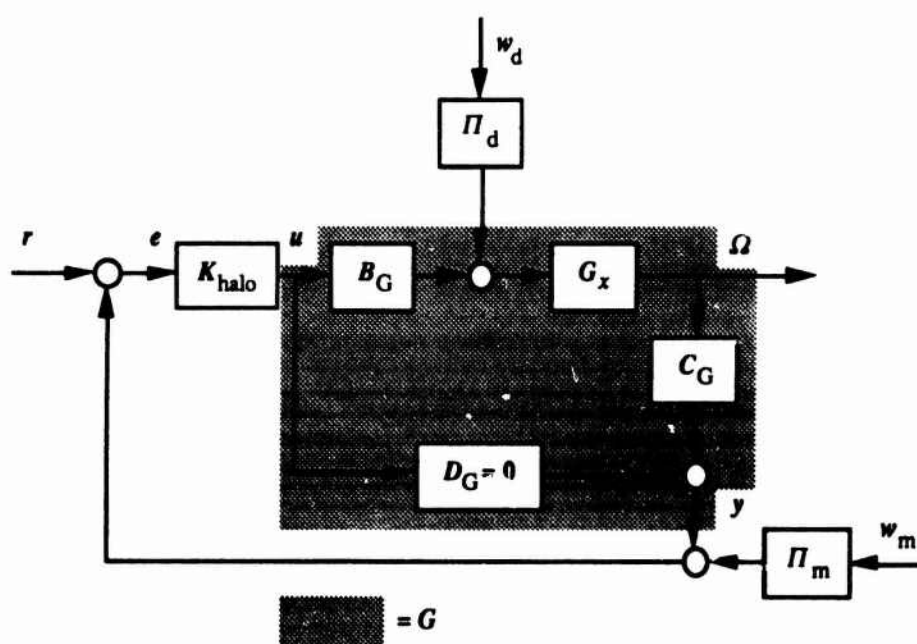


Figure 3.3: Expanded System Model

spectrum. The plant disturbance, or process noise, is then scaled by a non-dimensional matrix,  $\Pi_d$ ,

$$\Pi_d = \begin{bmatrix} \pi_v I & 0 \\ 0 & \pi_a I \end{bmatrix} \quad (3.13)$$

where  $\pi_v$  and  $\pi_a$  are the non-dimensional square root of the fixed power spectrum in velocity and acceleration, respectively. The measurement noise has also been scaled by a non-dimensional matrix,  $\Pi_m$ ,

$$\Pi_m = \pi_p I \quad (3.14)$$

where  $\pi_p$  is the non-dimensional square root of the fixed power spectrum in position. Figure 3.1 shows the system model required by Doyle, et al [38] for the two Ricatti equation  $\mathcal{H}_2$  control system design method. The plant ( $P_G$ ) in this system model has the general realization

$$P_G = \left[ \begin{array}{c|cc} A & B_1 & B_2 \\ \hline C_1 & D_{11} & D_{12} \\ C_2 & D_{21} & D_{22} \end{array} \right] \quad (3.15)$$

and requires a particular structure for the  $D$  matrices. Dailey [39] summarized a method for loop shifting and scaling these matrices; this method uses the singular value decomposition of the  $D_{12}$  and  $D_{21}$  matrices to transform a general system model into the desired form. Transforming the expanded system model (Fig. 3.3) into the  $\mathcal{H}_2$  system model and applying scaling yields

$$\dot{P}_G = \left[ \begin{array}{c|ccc} A_G & \Pi_d & 0 & \vdots & B_G \\ \hline \rho_\eta \alpha_\eta & 0 & 0 & \vdots & 0 \\ \rho_\zeta \alpha_\zeta & 0 & 0 & \vdots & 0 \\ 0 & 0 & 0 & \vdots & I \\ \dots & \dots & \dots & \dots & \dots \\ \Pi_m^{-1} C_G & 0 & I & \vdots & 0 \end{array} \right] \quad (3.16)$$

where  $(\hat{\cdot})$  indicates scaled parameters and  $\alpha_\eta$  and  $\alpha_\zeta$  are matrices defined such that

$$\eta = \alpha_\eta \Omega \quad \text{and} \quad \zeta = \alpha_\zeta \Omega. \quad (3.17)$$

### 3.3 State Space $\mathcal{H}_2$ Solution

The  $\mathcal{H}_2$  optimal solution involves solving two algebraic Ricatti equations (see Doyle, et al [38]). The first Ricatti equation ( $X_2$ ) represents state feedback; the second Ricatti equation ( $Y_2$ ) represents observer feedback. For this system, the two Ricatti equations are

$$X_2 A_G - X_2 B_G B_G^T X_2 + A_G^T X_2 + \rho_\eta^2 \alpha_\eta^T \alpha_\eta + \rho_\zeta^2 \alpha_\zeta^T \alpha_\zeta = 0 \quad (3.18)$$

$$Y_2 A_G^T - Y_2 C_G^T \Pi_m^{-T} \Pi_m^{-1} C_G Y_2 + A_G Y_2 + \Pi_d \Pi_d^T = 0. \quad (3.19)$$

Given the solutions to Eqs. (3.18) and (3.19), the feedback gain matrix becomes

$$F_{\mathcal{H}_2} = -B_G^T X_2 \quad (3.20)$$

and the observer gain matrix is

$$L_{\mathcal{H}_2} = -Y_2 C_G^T \Pi_m^{-T} \Pi_m^{-1}. \quad (3.21)$$

Finally, the optimum guidance law is given by

$$K_{halo} = \left[ \begin{array}{c|c} A_{\hat{K}} & B_{\hat{K}} \Pi_m^{-1} \\ \hline C_{\hat{K}} & 0 \end{array} \right] \quad (3.22)$$

$$= \left[ \begin{array}{c|c} A_{\hat{K}} & -L_{\mathcal{H}_2} \\ \hline F_{\mathcal{H}_2} & 0 \end{array} \right] \quad (3.23)$$

where

$$A_{\hat{K}} = A - B_G B_G^T X_2 - Y_2 C_G^T \Pi_m^{-T} \Pi_m^{-1} C_G. \quad (3.24)$$

### 3.4 Simulation Results

A simulation was developed to validate the guidance law given in Eq. (3.23). For the initial cases examined, linear simulation results were found to be in agreement with nonlinear simulation results. Therefore, the linear simulation was used to generate the results presented in this section and Appendix B. The state equation of the simulation is first formulated; then, data from two typical  $\mathcal{H}_2$  optimal guidance laws are given followed by data from three parametric studies.

#### 3.4.1 State Equation Formulation

The mathematical model of the guidance law, Eq. (3.23), is

$$\dot{\mathbf{X}}_K = \mathbf{A}_{\hat{K}} \mathbf{X}_K + \mathbf{B}_{\hat{K}} \Pi_m^{-1} \mathbf{e} \quad (3.25)$$

$$\mathbf{u} = \mathbf{C}_{\hat{K}} \mathbf{X}_K \quad (3.26)$$

where  $\mathbf{X}_K$  are the guidance law states. The inputs to the guidance law are deviations from the halo orbit,  $\mathbf{e}$ , and the outputs are the control accelerations,  $\mathbf{u}$ . From the expanded system model, Fig. 3.3, note

$$\mathbf{e} = \mathbf{C}_G \boldsymbol{\Omega} + \Pi_m \mathbf{w}_m + \mathbf{r}. \quad (3.27)$$

Hence,

$$\dot{\mathbf{X}}_K = \mathbf{B}_{\hat{K}} \Pi_m^{-1} \mathbf{C}_G \boldsymbol{\Omega} + \mathbf{A}_{\hat{K}} \mathbf{X}_K + \mathbf{B}_{\hat{K}} \mathbf{w}_m + \mathbf{B}_{\hat{K}} \Pi_m^{-1} \mathbf{r}. \quad (3.28)$$

The mathematical model associated with  $\dot{\mathbf{P}}$  is

$$\dot{\boldsymbol{\Omega}} = \mathbf{A}_G \boldsymbol{\Omega} + \Pi_d \mathbf{w}_d + \mathbf{B}_G \dot{\mathbf{u}} \quad (3.29)$$

$$\dot{\mathbf{e}} = \Pi_m^{-1} \mathbf{C}_G \boldsymbol{\Omega} + \mathbf{w}_m. \quad (3.30)$$

Hence, the Kalman filter mathematical model yields

$$\dot{\hat{\Omega}} = A_G \hat{\Omega} + B_G \hat{u} - L_{\mathcal{H}_2} \Pi_m^{-1} C_G (\Omega - \hat{\Omega}) \quad (3.31)$$

where the  $(\hat{\cdot})$  denotes the estimated system states.

Assume the guidance law states are a linear combination of the system state estimates plus additional undetermined states,  $\Gamma$ . Hence,

$$X_K = \hat{\Omega} + \Gamma. \quad (3.32)$$

Differentiating Eq. (3.32); substituting Eqs. (3.25), (3.26), (3.31) and (3.32); and noting  $\hat{u} = u$  yields

$$\dot{\Gamma} = (A_G - B_{\hat{K}} \Pi_m^{-1} C_G) \Gamma - L_{\mathcal{H}_2} w_m + B_{\hat{K}} \Pi_m^{-1} r. \quad (3.33)$$

The final state equation for the linear simulation is formed by augmenting Eqs. (3.28), (3.29) and (3.33) into a matrix equation

$$\begin{bmatrix} \dot{\Omega} \\ \dot{X}_K \\ \dot{\Gamma} \end{bmatrix} = \begin{bmatrix} A_G & B_G C_{\hat{K}} & 0 \\ B_{\hat{K}} \Pi_m^{-1} C_G & A_{\hat{K}} & 0 \\ 0 & 0 & (A_G - B_{\hat{K}} \Pi_m^{-1} C_G) \end{bmatrix} \begin{bmatrix} \Omega \\ X_K \\ \Gamma \end{bmatrix} + \begin{bmatrix} \Pi_d & 0 & 0 \\ 0 & B_{\hat{K}} & B_{\hat{K}} \Pi_m^{-1} \\ 0 & -L_{\mathcal{H}_2} & B_{\hat{K}} \Pi_m^{-1} \end{bmatrix} \begin{bmatrix} w_d \\ w_m \\ r \end{bmatrix} \quad (3.34)$$

and noting

$$\hat{\Omega} = X_K - \Gamma. \quad (3.35)$$

### 3.4.2 Typical $\mathcal{H}_2$ Guidance Laws

The simulation was run for 300 days (20 revolutions of the halo orbit) using mid-range weighting parameters ( $\rho_\eta = 170$  and  $\rho_\zeta = 550$ ) and minimum control acceleration weighting parameters ( $\rho_\eta = 36$  and  $\rho_\zeta = 1000$ ). The noise



statistics used in the simulations are given in Table 3.1. These statistics are consistent with the tracking accuracy study contained in the flight dynamics study [24].

Table 3.1: Simulation Noise Statistics

	Fixed Power Spectrum	Average State $\sigma$
Position	$\pi_p^2 = 2.665 \frac{\text{m}^2}{\text{s}}$	9.637 km
Velocity	$\pi_v^2 = 2.665\text{e-}8 \frac{\text{m}^2}{\text{s}^2}$	$1.152 \frac{\text{m}}{\text{s}}$
Acceleration	$\pi_a^2 = 1.666\text{e-}15 \frac{\text{m}^2}{\text{s}^3}$	N/A

The variations in the average total steady state propulsion requirement per day ( $\Delta V_{TOT}$ ) with respect to these input parameters is summarized in the next section and Appendix B. The reference input was a clockwise circular halo orbit with a radius of 3500 km and a non-dimensional frequency of 1.862647.

Appendix B.1 summarizes the state space realization and the transfer function matrix for the sixth-order  $\mathcal{H}_2$  guidance law using mid-range parameters. The guidance law is minimum phase and stable. Since the linearized equations of motion are uncoupled between the  $\xi$  and  $\eta$ -axes and the  $\zeta$ -axis, the guidance law is also uncoupled in this manner.

Appendix B.2 shows the last 10 revolutions of the system states, estimation error and control acceleration when the system has reached steady state. Both the system states and the control accelerations are sinusoidal functions at the selected halo orbit frequency. The estimation error is quickly driven to zero by the observer in all states. Table 3.2 compares these typical guidance laws with previous results; these results do not include process or measurement noise.

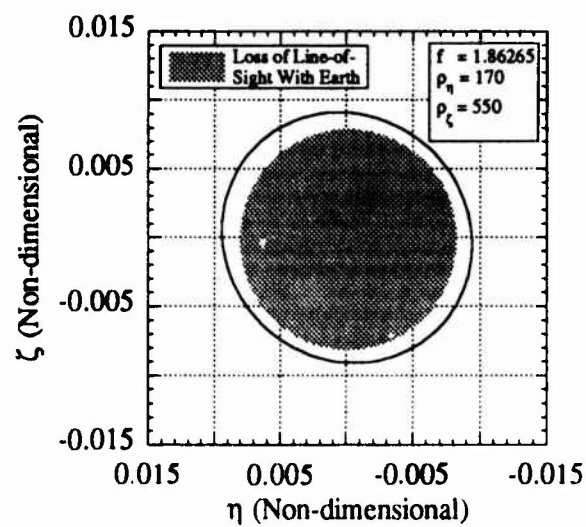
A robustness analysis was done for the mid-range weighting param-

Table 3.2:  $\Delta V_{TOT}$  Comparison

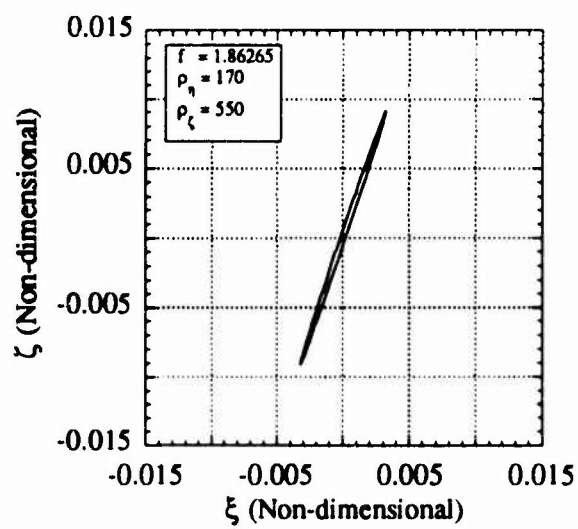
Study	$\Delta V_{TOT}$ (m/s/day)
Mid-range Weighting	0.2997
Minimum Weighting	0.1549
Farquhar [13]	0.2839
Flight Dynamics [24]	0.2800
Heppenheimer [18]	0.2929
Fraietta and Bond [17]	0.7934

ters guidance law. Structured uncertainty was used to represent error sources such as neglected high frequency dynamics, input actuator errors and low frequency plant parameter errors. The gain and phase margins were reduced with the addition of the observer into the guidance law. The gain and phase margin could be improved through the loop transfer recovery technique; however, this procedure was not applied in this research.

Figure 3.4 gives the geometric view of the halo orbit for the mid-range weighting parameters  $\mathcal{H}_2$  optimal guidance law when both process and measurement noise are absent from the simulation; Fig. 3.5 applies when  $3\sigma$  process and  $3\sigma$  measurement noise are included. The orbits are stable, repeatable and the line-of-sight with the Earth is never lost. Measurement noise showed little effect on the geometry of the resultant halo orbit; process noise showed a greater impact. Appendix B.3 gives additional geometric plots of the front and side views of the halo orbit with various amounts of process and measurement noise added to the simulation.

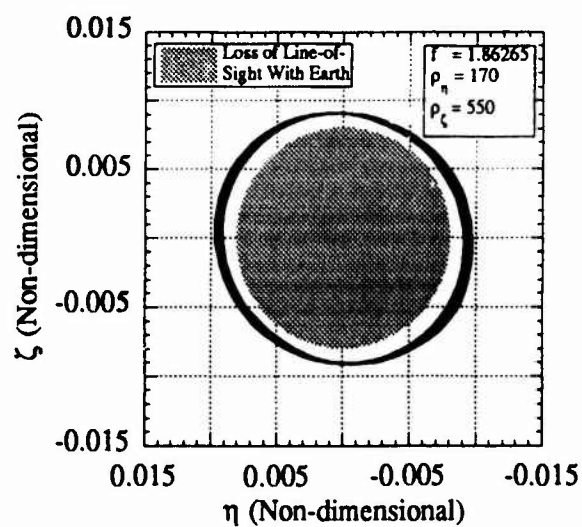


(a) Front View

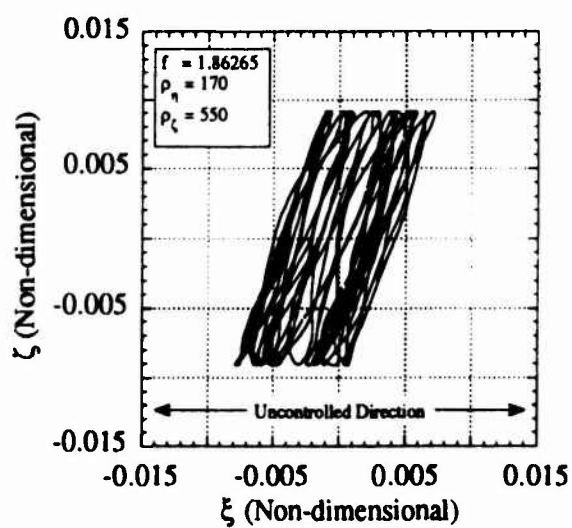


(b) Side View

Figure 3.4: Halo Orbit Geometry (Zero Noise)



(a) Front Side



(b) Side View

Figure 3.5: Halo Orbit Geometry ( $3\sigma$  Noise)

### 3.4.3 Control Input Parametric Study

Three-axes versus two-axes control ( $\xi$  and  $\zeta$ -axes) was investigated to determine the advantages or disadvantages of each method. The figures-of-merit for this parametric study were chosen to be the average steady state  $\Delta V$  per day for maintaining the orbit ( $\xi$  and  $\eta$ -axes) and the percent steady state error from the desired circular halo orbit.

Table 3.3 gives the results for three cases (a-c) where the semi-minor axis steady state error of the resultant halo orbit was held constant; the position weighting factors were varied in order to maintain constant semi-minor axis errors. Semi-minor axis errors more negative than -11.43% indicate a loss of line-of-sight with the Earth. In addition, the average steady state  $\Delta V$  per day in the  $\zeta$ -axis was held constant. Three-axis control provided a better resultant halo orbit which was closer to the desired circular orbit. However, the  $\Delta V$  associated with the tighter control was two orders of magnitude higher.

Table 3.3: Three vs. Two Axes Control

Control Axes		$\Delta V_{\xi}$	$\Delta V_{\eta}$	Major	Minor
		(m/s/day)		(% error)	
a)	3	7.866	2.694	4.85	-11.55
	2	0.034		11.92	-11.34
b)	3	8.124	2.778	4.20	-5.42
	2	0.063	-	8.53	-5.26
c)	3	8.476	2.890	2.62	-0.94
	2	0.209	-	4.03	-0.95

Two-axes control, using either control in the  $\xi$  or  $\eta$ -axis, was also investigated for advantages or disadvantages. Table 3.4 gives the results for three cases (a-c) where the average steady state  $\Delta V$  per day for each case was held constant; the position weighting factors were varied in order to maintain

Table 3.4:  $\xi$  vs.  $\eta$  Axis Control

Control Axes	$\Delta V_\xi$ (m/s/day)	$\Delta V_\eta$ (m/s/day)	Major (% error)	Minor (% error)
a) $\xi$	0.034	-	11.92	-11.34
$\eta$	-	0.034	65.84	-27.62
b) $\xi$	0.063	-	8.53	-5.26
$\eta$	-	0.063	47.29	-78.86
c) $\xi$	0.209	-	4.03	-0.95
$\eta$	-	0.209	42.12	-91.56

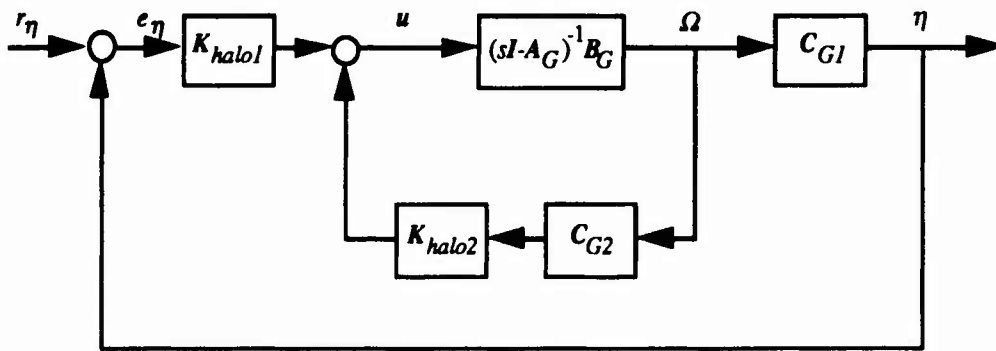


Figure 3.6: Representative Example Block Diagram

constant average steady state  $\Delta V$  per day. Two-axes control using  $\xi$ -axis provided much tighter resultant halo orbits for the same propulsion cost.

These two findings are a result of computing the guidance law using regulator theory and then commanding an input to be tracked by the closed-loop system. This procedure effectively closes an inner loop containing the states and associated gains which are not being commanded to track; an outer loop is then closed which contains the states which are tracked. Figure 3.6 shows these loops for a representative linear quadratic regulator example using the dynamics of the halo orbit guidance problem. Figure 3.7 plots the example's control acceleration-to-reference input transfer function ( $\frac{u}{r_\eta}$ ) for the

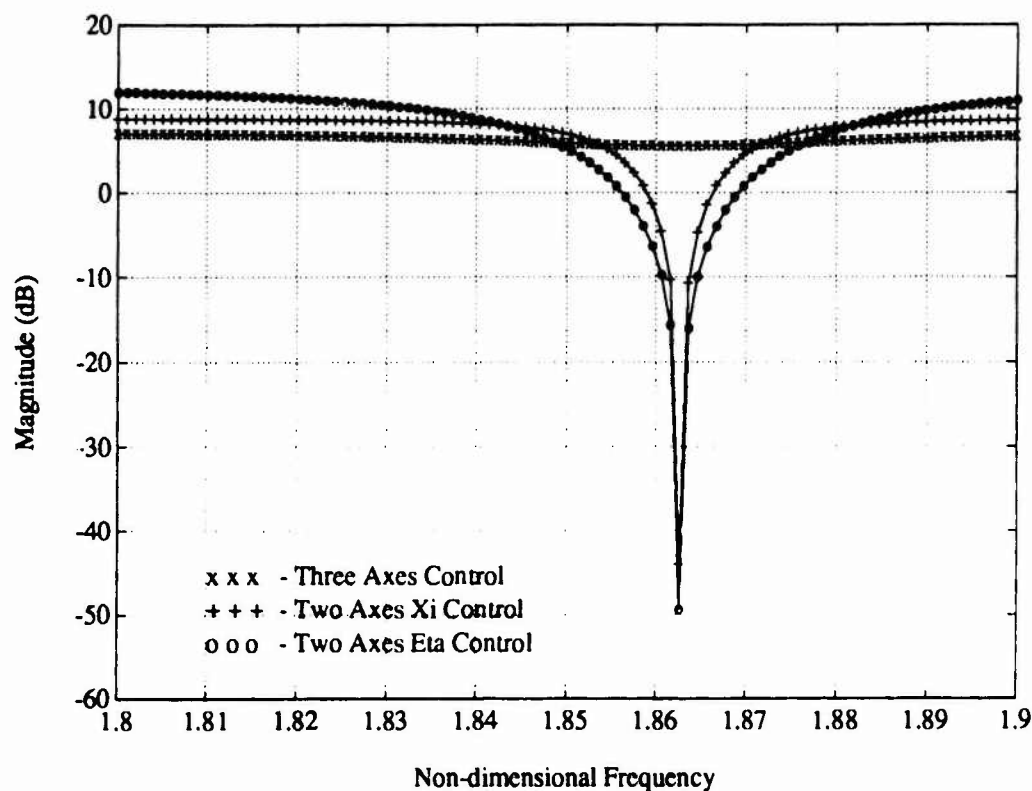


Figure 3.7: Control Acceleration Transfer Function ( $\frac{u}{r_\eta}$ ) for the Three and Two Axes Control Example

three-axes and two-axes control cases. At the frequency of interest (1.862647), three-axes control takes significantly more control acceleration than either of the two-axes control cases. Tracking accuracy is given by the magnitude of the output-to-reference input transfer function ( $\frac{\eta}{r_\eta}$ ) plotted in Fig. 3.8. "Good" command following for this example would occur at a magnitude of 0 dB. Hence, three-axes control has the best tracking performance followed by two-axes  $\xi$  control; two-axes  $\eta$  control has the worst tracking performance. Note that the trends shown in this representative example are the same as the trends shown in Tables 3.3 and 3.4. Thus, two-axes  $\xi$  control is used in the

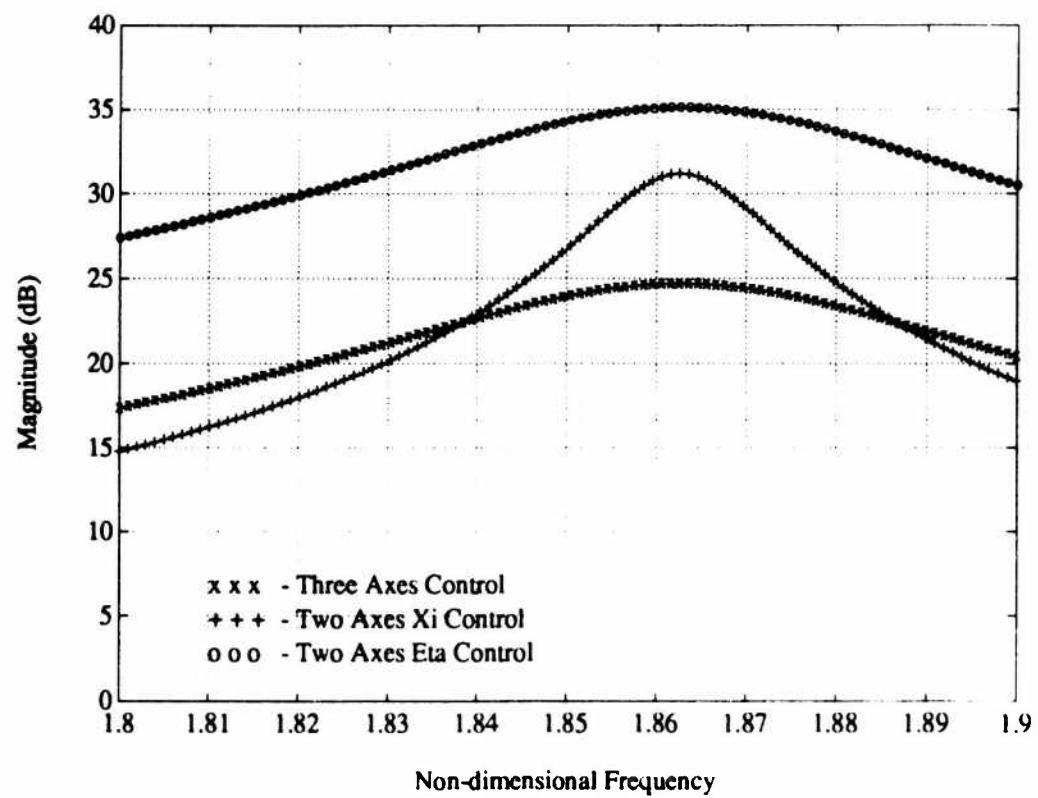


Figure 3.8: Closed-Loop Transfer Function ( $\frac{\eta}{r_\eta}$ ) for the Three and Two Axes Control Example

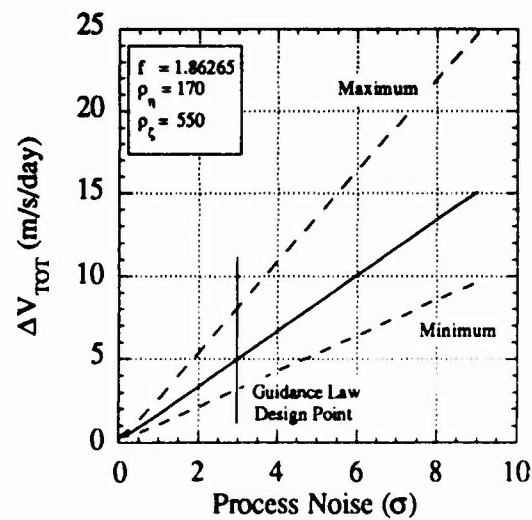


remaining simulations because at the frequency of interest it requires the least control acceleration for the best command following.

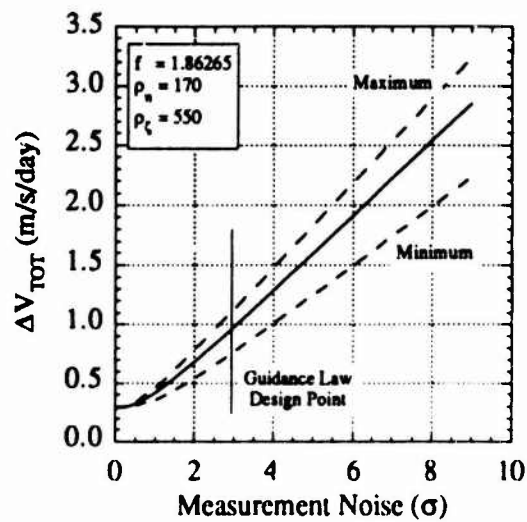
#### 3.4.4 Noise Characteristics Parametric Study

The steady state solution to the observer Ricatti equation is the error covariance associated with the estimated system states. Equation (3.19) shows the error covariance is a function of  $\Pi_d$  and  $\Pi_m$ . The noise statistics used in the simulations are given in Table 3.1. These statistics are consistent with the tracking accuracy study contained in the flight dynamics study [24]. Figure B.6 (a) in Appendix B.4 shows the average standard deviation of the position and velocity state as a function of the standard deviation of the process noise; Fig. B.6 (b) gives the average standard deviation of the velocity state. In both figures, the fixed power spectrum of the measurement noise is assumed to be  $2.665 \text{ m}^2/\text{s}$  in each axis. The average standard deviation of the position state is defined as the numerical average of the position singular values of the error covariance matrix. The similar definition applies to the average standard deviation of the velocity state.

A monte carlo analysis was completed to quantify the effect of these noise statistics on the average steady state  $\Delta V$  per day for halo orbit maintenance. Thirty 150 day simulations were run and the resultant average steady state  $\Delta V$  per day obtained. In all cases, the reference input to the simulation was a clockwise circular halo orbit with a radius of 3500 km and a non-dimensional frequency of 1.862647. Mid-range weighting parameters were also used. Figure 3.9 shows essentially a linear relationship between the amount of process and measurement noise and the resultant average steady state  $\Delta V$  per day. The dashed lines show the minimum and maximum values obtained in



(a)



(b)

Figure 3.9: Effect of Noise on Halo Orbit Station-keeping Cost

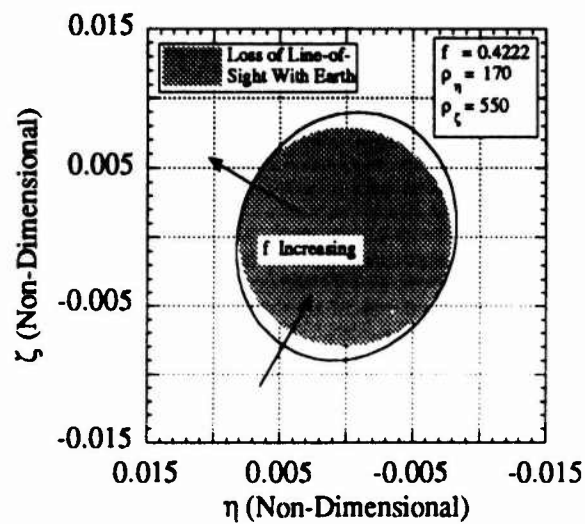
the 30 simulations. The average steady state  $\Delta V$  per day found in Table 3.2 corresponds to zero process noise and zero measurement noise.

### 3.4.5 Halo Orbit Characteristics Parametric Study

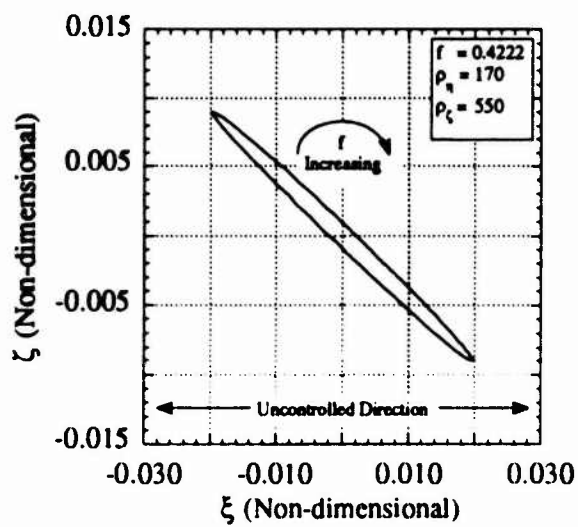
The position weighting factors,  $\rho_\eta$  and  $\rho_\zeta$ , and the halo orbit frequency were varied to determine the effects of each. Non-dimensional frequency was varied from 0.2 to 7.4 for each case. As before, the reference input to the simulation was a clockwise circular halo orbit with a radius of 3500 km. The duration of each simulation was 150 days.

Appendix B.5 gives the results of this parametric study as a function of halo orbit frequency. In each case, the resultant steady state halo orbit was an ellipse. For halo orbits with clockwise orbital rotation, Fig. 3.10 shows, qualitatively, the effect on the halo orbit of increasing the desired halo orbit frequency. The minimum deviation from a purely vertical orientation was obtained at a non-dimensional frequency of 1.47. As the halo orbit non-dimensional frequency deviated from the system's natural frequency (1.862647), velocity requirements in both axes increased rapidly. When non-dimensional frequency was reduced by 1, the average steady state  $\Delta V$  per day increased by a factor of 30. For an increase in non-dimensional frequency of 1, the average steady state  $\Delta V$  per day increased by a factor of 50.

The halo orbit non-dimensional frequency was then fixed at the natural frequency of the system and the position weighting factors were varied; these results are shown in Appendix B.6. The geometry of the halo orbit was essentially constant with respect to changes in the  $\zeta$ -axis weighting factor and steady state error decreased as the  $\eta$ -axis weighting factor increased. The orientation of the halo orbit was essentially constant for changes in either



(a) Front View



(b) Side View

Figure 3.10: Effect of Increasing Frequency on Halo Orbits with Clockwise Orbital Rotation

weighting factor. Due to the uncoupling of the linearized equations of motion, the velocity required in the  $\xi$ -axis was only influenced by the weighting factor in the  $\eta$ -axis; the velocity required increased as the weighting factor increased. Similarly, the velocity required in the  $\zeta$ -axis was only influenced by the weighting factor in the  $\zeta$ -axis. However, in this case, the velocity required decreased as the weighting factor increased. This was due to the  $\zeta$ -axis originally being stable and the  $\xi - \eta$  axes having to be stabilized by the guidance law.

## Chapter 4

### Rendezvous Targeting

Terminal phase rendezvous for the Gemini, Apollo and Space Shuttle missions was executed from stable elliptical orbits in the two-body problem. Two-body motion is planar; the rendezvous profile contains zero, or at least small amplitude sinusoidal, out-of-plane relative motion. Rendezvous targeting was done using Lambert's Theorem. By contrast, motion in the vicinity of the translunar equilibrium point is three-dimensional and unbounded. Further, Lambert's Theorem does not apply to motion in the three-body problem.

This chapter considers the terminal phase rendezvous of two spacecraft about the translunar equilibrium point. It assumes the target vehicle is in a small radius halo orbit and is controlling its own orbit using an unknown guidance law; the target vehicle remains passive with respect to the rendezvous profile. The chaser vehicle is in an independent small radius halo orbit and executes all rendezvous maneuvers. This chapter begins by developing the state equations for the target and chaser vehicles. The targeting law is then derived; this derivation is loosely equivalent to the rendezvous application of Hill's equations in the two-body problem. Lastly, nonlinear simulation results are presented.

#### 4.1 State Equations

The target vehicle orbits described in Chapter 3 can be approximated by an ellipse inclined to the  $\eta - \zeta$  plane. The equations of motion for this

approximation are

$$\Psi_{tp} = \begin{bmatrix} \xi_{tmax} \sin(ft + \psi_\xi) \\ \eta_{tmax} \sin(ft + \psi_\eta) \\ \zeta_{tmax} \sin(ft + \psi_\zeta) \end{bmatrix} \quad \text{and} \quad \Psi_{tv} = \dot{\Psi}_{tp} \quad (4.1)$$

which leads to the state equation

$$\begin{bmatrix} \dot{\Psi}_{tp} \\ \dot{\Psi}_{tv} \end{bmatrix} = A_p \begin{bmatrix} \Psi_{tp} \\ \Psi_{tv} \end{bmatrix} \quad (4.2)$$

where

$$A_p = \begin{bmatrix} 0 & I \\ -f^2 I & 0 \end{bmatrix} \quad (4.3)$$

and  $f$  is the halo orbit frequency. The subscripts  $( )_{tp}$  and  $( )_{tv}$  denote the target vehicle's position and velocity, respectively.

Since the halo orbits being considered have a small radius, the linearized equations of motion, Eq. (2.40), for the chaser vehicle can be used. Further, during a rendezvous profile the chaser vehicle will terminate its own halo orbit guidance. Hence, the chaser vehicle's state equation becomes

$$\begin{bmatrix} \dot{\Omega}_{cp} \\ \dot{\Omega}_{cv} \end{bmatrix} = A_G \begin{bmatrix} \Omega_{cp} \\ \Omega_{cv} \end{bmatrix} \quad (4.4)$$

where  $A_G$  is defined by Eq. (2.43) and the subscripts  $( )_{cp}$  and  $( )_{cv}$  denote the chaser vehicle's position and velocity, respectively.

Defining the relative position and velocity as

$$\begin{bmatrix} \delta_p \\ \delta_v \end{bmatrix} \triangleq \begin{bmatrix} \Omega_{cp} - \Psi_{tp} \\ \Omega_{cv} - \Psi_{tv} \end{bmatrix} \quad (4.5)$$

leads to the relative state equation

$$\begin{bmatrix} \dot{\delta}_p \\ \dot{\delta}_v \\ \dot{\Psi}_{tp} \\ \dot{\Psi}_{tv} \end{bmatrix} = \begin{bmatrix} A_G & \vdots & (A_G - A_p) \\ \dots & \dots & \dots \\ 0 & \vdots & A_p \end{bmatrix} \begin{bmatrix} \delta_p \\ \delta_v \\ \Psi_{tp} \\ \Psi_{tv} \end{bmatrix} \quad (4.6)$$

Equation (4.6) can be solved analytically

$$\begin{bmatrix} \delta_p(t_2^-) \\ \delta_v(t_2^-) \\ \Psi_{tp}(t_2^-) \\ \Psi_{tv}(t_2^-) \end{bmatrix} = \begin{bmatrix} \phi_{11} & \phi_{12} & \phi_{13} & \phi_{14} \\ \phi_{21} & \phi_{22} & \phi_{23} & \phi_{24} \\ 0 & 0 & \phi_{33} & \phi_{34} \\ 0 & 0 & \phi_{43} & \phi_{44} \end{bmatrix} \begin{bmatrix} \delta_p(t_1^+) \\ \delta_v(t_1^+) \\ \Psi_{tp}(t_1^+) \\ \Psi_{tv}(t_1^+) \end{bmatrix}. \quad (4.7)$$

where  $t_1$  and  $t_2$  denote the initiation and final times of the rendezvous, respectively. Also, the state transition matrix is a function of exponentially increasing and decreasing terms as well as sinusoidal terms at three different natural frequencies;  $\Phi(t_2, t_1)$  is further detailed in Appendix A.2. The superscripts  $(-)$  and  $(+)$  denote immediately before and immediately after a specified time, respectively.

## 4.2 Targeting Law

The necessary and sufficient conditions for rendezvous are that the relative position and velocity at the time of rendezvous be a specified value. Hence,  $\delta_p(t_2^+)$  and  $\delta_v(t_2^+)$  are known parameters. Consider a two maneuver terminal phase rendezvous sequence where the first maneuver is executed at the beginning of the rendezvous ( $t_1$ ) and designed so that the chaser vehicle will coast to the specified relative position at the time of rendezvous ( $t_2$ ); the second maneuver is then executed to satisfy the specified relative velocity condition.

The terminal phase initiation maneuver ( $TI$ ) is defined as

$$\Delta V_{TI} \triangleq \Omega_{cv}(t_1^+) - \Omega_{cv}(t_1^-) = \delta_v(t_1^+) - \delta_v(t_1^-). \quad (4.8)$$

Given the first row of the state transition matrix from Eq. (4.7), Eq. (4.8) can be expressed in terms of the specified position at the end of the rendezvous; the



initial relative position and velocity; and the chaser vehicle's initial position and velocity

$$\Delta \mathbf{V}_{TI} = \phi_{12}^{-1} \left[ \delta_p(t_2^+) + \{\phi_{13} - \phi_{11}\} \delta_p(t_1^-) + \{\phi_{14} - \phi_{12}\} \delta_v(t_1^-) - \phi_{13} \Omega_{cp}(t_1^-) - \phi_{14} \Omega_{cv}(t_1^-) \right]. \quad (4.9)$$

Note that this targeting law requires only relative state information, which can be provided by an onboard rendezvous navigation filter using proximity sensors, and chaser vehicle state information. Hence, no target vehicle specific information is required. Additionally, Eq. (4.9) contains a numerical singularity at specific transfer times. That is, when

$$(t_2 - t_1) = \frac{k\pi}{1.786178} \sim k \, 7.637724 \text{ days}; \quad k = 1, 2, 3, \dots \quad (4.10)$$

the  $\phi_{12}$  element becomes zero causing the  $\phi_{12}$  submatrix to become singular. Thus,  $\phi_{12}^{-1}$  does not exist. The  $\phi_{12}$  element corresponds to the uncoupled  $\zeta$ -axis in the linearized equations of motion. The  $\zeta$ -component is a sinusoidal function and becomes zero twice during a cycle at its natural frequency (1.786178). These singularities do not limit this research because the transfer times considered here are much shorter than any singularity time.

Lastly, the terminal phase final maneuver ( $TF$ ) is defined as

$$\Delta \mathbf{V}_{TF} \triangleq \Omega_{cv}(t_2^+) - \Omega_{cv}(t_2^-) = \delta_v(t_2^+) - \delta_v(t_2^-). \quad (4.11)$$

### 4.3 Simulation Results

A nonlinear simulation was developed to model the three-body terminal phase rendezvous problem (see Chapter 7). For analysis purposes, an option exists which will place the target vehicle in a planar circular orbit inclined to the  $\eta$ - $\zeta$  plane by a specified incline angle rather than using an actual

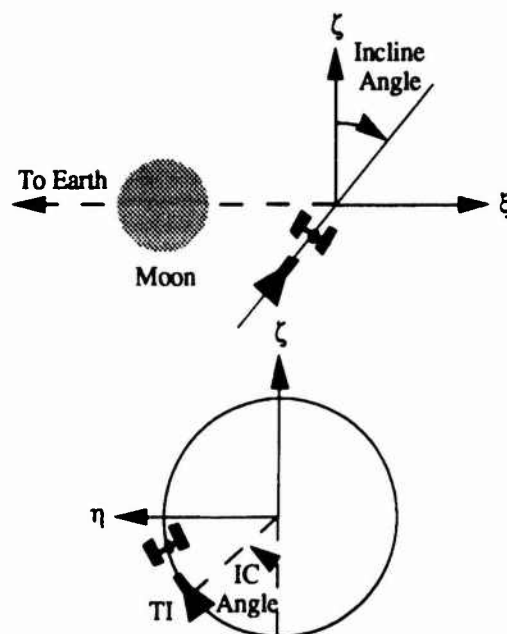


Figure 4.1: Incline and Initial Condition Angle Definitions

halo orbit. This option eliminates the target vehicle trajectory approximation used in the development of Eq. (4.9). In addition, an initial condition angle was defined to indicate the position on the halo orbit of the *TI* maneuver. Figure 4.1 shows the geometry of these angles. Several profiles were executed in order to investigate the characteristics of the three-body rendezvous problem. For each profile, clockwise orbits were used. The targeted position and velocity offset at rendezvous was specified to be zero in all cases.

#### 4.3.1 *TI* Targeting Law Error Parametric Study

The first three-body rendezvous characteristic investigated was final position error at the time of rendezvous due to the *TI* targeting law. The targeting law in Eq. (4.9) leads to a certain amount of error at the time of

rendezvous due to the target vehicle's trajectory approximation introduced in its development. Errors from the linearization of the equations of motion for the chaser vehicle have been removed by iterating on the specified relative position at the time of rendezvous within the simulation; this type of iteration technique is also used in the Space Shuttle rendezvous targeting software.

Figure 4.2 (a) gives the results for a clockwise halo orbit as a function of transfer time and initial condition angle. Figure 4.2 (b) shows constant error contours from Fig. 4.2 (a). Figure 4.2 (c) plots the side view of the target vehicle trajectory using the inclined ellipse approximation (dotted line) with the side view of the actual halo orbit (solid line). The maximum final position error occurs when  $TI$  occurs at the left or right sides of the halo orbit (initial condition angle approximately 90 or 270 deg). Further, the final position error was generally in the out-of-plane direction. Figure 4.2 (c) show that these points of maximum error also corresponds to the points of maximum curvature of the actual halo orbit. For all profiles, the chaser vehicle initiated the rendezvous profile approximately 19 km behind the target vehicle.

To correct for this targeting law error, a midcourse correction maneuver was added to the rendezvous profile. For demonstration purposes, the transfer time was held constant at 9 hrs and the initial condition angle was fixed at 46.08 deg; the transfer time and initial condition angle were arbitrarily chosen to be these values to be consistent with the planar circular orbit baseline case that results in a completely "in-plane" rendezvous profile. Figure 4.3 shows the results for one midcourse correction maneuver executed between  $TI$  and  $TF$  minus one hour. The final position error decreased rapidly from 1122 km to 18 km while the total propulsion cost of the rendezvous increased only slightly from 1.25 m/s to 1.78 m/s. Hence, the addition of midcourse cor-

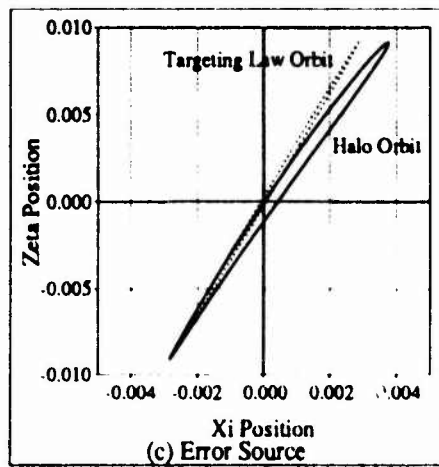
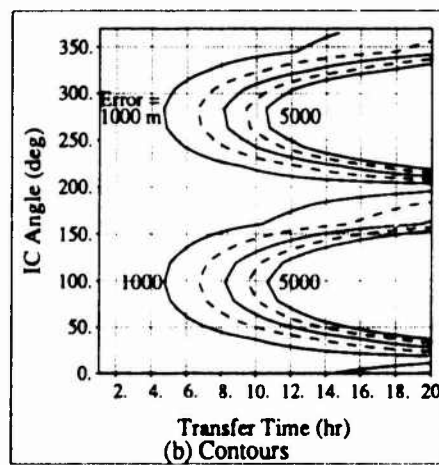
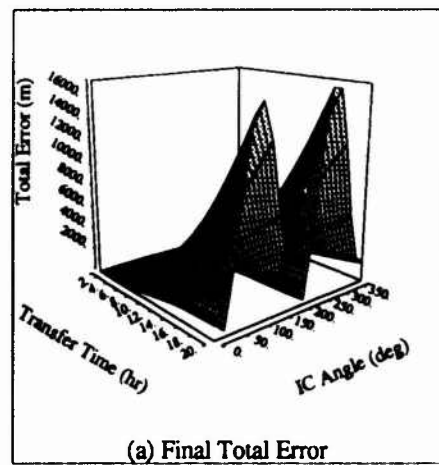


Figure 4.2: *TI* Targeting Law Error

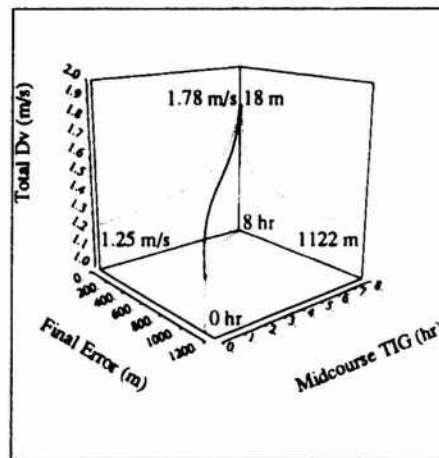


Figure 4.3: Midcourse Correction Maneuver Placement

rection maneuvers can substantially reduce errors due to the target vehicle's trajectory approximation used in the development of Eq. (4.9). The optimal location of a midcourse correction maneuver can not be determined solely from these data since that analysis requires a rendezvous navigation filter to be present.

#### 4.3.2 Constant Incline Angle Parametric Study

The second three-body rendezvous characteristic investigated was the effect of transfer time and initial condition angle on the geometry of the rendezvous profile. A planar circular orbit was used to insure final position errors were less than one meter. The incline angle was fixed at 22.85 deg which corresponded to the incline angle of the actual halo orbit used in this research. Finally, the chaser vehicle initiated the rendezvous profile 19 km behind the target vehicle in a coelliptic orbit.

Figure 4.4 (a) shows the maximum out-of-plane relative position

achieved by the rendezvous profile as a function of the input parameters. The out-of-plane component results from the coupling of the  $\xi - \eta$  axes in the equations of motion. Its magnitude is greatest when the rendezvous profile is initiated at the top or bottom of the orbit (initial condition angle approximately 0 or 180 deg). These points correspond to the points of maximum distance from the equilibrium point along the action line of gravitational and centrifugal forces. Figure 4.4 (b) gives the total propulsion cost of the rendezvous profile; Fig. 4.4 (c) overlays a plot of a minimum out-of-plane rendezvous profile (dashed lines) on constant total propulsion cost contours (solid lines). Two characteristics can be observed from these plots. First, for every initial condition angle, there is a transfer time which produce a minimum total propulsion cost of the rendezvous profile (eg. 180 deg, 13 hrs). Second, total propulsion costs increase with out-of-plane relative motion.

### 4.3.3 Constant Transfer Time Parametric Study

The third three-body rendezvous characteristic investigated was the effect of incline angle and initial condition angle on the geometry of the rendezvous profile. As before, a planar circular orbit was used to insure final position errors were less than one meter. The transfer time was fixed at the baseline case value of 9 hrs and, once again, the chaser vehicle initiated the rendezvous profile 19 km behind the target vehicle in a coelliptic orbit.

Figure 4.5 shows the same general information as Fig. 4.4 except incline angle has replaced transfer time. These results show that a minimum total propulsion cost rendezvous profile is a function of incline angle as well as initial condition angle and transfer time. Also, when transfer time is held constant, the minimum total propulsion cost rendezvous profiles have

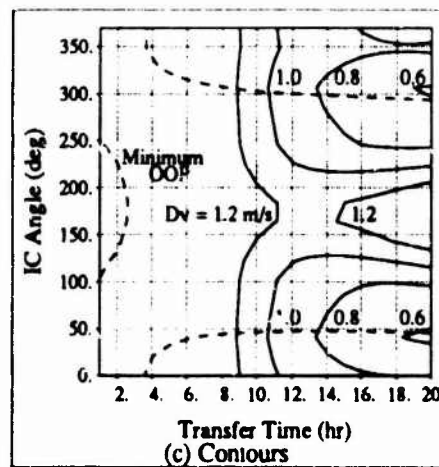
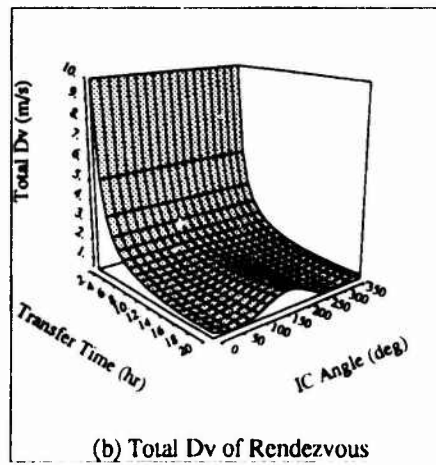
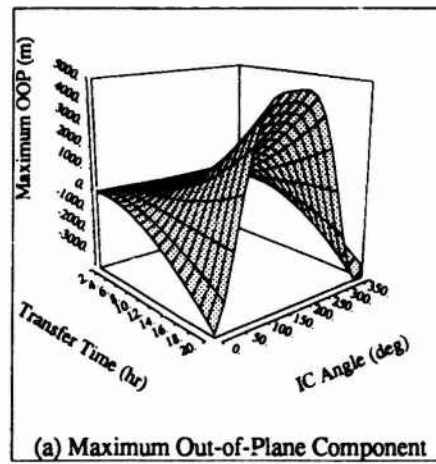


Figure 4.4: Constant Incline Angle Characteristics

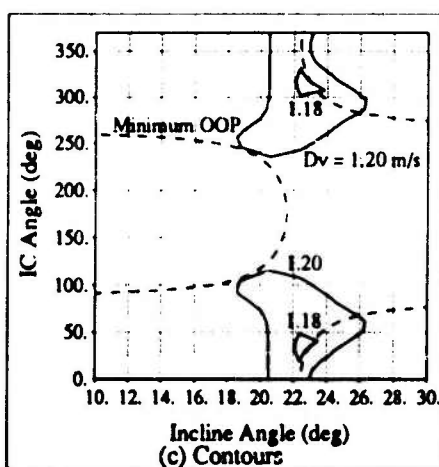
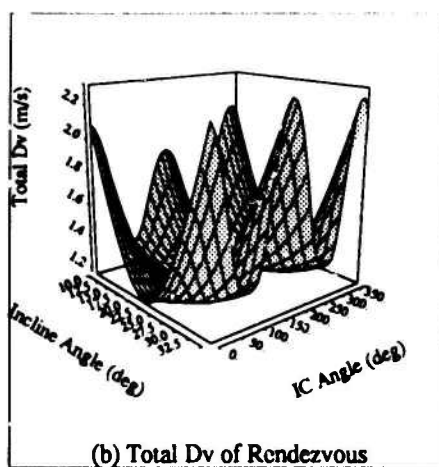
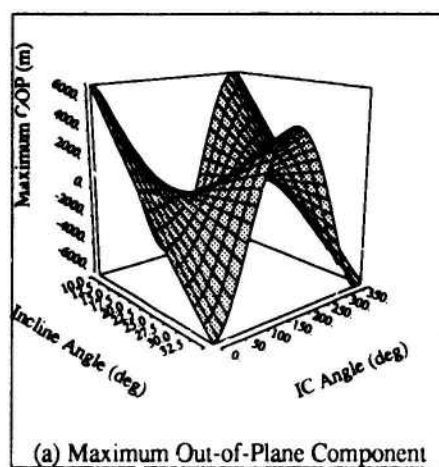


Figure 4.5: Constant Transfer Time Characteristics



"in-plane" relative motion.

#### 4.3.4 Representative Relative Trajectories

Figure 4.6 summarizes the geometry of the rendezvous profile as initial condition and incline angles change. Figure 4.6 (c) gives a completely "in-plane" profile executed on the left side of the orbit. Figures 4.6 (a) and (b) show that for a fixed incline angle and increasing initial condition angle in the vicinity of the "in-plane" profile, the out-of-plane component switches from away from the Moon (positive  $\xi$ ) to toward the Moon (negative  $\xi$ ). Figures 4.6 (d) and (e) show this same characteristic for a fixed initial condition angle and decreasing incline angle in the vicinity of the "in-plane" profile.

Figure 4.6 also shows that the relative trajectory is three-dimensional. To further examine this conclusion, the torsion and rate of change of torsion was computed for the relative trajectory at the initiation of the rendezvous profile ( $TI$ ). Torsion is a measure of the twisting of a curve and is computed from

$$\tau = \frac{(\dot{\delta}_p \times \ddot{\delta}_p) \cdot \ddot{\delta}_p}{\|\dot{\delta}_p \times \ddot{\delta}_p\|^2} \quad (4.12)$$

In addition, the rate of change of torsion is given by

$$\dot{\tau} = \frac{(\dot{\delta}_p \times \ddot{\delta}_p) \cdot \ddot{\delta}_p + (\ddot{\delta}_p \times \ddot{\delta}_p) \cdot \ddot{\delta}_p - 2\tau(\dot{\delta}_p \times \ddot{\delta}_p) \cdot (\ddot{\delta}_p \times \ddot{\delta}_p)}{\|\dot{\delta}_p \times \ddot{\delta}_p\|^2} \quad (4.13)$$

Figures 4.7 (a) and (b) plot the relative trajectory's torsion and rate of change of torsion at the beginning of the terminal phase as a function of initial condition and incline angles. Transfer time was held constant at 9 hrs. A necessary condition for the relative trajectory to be two-dimensional is that the torsion and rate-of-change of torsion be zero at the initiation of

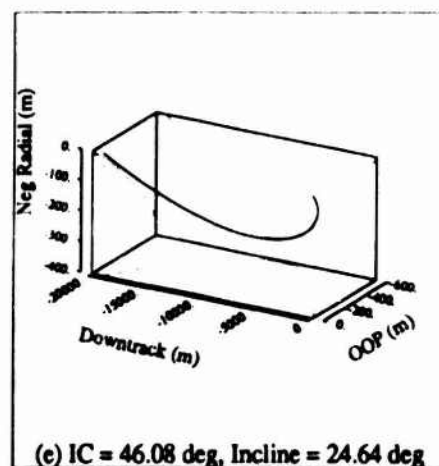
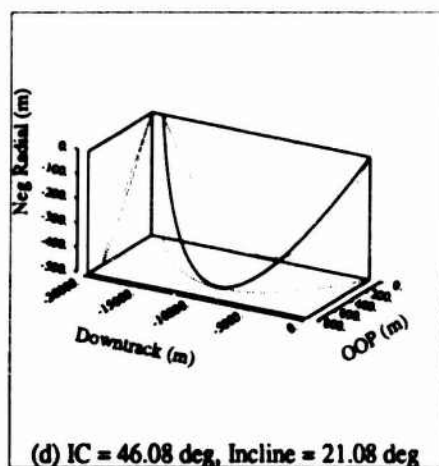
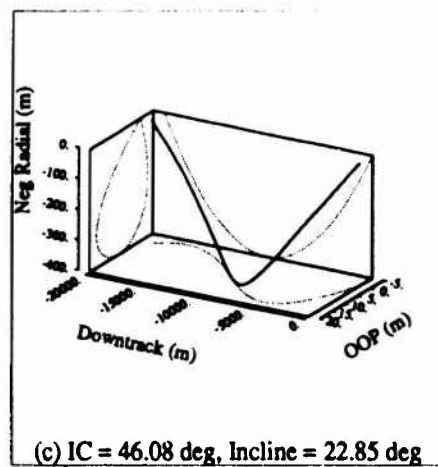
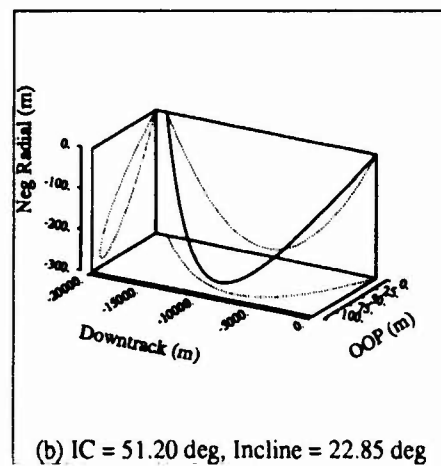
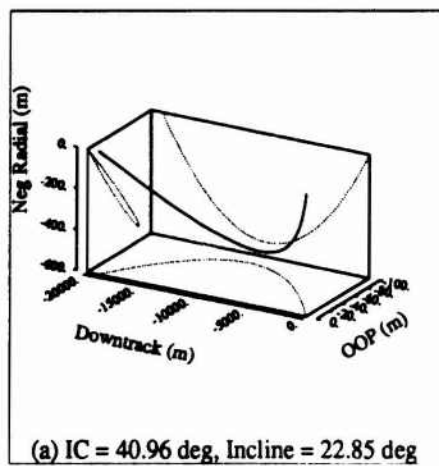


Figure 4.6: Representative Relative Motion

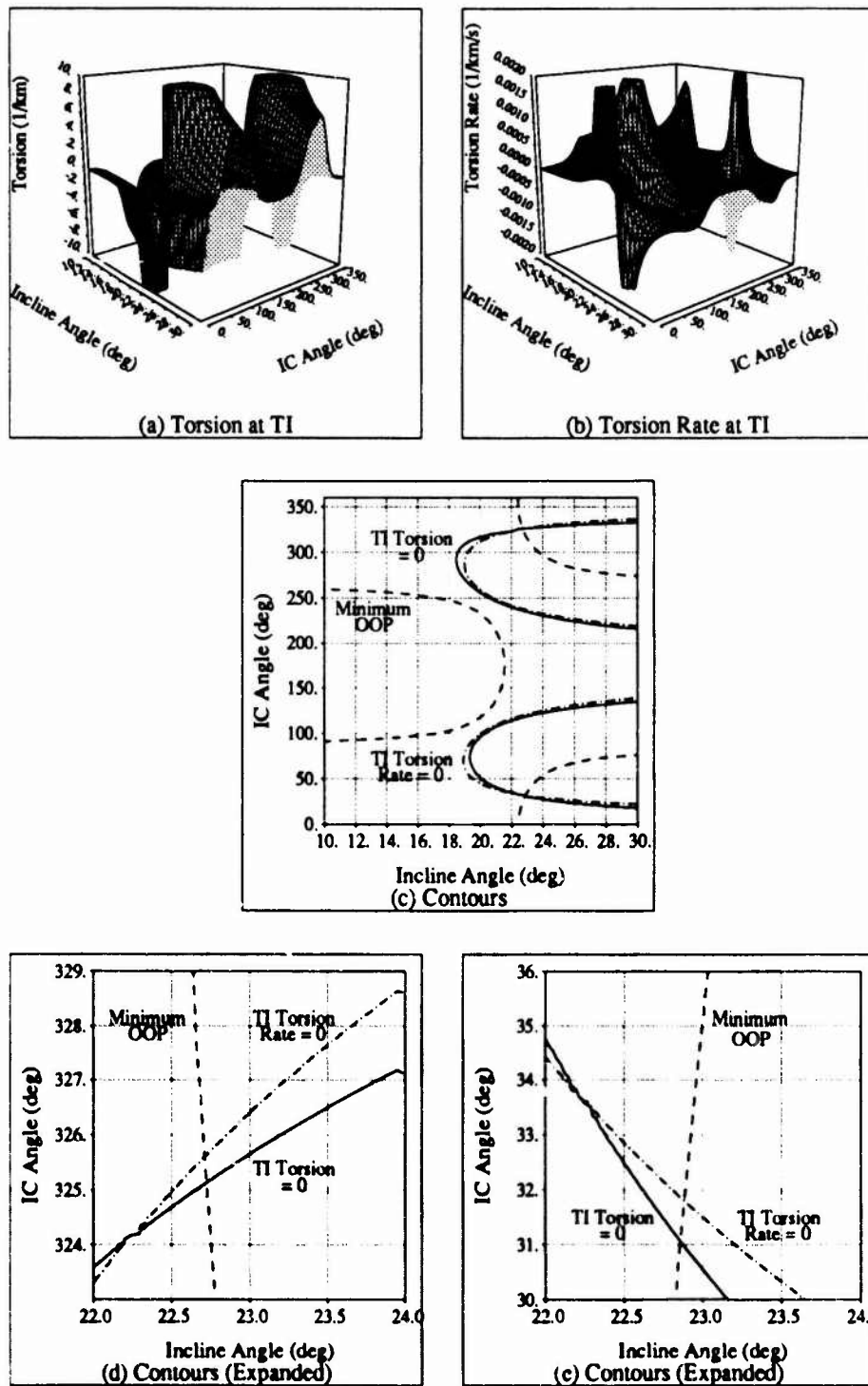


Figure 4.7: Relative Trajectory Torsion and Rate of Change of Torsion at Terminal Phase Rendezvous Initiation

the rendezvous profile. Figure 4.7 (c) shows contours of torsion and the rate of change of torsion equal to zero. Also shown is the minimum out-of-plane contour from Fig. 4.5. Figures 4.7 (d) and (e) are expanded views of the intersections of the three contours given in Fig. 4.7 (c). For the relative trajectory to be two-dimensional and lie in the target vehicle's halo orbit plane, the three contours must intersect at the same point. Hence, two-dimensional relative trajectories which lie in the target vehicle's halo orbit plane do not exist. However, the minimum out-of-plane contour from Fig. 4.5 represents a maximum out-of-plane distance on the order of 10 m. Thus, these relative trajectories are essentially "in-plane" and will be referred to as such in this research.

## Chapter 5

### Rendezvous Navigation

The Apollo onboard rendezvous navigation filter represents the first application of Kalman filtering techniques to the rendezvous navigation problem. This problem can be defined as determining the relative state of the two spacecrafts performing the rendezvous. Muller and Kachmar [40] showed the equivalence of optimally estimating the relative state or optimally estimating the inertial state of one spacecraft and subtracting it from an externally supplied inertial state of the other spacecraft. This estimation is optimal in the sense that it yields the minimum relative state error at the time of measurement incorporation, not necessarily the minimum relative state error over the entire navigation period. Nevertheless, to reduce the complexity of the rendezvous navigation filter, this formulation was used in the Apollo and Space Shuttle rendezvous navigation filters.

For this research, the rendezvous navigation filter will estimate the inertial state of the chaser vehicle; it is assumed that either the target vehicle or its mission control center will supply the chaser vehicle with target vehicle state information at the time of each measurement. The Space Shuttle rendezvous navigation filter is mechanized in this manner except only one target vehicle state vector is required at the beginning of the rendezvous profile. Target vehicle state information is required at every measurement in this research because the target vehicle requires active guidance to maintain its own halo orbit and it is assumed that this guidance law is unknown to the chaser vehicle.

The chaser vehicle would have to know the target vehicle's guidance law in order to propagate target vehicle state information in a manner similar to the Space Shuttle rendezvous navigation filter.

In this chapter, a continuous dynamics, discrete measurement extended Kalman filter is developed. The rendezvous navigation filter is formulated assuming the estimated states are the chaser vehicle's inertial state, unmodeled accelerations on the chaser vehicle, and measurement biases. The filter is implemented in the nonlinear simulation such that the chaser vehicle's inertial state is always estimated and the other estimation states are selectable. Initially, the dynamical system is developed. Then, the estimation state-error covariance matrix propagation and update equations are presented and the measurement-state relationships derived. Lastly, nonlinear simulation results are given to assess the performance of the rendezvous navigation filter.

## 5.1 Continuous-Discrete Kalman Filter

### 5.1.1 Dynamical System

The dynamical system for this problem can be described by a continuous nonlinear differential equation

$$\dot{\mathbf{X}}_c(t) = \mathbf{f}_1(\mathbf{X}_c(t)) + \mathbf{a}(t) \quad (5.1)$$

where  $\mathbf{f}_1(\mathbf{X}_c(t))$  is given by Eq. (2.27) and  $\mathbf{a}(t)$  represents unmodeled accelerations. Assume the unmodeled accelerations have the form of a first-order Gauss-Markov process

$$\dot{\mathbf{a}}(t) = \mathbf{A}_a \mathbf{a}(t) + \mathbf{w}_a(t) \quad (5.2)$$

where

$$\mathbf{A}_a = \text{diag}[a_{a11}, a_{a22}, a_{a33}, a_{a44}, a_{a55}, a_{a66}] \quad (5.3)$$

and  $\mathbf{w}_a(t)$  is white gaussian noise with zero mean and  $\mathbf{Q}_a$  fixed power spectrum. The discrete nonlinear measurements are modeled as

$$\mathbf{y}(t_k) = \mathbf{h}_1(\mathbf{X}_c(t_k)) + \mathbf{b}(t_k) + \mathbf{v}(t_k); \quad k = 1, 2, \dots \quad (5.4)$$

where  $\mathbf{h}_1(\mathbf{X}_c(t_k))$  represents the measurement-state relationships derived in Section 5.1.3. The measurement bias  $\mathbf{b}(t_k)$  is also modeled as a first-order Gauss-Markov process

$$\dot{\mathbf{b}}(t) = \mathbf{A}_b \mathbf{b}(t) + \mathbf{w}_b(t) \quad (5.5)$$

where

$$\mathbf{A}_b = \text{diag} [a_{b11}, a_{b22}, a_{b33}, a_{b44}, a_{b55}, a_{b66}] \quad (5.6)$$

and  $\mathbf{w}_b(t)$  is white gaussian noise with zero mean and  $\mathbf{Q}_b$  fixed power spectrum. The measurement noise  $\mathbf{v}(t_k)$  is also white gaussian noise with zero mean and  $\mathbf{R}_k$  covariance matrix.

Define an estimation state vector

$$\mathbf{Z}(t) \triangleq \begin{bmatrix} \mathbf{X}_c(t) \\ \mathbf{a}(t) \\ \mathbf{b}(t) \end{bmatrix}. \quad (5.7)$$

Combining Eqs. (5.1), (5.2), and (5.5) yields

$$\dot{\mathbf{Z}}(t) = \mathbf{f}_2(\mathbf{Z}(t)) + \mathbf{w}(t) \quad (5.8)$$

which for notational convenience will be written as

$$\dot{\mathbf{Z}} = \mathbf{f}_2 + \mathbf{w} \quad (5.9)$$

where

$$\mathbf{f}_2 \triangleq \mathbf{f}_2(\mathbf{Z}(t)) = \begin{bmatrix} \mathbf{f}_1(\mathbf{X}_c(t)) + \mathbf{a}(t) \\ \mathbf{A}_a \mathbf{a}(t) \\ \mathbf{A}_b \mathbf{b}(t) \end{bmatrix} \quad (5.10)$$

$$\mathbf{w} \triangleq \mathbf{w}(t) = \begin{bmatrix} \mathbf{0} \\ \mathbf{w}_a(t) \\ \mathbf{w}_b(t) \end{bmatrix}. \quad (5.11)$$

The white gaussian noise  $\mathbf{w}$  has zero mean and  $\mathbf{Q}$  fixed power spectrum where

$$\mathbf{Q} = \begin{bmatrix} 0 & 0 & 0 \\ 0 & \mathbf{Q}_a & 0 \\ 0 & 0 & \mathbf{Q}_b \end{bmatrix}. \quad (5.12)$$

Finally, Eq. (5.4) becomes

$$\mathbf{y}(t_k) = \mathbf{h}_2(\mathbf{Z}(t_k)) + \mathbf{v}(t_k) \quad (5.13)$$

which for notational convenience will be written as

$$\mathbf{y}_k = \mathbf{h}_{2k} + \mathbf{v}_k \quad (5.14)$$

where

$$\mathbf{h}_{2k} \triangleq \mathbf{h}_2(\mathbf{Z}(t_k)) = \mathbf{h}_1(\mathbf{X}_c(t_k)) + \mathbf{b}(t_k) \triangleq \mathbf{h}_{1k} + \mathbf{b}_k. \quad (5.15)$$

### 5.1.2 Propagation and Update Equations

Equations (5.9) and (5.14) give the standard form of the dynamical system for the continuous-discrete Kalman filter. The derivation of the propagation and update equations for this filter is well-known (see Gelb [41] for example); this derivation minimizes the magnitude of the expected value of the estimation error. The estimation state propagation equation is

$$\dot{\hat{\mathbf{Z}}} = \mathbf{E}[\mathbf{f}_2]. \quad (5.16)$$

Expanding  $\mathbf{f}_2$  about the estimated state in a Taylor series, taking the expectation and neglecting higher order terms yields

$$\dot{\hat{\mathbf{Z}}} = \mathbf{f}_2(\hat{\mathbf{Z}}(t)); \quad t_k \leq t \leq t_{k+1} \quad (5.17)$$



where sensor measurements are available at  $t_k$  and  $t_{k+1}$ . For notational convenience, Eq. (5.17) will be written as

$$\dot{\hat{\mathbf{Z}}} = \hat{\mathbf{f}}_2. \quad (5.18)$$

Propagation of the error covariance matrix  $\mathbf{P}(t)$  is done using

$$\dot{\mathbf{P}} = \mathbf{P}\mathbf{F}^T + \mathbf{F}\mathbf{P} + \mathbf{Q} \quad (5.19)$$

where  $\mathbf{Q}$  has the form given by Eq. (5.12) and

$$\mathbf{F} \triangleq \left. \frac{\partial \mathbf{f}_2(\mathbf{Z}(t))}{\partial \mathbf{Z}(t)} \right|_{\mathbf{Z}(t)=\hat{\mathbf{Z}}(t)}. \quad (5.20)$$

Equation (5.20) can be further reduced to

$$\mathbf{F} = \begin{bmatrix} \left. \frac{\partial \mathbf{f}_1(\mathbf{X}_c(t))}{\partial \mathbf{X}_c(t)} \right|_{\mathbf{X}_c(t)=\hat{\mathbf{X}}_c(t)} & \mathbf{I} & \mathbf{0} \\ \mathbf{0} & \mathbf{A}_a & \mathbf{0} \\ \mathbf{0} & \mathbf{0} & \mathbf{A}_b \end{bmatrix} \quad (5.21)$$

which after compacting the notation becomes

$$\mathbf{F} = \begin{bmatrix} \frac{\partial \mathbf{f}_1}{\partial \hat{\mathbf{X}}_c} & \mathbf{I} & \mathbf{0} \\ \mathbf{0} & \mathbf{A}_a & \mathbf{0} \\ \mathbf{0} & \mathbf{0} & \mathbf{A}_b \end{bmatrix}. \quad (5.22)$$

Differentiating  $\mathbf{f}_1$ , given in Eq. (2.27), yields

$$\frac{\partial \mathbf{f}_1}{\partial \hat{\mathbf{X}}_c} = \begin{bmatrix} 0 & 0 & 0 & 1 & 0 & 0 \\ 0 & 0 & 0 & 0 & 1 & 0 \\ 0 & 0 & 0 & 0 & 0 & 1 \\ f_{41} & f_{42} & f_{43} & 0 & 2 & 0 \\ f_{42} & f_{52} & f_{53} & -2 & 0 & 0 \\ f_{43} & f_{53} & f_{63} & 0 & 0 & 0 \end{bmatrix} \quad (5.23)$$

where

$$f_{41} = 1 + \frac{3\mu(\hat{x}_c - (1 - \mu))^2}{\rho_{MC}^5} - \frac{\mu}{\rho_{MC}^3} + \frac{3(1 - \mu)(\hat{x}_c + \mu)^2}{\rho_{EC}^5} - \frac{(1 - \mu)}{\rho_{EC}^3} \quad (5.24)$$

$$f_{42} = \frac{3\mu(\hat{x}_c - (1 - \mu))\hat{y}_c}{\rho_{MC}^5} + \frac{3(1 - \mu)(\hat{x}_c + \mu)\hat{y}_c}{\rho_{EC}^5} \quad (5.25)$$

$$f_{43} = \frac{3\mu(\hat{x}_c - (1 - \mu))\hat{z}_c}{\rho_{MC}^5} + \frac{3(1 - \mu)(\hat{x}_c + \mu)\hat{z}_c}{\rho_{EC}^5} \quad (5.26)$$

$$f_{52} = 1 + \frac{3\mu\hat{y}_c^2}{\rho_{MC}^5} - \frac{\mu}{\rho_{MC}^3} + \frac{3(1 - \mu)\hat{y}_c^2}{\rho_{EC}^5} - \frac{(1 - \mu)}{\rho_{EC}^3} \quad (5.27)$$

$$f_{53} = \frac{3\mu\hat{y}_c\hat{z}_c}{\rho_{MC}^5} + \frac{3(1 - \mu)\hat{y}_c\hat{z}_c}{\rho_{EC}^5} \quad (5.28)$$

$$f_{63} = \frac{3\mu\hat{z}_c^2}{\rho_{MC}^5} - \frac{\mu}{\rho_{MC}^3} + \frac{3(1 - \mu)\hat{z}_c^2}{\rho_{EC}^5} - \frac{(1 - \mu)}{\rho_{EC}^3} \quad (5.29)$$

$$\rho_{MC} = \sqrt{(\hat{x}_c - (1 - \mu))^2 + \hat{y}_c^2 + \hat{z}_c^2} \quad (5.30)$$

$$\rho_{EC} = \sqrt{(\hat{x}_c + \mu)^2 + \hat{y}_c^2 + \hat{z}_c^2} \quad (5.31)$$

The ( )<sub>C</sub> subscript denotes the chaser vehicle. Finally, the estimation state and error covariance matrix are updated according to

$$\hat{\mathbf{Z}}^+ = \hat{\mathbf{Z}}^- + \mathbf{K}_k(\mathbf{y}_k - \hat{\mathbf{h}}_{2k}) \quad (5.32)$$

$$\mathbf{P}^+ = (\mathbf{I} - \mathbf{K}_k\mathbf{H}_k)\mathbf{P}^-(\mathbf{I} - \mathbf{K}_k\mathbf{H}_k)^T + \mathbf{K}_k\mathbf{R}_k\mathbf{K}_k^T \quad (5.33)$$

where the superscripts ( )<sup>-</sup> and ( )<sup>+</sup> denote immediately before and immediately after measurement incorporation, respectively, and

$$\mathbf{K}_k = \mathbf{P}^-\mathbf{H}_k^T(\mathbf{H}_k\mathbf{P}^-\mathbf{H}_k^T + \mathbf{R}_k)^{-1} \quad (5.34)$$

$$\hat{\mathbf{h}}_{2k} = \mathbf{E}[\mathbf{h}_{2k}] \quad (5.35)$$

$$\mathbf{H}_k \triangleq \left. \frac{\partial \mathbf{h}_2(\mathbf{Z}(t_k))}{\partial \mathbf{Z}(t_k)} \right|_{\mathbf{Z}(t_k)=\hat{\mathbf{Z}}(t_k^-)} \quad (5.36)$$

Expanding  $\mathbf{h}_2$  about the estimated state in a Taylor series, taking the expectation and neglecting the higher order terms in Eq. (5.35) yields

$$\hat{\mathbf{h}}_{2k} = \mathbf{h}_2(\hat{\mathbf{Z}}(t_k^-)). \quad (5.37)$$

Additionally, Eq. (5.36) can be further reduced to

$$\mathbf{H}_k = \left[ \left. \frac{\partial \mathbf{h}_1(\mathbf{X}_c(t_k))}{\partial \mathbf{X}_c(t_k)} \right|_{\mathbf{X}_c(t_k)=\hat{\mathbf{X}}_c(t_k^-)} \quad \mathbf{0} \quad \mathbf{I} \right] \quad (5.38)$$

which after compacting the notation becomes

$$\mathbf{H}_k = \left[ \frac{\partial \mathbf{h}_{1k}}{\partial \mathbf{X}_c} \quad \mathbf{0} \quad \mathbf{I} \right]. \quad (5.39)$$

In the next section,  $\mathbf{h}_{1k}$  is defined and  $\frac{\partial \mathbf{h}_{1k}}{\partial \mathbf{X}_c}$  is computed.

### 5.1.3 Measurement-State Relationships

Consider a set of measurements consisting of

$$\mathbf{h}_{1k} = \begin{bmatrix} R \\ \dot{R} \\ \phi \\ \theta \end{bmatrix} \quad (5.40)$$

where  $R$  is the relative range between the chaser and target vehicles,  $\dot{R}$  is the relative range rate, and  $\phi$  and  $\theta$  are the roll and pitch angles of the relative position vector in the chaser vehicle's body coordinates. The corresponding measurement bias vector is

$$\mathbf{b}_k = \begin{bmatrix} b_R \\ b_{\dot{R}} \\ b_\phi \\ b_\theta \end{bmatrix}. \quad (5.41)$$

Differentiating Eq. (5.40) yields

$$\frac{\partial \mathbf{h}_{1k}}{\partial \dot{\mathbf{X}}_c} = \begin{bmatrix} \frac{\partial R}{\partial \dot{\mathbf{X}}_c} \\ \frac{\partial R}{\partial \dot{\mathbf{X}}_c} \\ \frac{\partial \phi}{\partial \dot{\mathbf{X}}_c} \\ \frac{\partial \theta}{\partial \dot{\mathbf{X}}_c} \end{bmatrix}. \quad (5.42)$$

Assume the proximity sensor is located at a known position ( $\delta_S$ ) in the chaser vehicle's body coordinate system. Further, assume the chaser vehicle's attitude with respect to the local vertical inertial rectangular (LVIR) coordinate system and the orientation of the sensor's coordinate system are known. Hence, the transformations from LVIR to the body coordinate system ( $\mathbf{T}_{BL}$ ) and from the body to the sensor coordinate system ( $\mathbf{T}_{SB}$ ) can be computed. Finally, with the chaser vehicle's inertial position and velocity known, the transformation from the inertial to the LVIR coordinate system ( $\mathbf{T}_{LI}$ ) can also be computed.

If the state vector of the chaser and target vehicles is partitioned into inertial position and velocity,

$$\mathbf{X}_c = \begin{bmatrix} \mathbf{r}_c \\ \dots \\ \mathbf{v}_c \end{bmatrix} \quad (5.43)$$

$$\mathbf{X}_t = \begin{bmatrix} \mathbf{r}_t \\ \dots \\ \mathbf{v}_t \end{bmatrix} \quad (5.44)$$

then, the relative position and velocity vectors from the sensor location to the target vehicle can be written

$$\mathbf{R} = \mathbf{r}_t - \mathbf{r}_c - (\mathbf{T}_{BL}\mathbf{T}_{LI})^T \delta_S \quad (5.45)$$

$$\mathbf{V} = \mathbf{v}_t - \mathbf{v}_c. \quad (5.46)$$

From Eqs. (5.45) and (5.46), it follows that the relative range and range rate are

$$R = \|\mathbf{R}\| \quad (5.47)$$

$$\dot{R} = \frac{\mathbf{R} \cdot \mathbf{V}}{\|\mathbf{R}\|}. \quad (5.48)$$

Differentiating Eqs. (5.47) and (5.48) yield

$$\frac{\partial R}{\partial \dot{\mathbf{X}}_c} = \frac{\hat{\mathbf{R}}^T}{\|\hat{\mathbf{R}}\|} \frac{\partial \mathbf{R}}{\partial \dot{\mathbf{X}}_c} \quad (5.49)$$

$$\frac{\partial \dot{R}}{\partial \dot{\mathbf{X}}_c} = \left( \frac{\hat{\mathbf{V}}^T}{\|\hat{\mathbf{R}}\|} - \frac{\hat{\mathbf{R}}^T \hat{\mathbf{V}} \hat{\mathbf{R}}^T}{\|\hat{\mathbf{R}}\|^3} \right) \frac{\partial \mathbf{R}}{\partial \dot{\mathbf{X}}_c} + \frac{\hat{\mathbf{R}}^T}{\|\hat{\mathbf{R}}\|} \frac{\partial \mathbf{V}}{\partial \dot{\mathbf{X}}_c}. \quad (5.50)$$

Define three vectors which correspond to the columns of the LVIR to inertial coordinate system transformation matrix

$$\mathbf{T}_{IL} \triangleq \begin{bmatrix} \mathbf{T}_{IL1} & \mathbf{T}_{IL2} & \mathbf{T}_{IL3} \end{bmatrix} = \mathbf{T}_{LI}^T. \quad (5.51)$$

where

$$\mathbf{T}_{IL1} = \text{unit}(\mathbf{r}_c \times \mathbf{v}_c \times \mathbf{r}_c) \quad (5.52)$$

$$\mathbf{T}_{IL2} = -\text{unit}(\mathbf{r}_c \times \mathbf{v}_c) \quad (5.53)$$

$$\mathbf{T}_{IL3} = -\text{unit}(\mathbf{r}_c). \quad (5.54)$$

Also, define the vector

$$\mathbf{C}_1 \triangleq \mathbf{T}_{BL}^T \delta_s \quad (5.55)$$

which is not a function of  $\mathbf{X}_c$ . Then, differentiating Eq. (5.45) yields

$$\frac{\partial \mathbf{R}}{\partial \dot{\mathbf{X}}_c} = \begin{bmatrix} -\mathbf{I} & \mathbf{0} \end{bmatrix} - \mathbf{C}_1(1) \frac{\partial \mathbf{T}_{IL1}}{\partial \dot{\mathbf{X}}_c} - \mathbf{C}_1(2) \frac{\partial \mathbf{T}_{IL2}}{\partial \dot{\mathbf{X}}_c} - \mathbf{C}_1(3) \frac{\partial \mathbf{T}_{IL3}}{\partial \dot{\mathbf{X}}_c}. \quad (5.56)$$

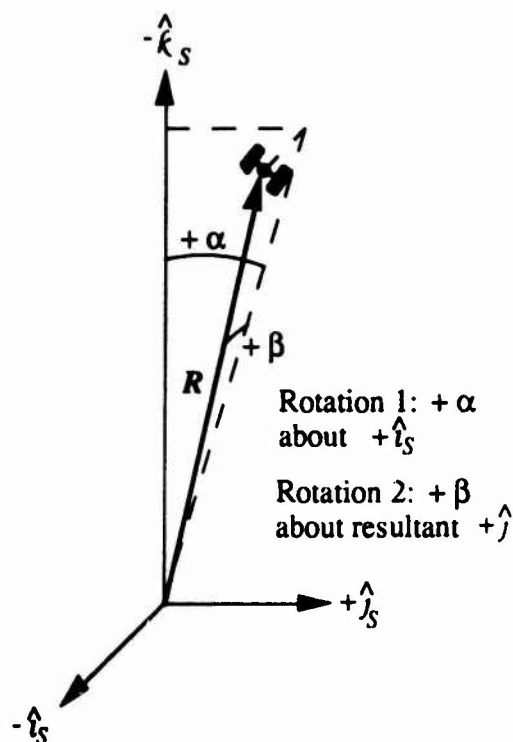


Figure 5.1: Angle Measurements

Further, differentiating Eq. (5.46) gives

$$\frac{\partial V}{\partial \dot{X}_c} = \begin{bmatrix} \mathbf{0} & : & -\mathbf{I} \end{bmatrix}. \quad (5.57)$$

Figure 5.1 shows the two angles of the relative position vector measured by the sensor. These angles are in the sensor coordinate frame and are computed by

$$\alpha = \arctan \left( \frac{\mathbf{R} \cdot \hat{j}_S}{\mathbf{R} \cdot -\hat{k}_S} \right) \quad (5.58)$$

$$\beta = \arctan \left( \frac{\mathbf{R} \cdot -\hat{i}_S}{\sqrt{(\mathbf{R} \cdot \hat{j}_S)^2 + (\mathbf{R} \cdot -\hat{k}_S)^2}} \right). \quad (5.59)$$

Figure 5.2 gives the two angles used by the extended Kalman filter; they are

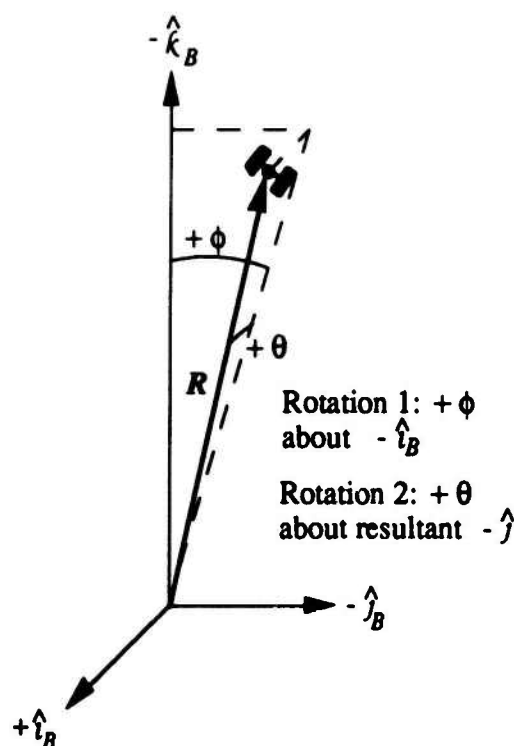


Figure 5.2: Computed Angles

the preferred line-of-sight angles because they have an intuitive interpretation to the crewman on-board the chaser vehicle. These angles are in the chaser vehicle's body coordinate system and can be computed directly from the sensor measured angles by

$$\phi = \arcsin \left( \frac{\left( T_{SB}(1,2) \sin \beta - T_{SB}(2,2) \sin \alpha \cos \beta \right) + T_{SB}(3,2) \cos \alpha \cos \beta}{\cos \theta} \right) \quad (5.60)$$

$$\theta = \arcsin \left( \frac{-T'_{SB}(1,1) \sin \beta + T_{SB}(2,1) \sin \alpha \cos \beta}{-T_{SB}(3,1) \cos \alpha \cos \beta} \right) \quad (5.61)$$

Differentiating Eqs. (5.60) and (5.61) yield

$$\frac{\partial \phi}{\partial \dot{\mathbf{X}}_c} = \frac{\sin \hat{\phi} \sin \hat{\theta}}{\cos \hat{\phi} \cos \hat{\theta}} \frac{\partial \theta}{\partial \dot{\mathbf{X}}_c} - \frac{\mathbf{T}_{SB}(2,2) \cos \hat{\alpha} \cos \hat{\beta} + \mathbf{T}_{SB}(3,2) \sin \hat{\alpha} \cos \hat{\beta}}{\cos \hat{\phi} \cos \hat{\theta}} \frac{\partial \alpha}{\partial \dot{\mathbf{X}}_c} + \frac{\begin{pmatrix} \mathbf{T}_{SB}(1,2) \cos \hat{\beta} + \mathbf{T}_{SB}(2,2) \sin \hat{\alpha} \sin \hat{\beta} \\ -\mathbf{T}_{SB}(3,2) \cos \hat{\alpha} \sin \hat{\beta} \end{pmatrix}}{\cos \hat{\phi} \cos \hat{\theta}} \frac{\partial \beta}{\partial \dot{\mathbf{X}}_c} \quad (5.62)$$

$$\frac{\partial \theta}{\partial \dot{\mathbf{X}}_c} = \frac{\mathbf{T}_{SB}(2,1) \cos \hat{\alpha} \cos \hat{\beta} + \mathbf{T}_{SB}(3,1) \sin \hat{\alpha} \cos \hat{\beta}}{\cos \hat{\theta}} \frac{\partial \alpha}{\partial \dot{\mathbf{X}}_c} - \frac{\begin{pmatrix} \mathbf{T}_{SB}(1,1) \cos \hat{\beta} + \mathbf{T}_{SB}(2,1) \sin \hat{\alpha} \sin \hat{\beta} \\ -\mathbf{T}_{SB}(3,1) \cos \hat{\alpha} \sin \hat{\beta} \end{pmatrix}}{\cos \hat{\theta}} \frac{\partial \beta}{\partial \dot{\mathbf{X}}_c}. \quad (5.63)$$

Further, differentiating Eqs. (5.58) and (5.59) yield

$$\frac{\partial \alpha}{\partial \dot{\mathbf{X}}_c} = \frac{\dot{\mathbf{R}}^T \dot{\mathbf{j}}_s}{(\dot{\mathbf{R}}^T \dot{\mathbf{j}}_s)^2 + (\dot{\mathbf{R}}^T \dot{\mathbf{k}}_s)^2} \left( \dot{\mathbf{R}}^T \frac{\partial \dot{\mathbf{k}}_s}{\partial \dot{\mathbf{X}}_c} + \dot{\mathbf{k}}_s^T \frac{\partial \mathbf{R}}{\partial \dot{\mathbf{X}}_c} \right) - \frac{\dot{\mathbf{R}}^T \dot{\mathbf{k}}_s}{(\dot{\mathbf{R}}^T \dot{\mathbf{j}}_s)^2 + (\dot{\mathbf{R}}^T \dot{\mathbf{k}}_s)^2} \left( \dot{\mathbf{R}}^T \frac{\partial \dot{\mathbf{j}}_s}{\partial \dot{\mathbf{X}}_c} + \dot{\mathbf{j}}_s^T \frac{\partial \mathbf{R}}{\partial \dot{\mathbf{X}}_c} \right) \quad (5.64)$$

$$\frac{\partial \beta}{\partial \dot{\mathbf{X}}_c} = -\frac{\sqrt{(\dot{\mathbf{R}}^T \dot{\mathbf{j}}_s)^2 + (\dot{\mathbf{R}}^T \dot{\mathbf{k}}_s)^2}}{\|\dot{\mathbf{R}}\|^2} \left( \dot{\mathbf{R}}^T \frac{\partial \dot{\mathbf{i}}_s}{\partial \dot{\mathbf{X}}_c} + \dot{\mathbf{i}}_s^T \frac{\partial \mathbf{R}}{\partial \dot{\mathbf{X}}_c} \right) + \frac{(\dot{\mathbf{R}}^T \dot{\mathbf{i}}_s)(\dot{\mathbf{R}}^T \dot{\mathbf{k}}_s)}{\|\dot{\mathbf{R}}\|^2 \sqrt{(\dot{\mathbf{R}}^T \dot{\mathbf{j}}_s)^2 + (\dot{\mathbf{R}}^T \dot{\mathbf{k}}_s)^2}} \left( \dot{\mathbf{R}}^T \frac{\partial \dot{\mathbf{k}}_s}{\partial \dot{\mathbf{X}}_c} + \dot{\mathbf{k}}_s^T \frac{\partial \mathbf{R}}{\partial \dot{\mathbf{X}}_c} \right) + \frac{(\dot{\mathbf{R}}^T \dot{\mathbf{i}}_s)(\dot{\mathbf{R}}^T \dot{\mathbf{j}}_s)}{\|\dot{\mathbf{R}}\|^2 \sqrt{(\dot{\mathbf{R}}^T \dot{\mathbf{j}}_s)^2 + (\dot{\mathbf{R}}^T \dot{\mathbf{k}}_s)^2}} \left( \dot{\mathbf{R}}^T \frac{\partial \dot{\mathbf{j}}_s}{\partial \dot{\mathbf{X}}_c} + \dot{\mathbf{j}}_s^T \frac{\partial \mathbf{R}}{\partial \dot{\mathbf{X}}_c} \right). \quad (5.65)$$

Note that the  $\dot{\mathbf{i}}_s$ ,  $\dot{\mathbf{j}}_s$ , and  $\dot{\mathbf{k}}_s$  unit vectors are the columns of the sensor to inertial coordinate system transformation matrix

$$\begin{bmatrix} \dot{\mathbf{i}}_s & \dot{\mathbf{j}}_s & \dot{\mathbf{k}}_s \end{bmatrix} \triangleq (\mathbf{T}_{SB} \mathbf{T}_{BL} \mathbf{T}_{LI})^T. \quad (5.66)$$

Define three vectors

$$\begin{bmatrix} \mathbf{C}_2 & \mathbf{C}_3 & \mathbf{C}_4 \end{bmatrix} \triangleq (\mathbf{T}_{SB} \mathbf{T}_{BL})^T. \quad (5.67)$$



which are not a function of  $\mathbf{X}_c$ . Then,

$$\dot{\mathbf{i}}_S = \mathbf{T}_{LI}^T \mathbf{C}_2 \quad (5.68)$$

$$\dot{\mathbf{j}}_S = \mathbf{T}_{LI}^T \mathbf{C}_3 \quad (5.69)$$

$$\dot{\mathbf{k}}_S = \mathbf{T}_{LI}^T \mathbf{C}_4. \quad (5.70)$$

Differentiating Eqs. (5.68-5.70) produces

$$\frac{\partial \dot{\mathbf{i}}_S}{\partial \dot{\mathbf{X}}_c} = \mathbf{C}_2(1) \frac{\partial \mathbf{T}_{IL1}}{\partial \dot{\mathbf{X}}_c} + \mathbf{C}_2(2) \frac{\partial \mathbf{T}_{IL2}}{\partial \dot{\mathbf{X}}_c} + \mathbf{C}_2(3) \frac{\partial \mathbf{T}_{IL3}}{\partial \dot{\mathbf{X}}_c} \quad (5.71)$$

$$\frac{\partial \dot{\mathbf{j}}_S}{\partial \dot{\mathbf{X}}_c} = \mathbf{C}_3(1) \frac{\partial \mathbf{T}_{IL1}}{\partial \dot{\mathbf{X}}_c} + \mathbf{C}_3(2) \frac{\partial \mathbf{T}_{IL2}}{\partial \dot{\mathbf{X}}_c} + \mathbf{C}_3(3) \frac{\partial \mathbf{T}_{IL3}}{\partial \dot{\mathbf{X}}_c} \quad (5.72)$$

$$\frac{\partial \dot{\mathbf{k}}_S}{\partial \dot{\mathbf{X}}_c} = \mathbf{C}_4(1) \frac{\partial \mathbf{T}_{IL1}}{\partial \dot{\mathbf{X}}_c} + \mathbf{C}_4(2) \frac{\partial \mathbf{T}_{IL2}}{\partial \dot{\mathbf{X}}_c} + \mathbf{C}_4(3) \frac{\partial \mathbf{T}_{IL3}}{\partial \dot{\mathbf{X}}_c}. \quad (5.73)$$

Lastly, Eq. (5.52) can be rewritten

$$\mathbf{T}_{IL1} = \text{unit} \left( (\mathbf{r}_c^T \mathbf{r}_c) \mathbf{v}_c - (\mathbf{r}_c^T \mathbf{v}_c) \mathbf{r}_c \right) \quad (5.74)$$

$$\triangleq \text{unit}(\mathbf{C}_5) \quad (5.75)$$

which can be differentiated to yield

$$\frac{\partial \mathbf{T}_{IL1}}{\partial \dot{\mathbf{X}}_c} = \left( \frac{\mathbf{I}}{\|\dot{\mathbf{C}}_5\|} - \frac{\dot{\mathbf{C}}_5 \dot{\mathbf{C}}_5^T}{\|\dot{\mathbf{C}}_5\|^3} \right) \frac{\partial \mathbf{C}_5}{\partial \dot{\mathbf{X}}_c} \quad (5.76)$$

where

$$\frac{\partial \mathbf{C}_5}{\partial \dot{\mathbf{X}}_c} = \begin{bmatrix} 2\dot{\mathbf{v}}_c \dot{\mathbf{r}}_c^T - \dot{\mathbf{r}}_c^T \dot{\mathbf{v}}_c \mathbf{I} - \dot{\mathbf{r}}_c \dot{\mathbf{v}}_c^T & \vdots & \dot{\mathbf{r}}_c^T \dot{\mathbf{r}}_c \mathbf{I} - \dot{\mathbf{r}}_c \dot{\mathbf{r}}_c^T \end{bmatrix}. \quad (5.77)$$

Further, differentiating Eqs. (5.53) and (5.54) yield

$$\begin{aligned} \frac{\partial \mathbf{T}_{IL2}}{\partial \dot{\mathbf{X}}_c} &= \left( \frac{(\dot{\mathbf{r}}_c \times \dot{\mathbf{v}}_c)(\dot{\mathbf{r}}_c \times \dot{\mathbf{v}}_c)^T}{\|\dot{\mathbf{r}}_c \times \dot{\mathbf{v}}_c\|^3} - \frac{\mathbf{I}}{\|\dot{\mathbf{r}}_c \times \dot{\mathbf{v}}_c\|} \right) \\ &\times \begin{bmatrix} 0 & \dot{z}_c & -\dot{y}_c & 0 & -\dot{z}_c & \dot{y}_c \\ -\dot{z}_c & 0 & \dot{x}_c & \dot{z}_c & 0 & -\dot{x}_c \\ \dot{y}_c & -\dot{x}_c & 0 & -\dot{y}_c & \dot{x}_c & 0 \end{bmatrix} \end{aligned} \quad (5.78)$$

$$\frac{\partial \mathbf{T}_{IL3}}{\partial \dot{\mathbf{X}}_c} = \begin{bmatrix} \dot{\mathbf{r}}_c \dot{\mathbf{r}}_c^T - \frac{\mathbf{I}}{\|\dot{\mathbf{r}}_c\|} & \vdots & \mathbf{0} \end{bmatrix}. \quad (5.79)$$

Tables 5.1 and 5.2 summarize the measurement - state relationships.

Table 5.1: Measurement - State Relationships

Parameter		Derivative	
$h_{1k}$	Eq. (5.40)	$\frac{\partial h_{1k}}{\partial \mathbf{X}_c}$	Eq. (5.42)
$R$	Eq. (5.47)	$\frac{\partial R}{\partial \mathbf{X}_c}$	Eq. (5.49)
$\dot{R}$	Eq. (5.48)	$\frac{\partial \dot{R}}{\partial \mathbf{X}_c}$	Eq. (5.50)
$\phi$	Eq. (5.60)	$\frac{\partial \phi}{\partial \mathbf{X}_c}$	Eq. (5.62)
$\theta$	Eq. (5.61)	$\frac{\partial \theta}{\partial \mathbf{X}_c}$	Eq. (5.63)

## 5.2 Simulation Results

A nonlinear simulation was developed to model the rendezvous navigation filter (see Chapter 7). Several profiles were executed in order to assess the performance of the rendezvous navigation filter. For each profile, clockwise orbits were used. A planar circular orbit was also used to insure final position errors due to the rendezvous targeting law were less than one meter. The incline angle, initial condition angle and transfer time were fixed at the baseline values which resulted in an "in-plane" rendezvous profile.

The chaser vehicle was initialized 19 km behind the target vehicle in a coelliptic orbit. An error vector was then added to the chaser vehicle to model the uncertainty in the state just prior to the  $T/I$  maneuver. Error vectors were generated randomly using error statistics consistent with Gingiss [35]. Thirteen particular error vectors were used in this research; each one corresponded to a constant  $1\sigma$  error from the 6-dimensional error ellipsoid at the  $T/I$  maneuver. Potter [42] and Hitzl [43] both describe the technique used in choosing these vectors. This technique consists of computing a scalar using the error vector and the inverse of the covariance matrix. This scalar is proportional

Table 5.2: Parameters used by Measurement - State Relationships

Parameter		Derivative	
$R$	Eq. (5.45)	$\frac{\partial R}{\partial \bar{X}_c}$	Eq. (5.56)
$V$	Eq. (5.46)	$\frac{\partial V}{\partial \bar{X}_c}$	Eq. (5.57)
$\alpha$	Eq. (5.58)	$\frac{\partial \alpha}{\partial \bar{X}_c}$	Eq. (5.64)
$\beta$	Eq. (5.59)	$\frac{\partial \beta}{\partial \bar{X}_c}$	Eq. (5.65)
$i_s$	Eq. (5.68)	$\frac{\partial i_s}{\partial \bar{X}_c}$	Eq. (5.71)
$j_s$	Eq. (5.69)	$\frac{\partial j_s}{\partial \bar{X}_c}$	Eq. (5.72)
$k_s$	Eq. (5.70)	$\frac{\partial k_s}{\partial \bar{X}_c}$	Eq. (5.73)
$C_1$	Eq. (5.55)	N/A	N/A
$C_2$	Eq. (5.67)	N/A	N/A
$C_3$	Eq. (5.67)	N/A	N/A
$C_4$	Eq. (5.67)	N/A	N/A
$C_5$	Eq. (5.75)	$\frac{\partial C_5}{\partial \bar{X}_c}$	Eq. (5.77)
$T_{IL1}$	Eq. (5.52)	$\frac{\partial T_{IL1}}{\partial \bar{X}_c}$	Eq. (5.76)
$T_{IL2}$	Eq. (5.53)	$\frac{\partial T_{IL2}}{\partial \bar{X}_c}$	Eq. (5.78)
$T_{IL3}$	Eq. (5.54)	$\frac{\partial T_{IL3}}{\partial \bar{X}_c}$	Eq. (5.79)

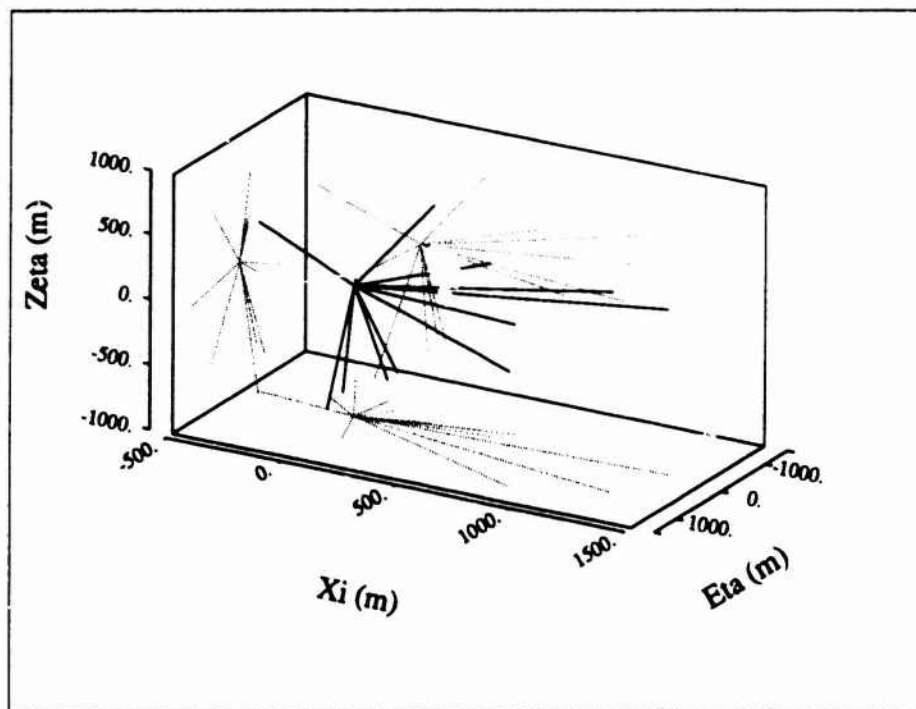


Figure 5.3: Position Error Vectors for Monte Carlo Analysis

to the  $n$ -dimensional probability density function and hence, constant values of this scalar equate to constant surfaces on the error ellipsoid. Finally, these vectors were chosen to span all directions of the  $T/I$  error ellipsoid. Figures 5.3 and 5.4 show the direction of these position and velocity error vectors, respectively.

The proximity sensor was modeled after the Space Shuttle rendezvous radar [44]. Sensor measurements consisted of relative range and line-of-sight angles and were taken every minute. Measurement statistics and sensor capabilities were chosen similar to the Space Shuttle rendezvous radar [44] and were

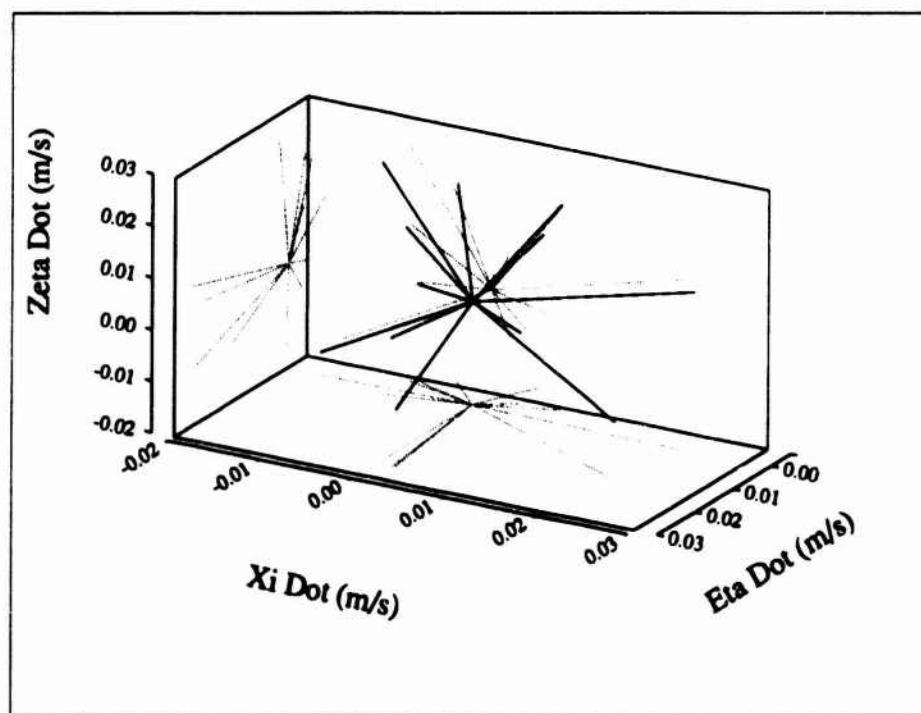


Figure 5.4: Velocity Error Vectors for Monte Carlo Analysis

consistent with an advanced rendezvous tracking system study [45]. Random noise was added to each measurement, but measurement biases and unmodeled accelerations were omitted from the estimation vector.

Figure 5.5 shows the average state estimation error of all 13 error vectors (solid line) in the LVIR coordinate frame; also shown is the  $1\sigma$  standard deviation of the state (dotted lines). Appendix C.1 contains these same data for each individual simulation. State estimation errors converged quickly after only a few measurements were incorporated.

In Chapter 4, midcourse correction maneuvers were shown to substantially reduce final position errors due to the rendezvous targeting law; they also aid in reducing the effects of navigation errors. The optimal placement of a midcourse correction maneuver within the rendezvous profile depends on the navigation errors at the time of the maneuver and the sensitivity of the final position errors at the time of rendezvous with respect to maneuver velocity errors. Two parametric studies were completed to characterize the optimal placement of a midcourse correction maneuver.

### 5.2.1 Navigation Errors Parametric Study

The first study investigated was the navigation errors along the reference trajectory for the baseline "in-plane" rendezvous profile. This study was designed to answer the question, "Is there a place in the rendezvous profile where the navigation errors are small in the direction of the  $\Delta V$  required from a midcourse correction maneuver?" If such a place exists, a midcourse correction maneuver should be executed at this point in the rendezvous profile because the midcourse correction maneuver is insensitive to navigation errors.

To determine if such a position in the rendezvous profile exists, a

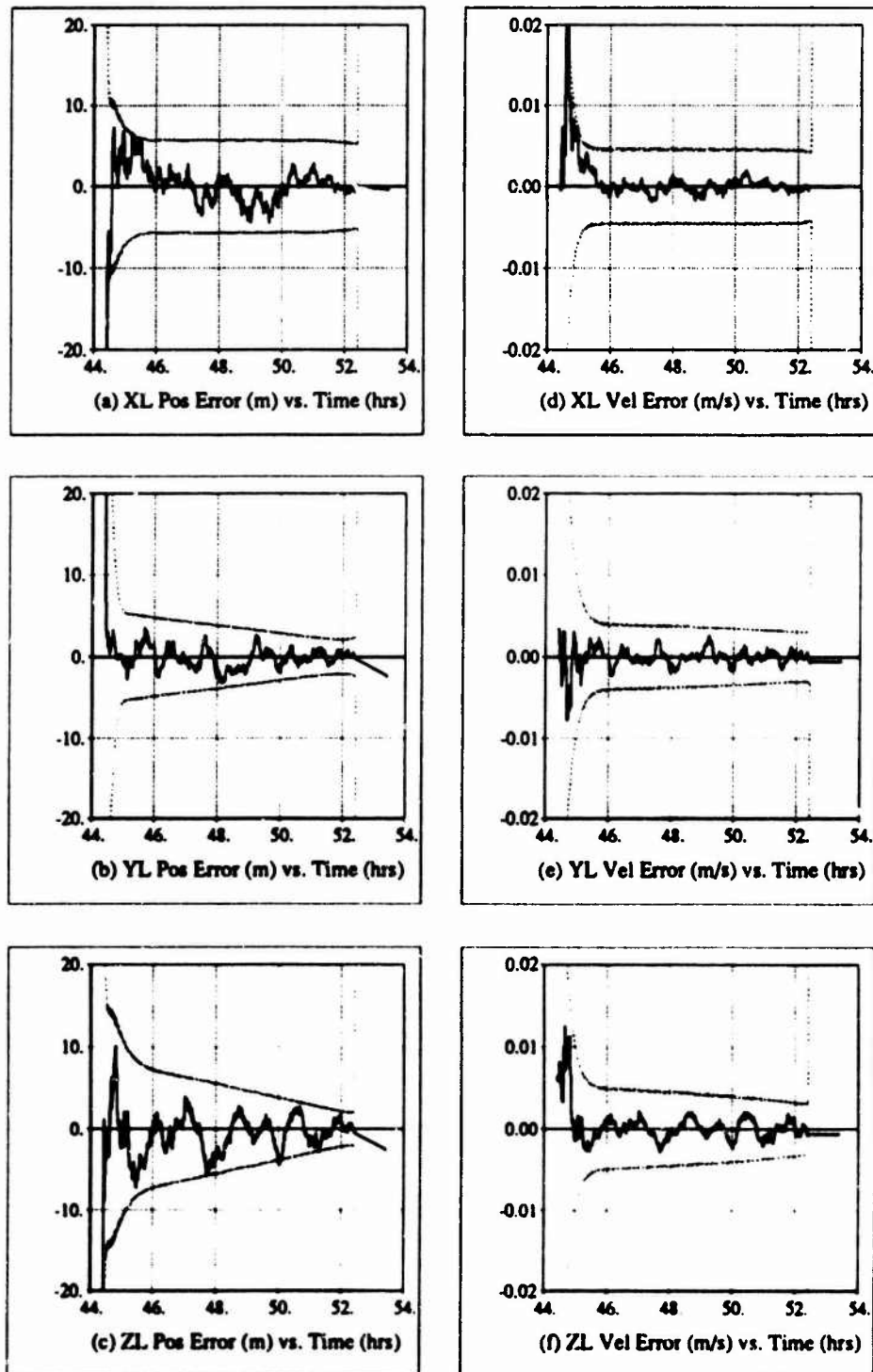


Figure 5.5: Average Chaser Vehicle State Estimation Error

covariance analysis was done. Figure 5.6 (a) shows the time history of the magnitude of the principle axes of the LVIR covariance position error ellipsoid. Also indicated on Fig. 5.6 (a) is the general correlation between the LVIR coordinate frame and the principle axes. Figure 5.6 (b) gives the LVIR azimuth and elevation angles of the largest principle axis of the covariance position error ellipsoid. Figure 5.7 provides these same data for the LVIR covariance velocity error ellipsoid.

The covariance position error ellipsoid is initialized as a sphere. With the first couple of proximity sensor measurements, the sphere shrinks at an essentially uniform rate. Then, for a brief time the out-of-plane direction is the largest principle axis, but then it decreases and the radial direction becomes the largest principle axis. It then shrinks and, finally, the downtrack direction becomes the largest principle axis. The final covariance position error ellipsoid is aligned with the LVIR coordinate frame, but rotated 4.9 deg about the positive out-of-plane axis.

The covariance velocity error ellipsoid behaves in an similar manner except for the out-of-plane direction never being the largest principle axis. The final covariance velocity error ellipsoid is also aligned with the LVIR coordinate frame, but it is rotated 5.0 deg about the positive out-of-plane axis.

Note that even though these error ellipsoids lose their spherical shape, which might suggest a desirable location for a midcourse correction maneuver, the absolute magnitude of all of the principle axes is small after only a few measurements have been incorporated into the rendezvous navigation filter. Thus, placement of a midcourse correction maneuver is not directly dependent on navigation errors.



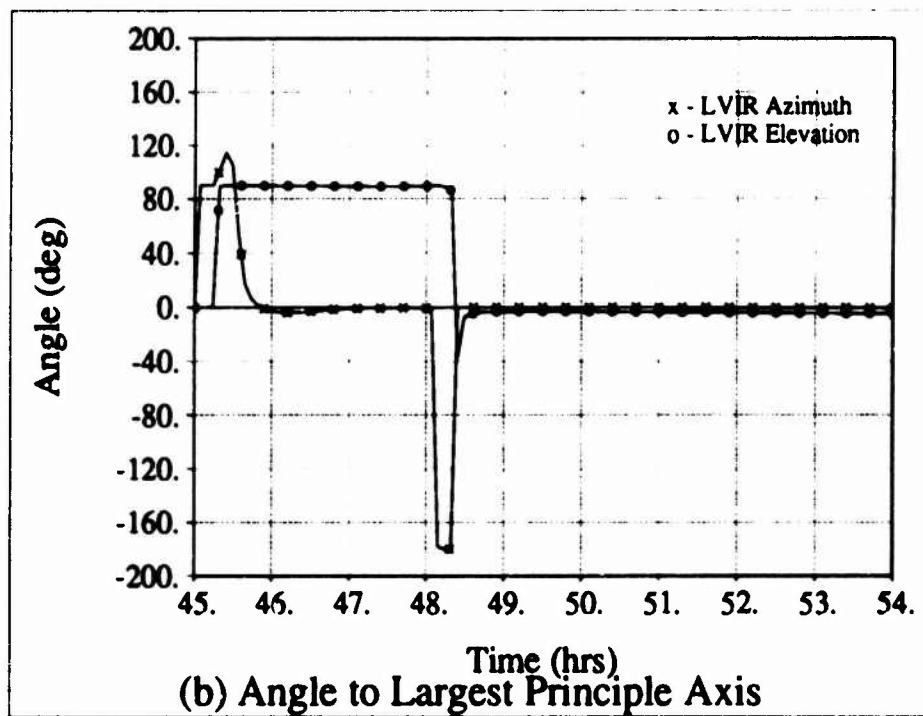
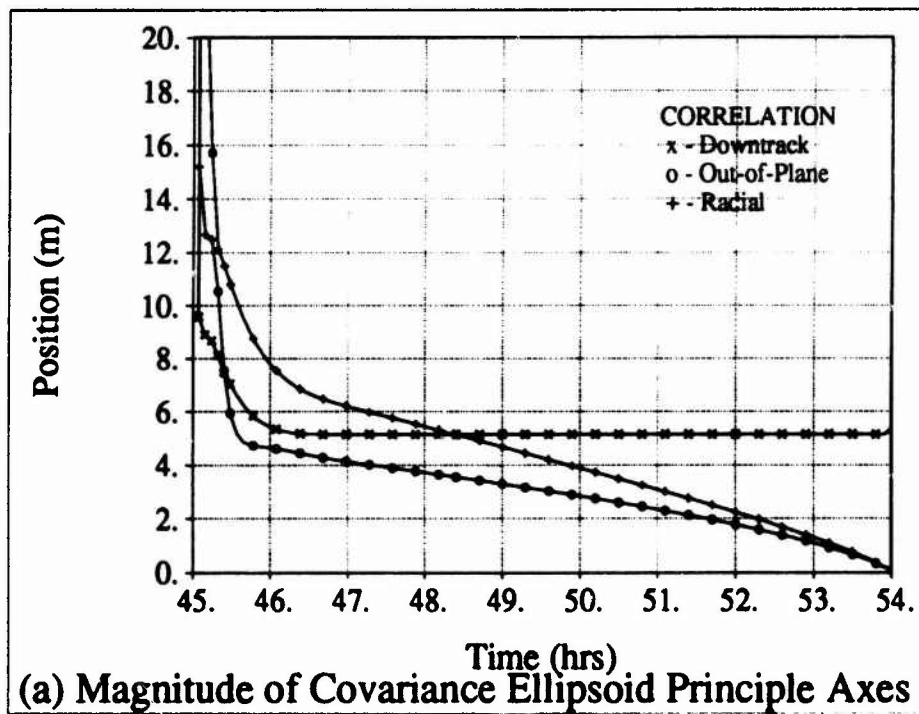


Figure 5.6: Covariance Position Error Ellipsoid Magnitude and Orientation

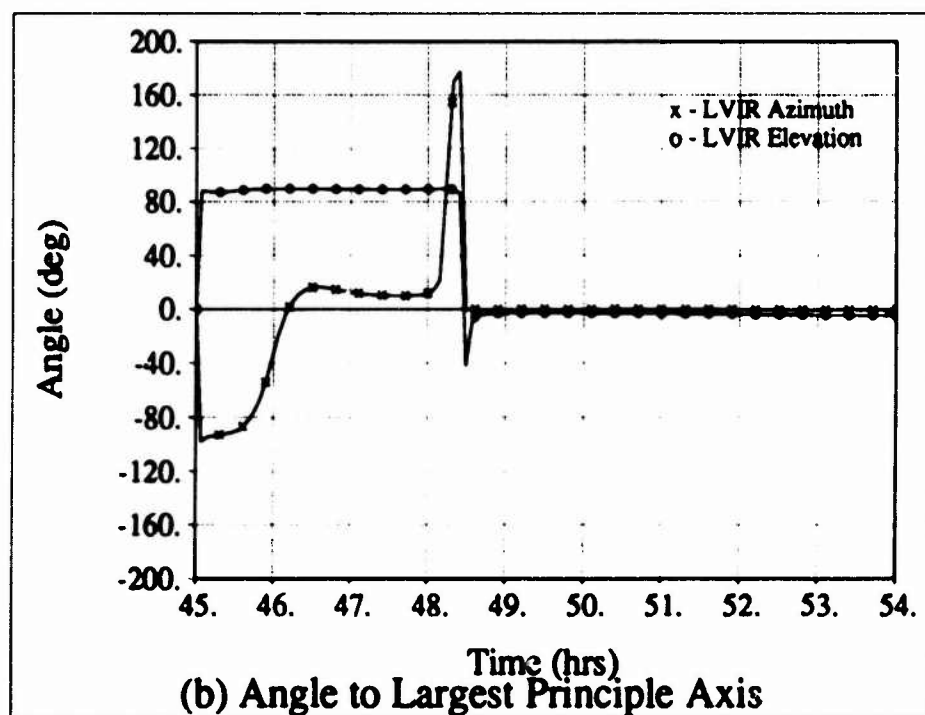
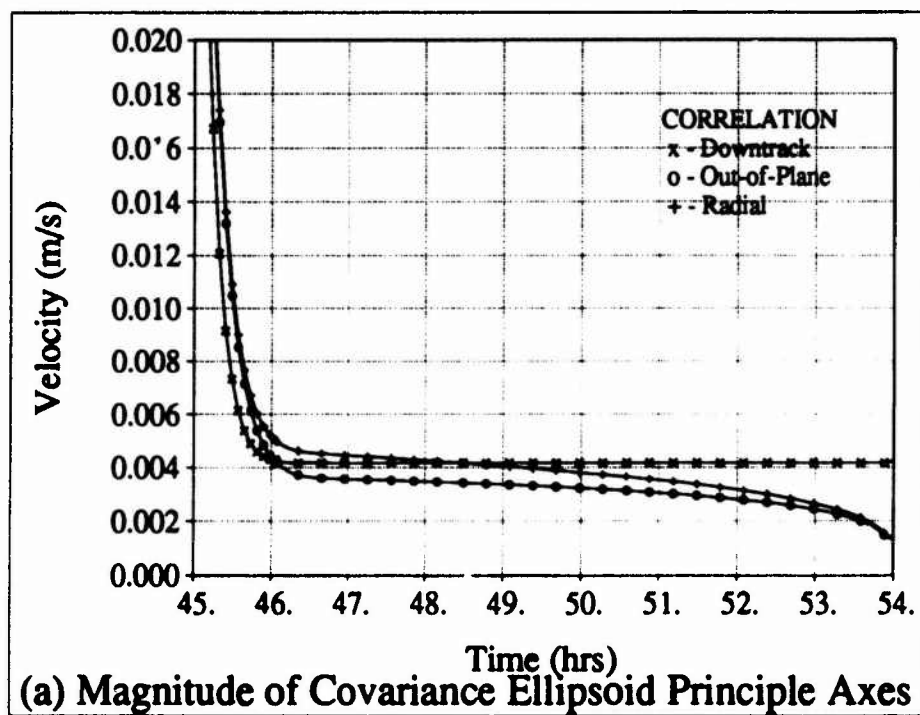


Figure 5.7: Covariance Velocity Error Ellipsoid Magnitude and Orientation

### 5.2.2 Final Position Error Sensitivity Parametric Study

The second study investigated was the sensitivity of the final position errors with respect to maneuver velocity errors. This study was designed to answer the question, "Is there a place in the rendezvous profile where final position errors are insensitive to velocity errors from executing a midcourse correction maneuver?" If such a place exists, a midcourse correction maneuver should be executed at this point in the rendezvous profile because any velocity errors in the maneuver execution will have less affect on final position errors.

To determine if such a position in the rendezvous profile exists, a sensitivity matrix was computed; the sensitivity matrix is defined as

$$\frac{\partial \delta_{pTF}}{\partial V} \triangleq \begin{bmatrix} \frac{\partial \delta_d}{\partial V_d} & \frac{\partial \delta_d}{\partial V_o} & \frac{\partial \delta_d}{\partial V_r} \\ \frac{\partial \delta_o}{\partial V_d} & \frac{\partial \delta_o}{\partial V_o} & \frac{\partial \delta_o}{\partial V_r} \\ \frac{\partial \delta_r}{\partial V_d} & \frac{\partial \delta_r}{\partial V_o} & \frac{\partial \delta_r}{\partial V_r} \end{bmatrix} \quad (5.80)$$

where the ( )<sub>d</sub>, ( )<sub>o</sub> and ( )<sub>r</sub> subscripts indicate the downtrack, out-of-plane and radial directions, respectively. Each partial derivative in Eq. (5.80) was computed numerically along the reference trajectory for the baseline "in-plane" rendezvous profile using the central differences technique with four evaluations.

Figure 5.8 gives a time history of the largest singular value of the sensitivity matrix; individual time histories of the elements of the sensitivity matrix are included in Appendix C.2. Figure 5.8 shows no significant sensitivity of the final position errors with respect to velocity errors. However, it does substantiate the general philosophy that the final position errors will be smaller given a smaller transfer time between the midcourse correction maneuver and the time of rendezvous. Nevertheless, the placement of a mid-

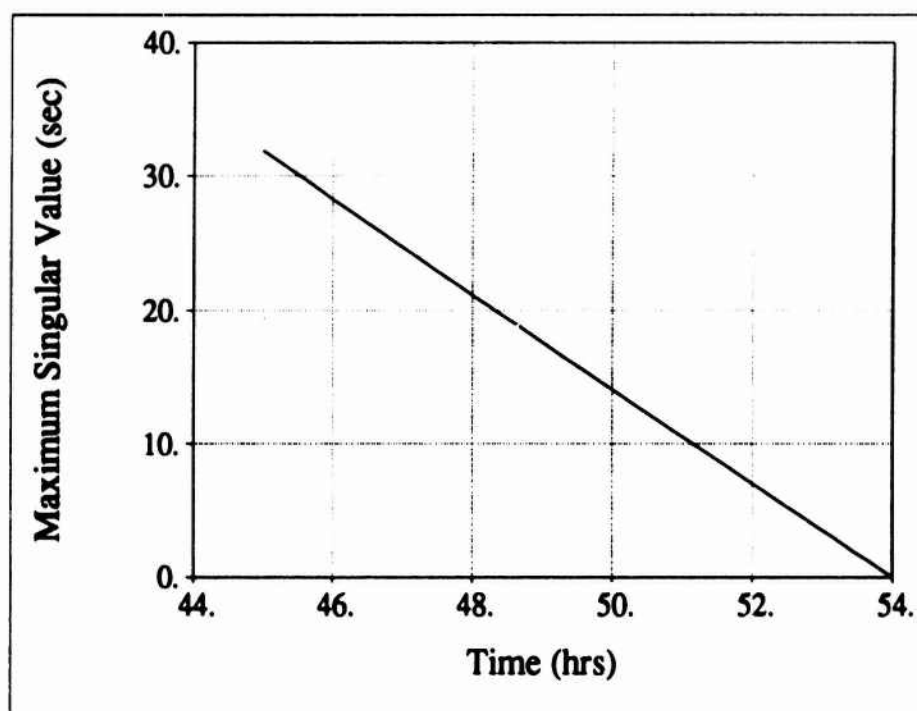


Figure 5.8: Sensitivity Matrix Largest Singular Value

course correction maneuver is not directly dependent on final position error sensitivities.

Thus, since the placement of a midcourse correction maneuver is not directly dependent on navigation errors or final position error sensitivities, the midcourse correction maneuvers can be placed in the rendezvous profile based on time.

## Chapter 6

### Applications

To demonstrate the entire guidance and navigation system, this chapter considers two profiles for terminal phase rendezvous in the planar circular orbit and two equivalent profiles in a  $\mathcal{H}_2$  guided halo orbit. The two profiles chosen correspond to "in-plane" (profile 1) and "out-of-plane" (profile 2) relative trajectories for the planar circular orbit; the initial condition angles were 46.08 deg and 180.00 deg, respectively. These same initial condition angles were used in the  $\mathcal{H}_2$  guided halo orbit demonstration. The transfer time was also held constant at 9 hrs for both demonstrations. The incline angle for the planar circular orbit demonstration was 22.85 deg; this is the same as the incline angle of the  $\mathcal{H}_2$  guided halo orbit used in this research.

Monte carlo simulations were done using the 13 error vectors selected in Chapter 5. For comparison purposes, a reference simulation was also done assuming "ideal" navigation. Four midcourse correction maneuvers were added to the rendezvous profile to correct for rendezvous targeting and rendezvous navigation filter state estimation errors. These maneuvers were placed on time at  $TI$  plus two,  $TI$  plus four,  $TI$  plus six and  $TI$  plus eight hours. The Space Shuttle program also uses four midcourse correction maneuvers in its rendezvous profile; three of these maneuvers are placed on time while one is executed on an elevation angle to the target vehicle.

This chapter presents a summary of these simulations; Appendix D tabulates the propulsion requirements and final miss distance for each indi-

vidual rendezvous profile. Propulsion requirements are given in terms of the velocity required for each maneuver. Final miss distance is defined as the error from the desired position offset at the time of rendezvous.

## 6.1 Planar Circular Orbit Demonstration

Figure 6.1 shows the reference relative trajectory for the "in-plane" profile; Fig. 6.2 applies to the "out-of-plane" profile. In both profiles, the chaser vehicle initiated the rendezvous profile 19 km behind the target vehicle in a coelliptic orbit. These relative trajectories have two main differences. In profile 1, the "in-plane" relative trajectory has a maximum out-of-plane position less than 20 m and goes only slightly below the target vehicle. This relative trajectory is essentially straight line motion and shows little orbital mechanics effects. By contrast, the maximum out-of-plane relative position in profile 2 is greater than 800 m and the "out-of-plane" relative trajectory goes below the target vehicle over 6 times the amount of the "in-plane" relative trajectory. Orbital mechanics effects are clearly present in this rendezvous profile.

These relative trajectory differences are also reflected in the propulsion requirements and final miss distance of each rendezvous profile. Table 6.1 summarizes the propulsion requirements for both the planar circular orbit and the  $\mathcal{H}_2$  guided halo orbit; the reaction control system (RCS) fuel consumed was computed using

$$w_p = w_o \left[ 1 - \exp \frac{\Delta V}{I_{sp} g} \right]. \quad (6.1)$$

The initial spacecraft weight was assumed to be the maximum allowed (13,000 lbs) under the assumptions of the restricted three-body problem. Also, a medium performance RCS jet ( $I_{sp} = 270$  sec) was assumed; this is a typi-

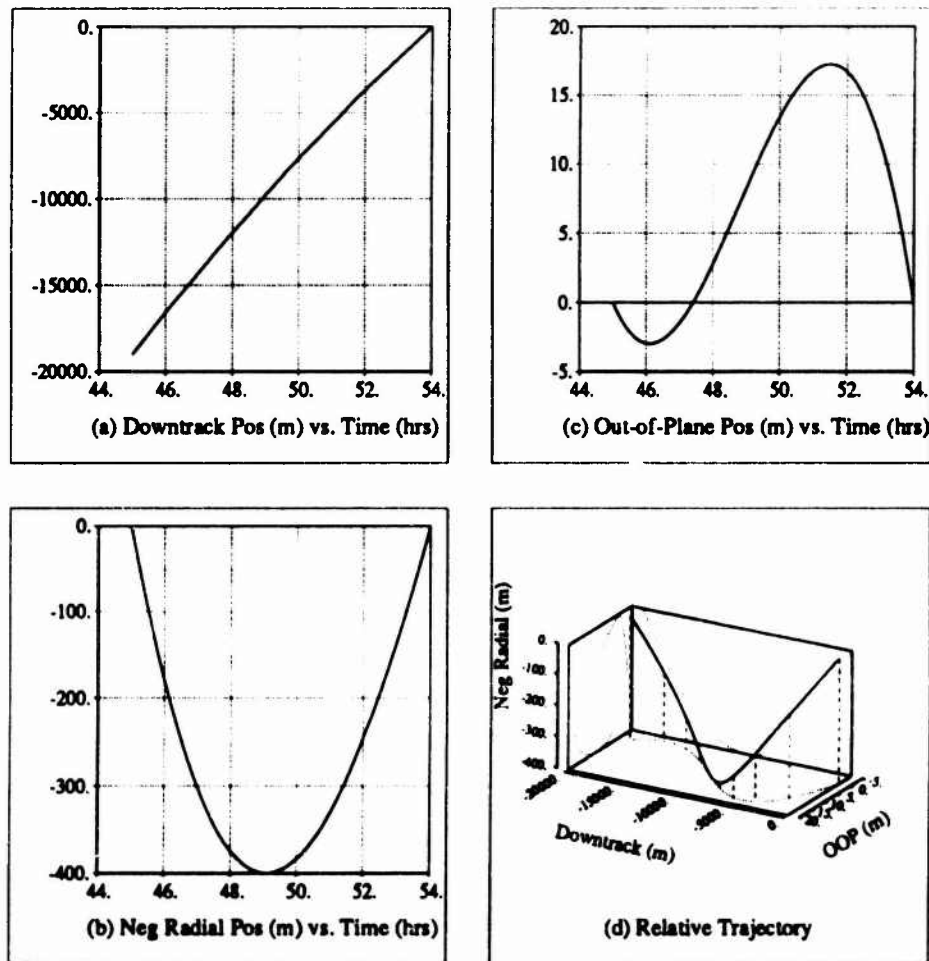


Figure 6.1: Planar Circular Orbit Reference Relative Trajectory  
(IC=46.08 deg, INC=22.85 deg, TT=9 hrs)



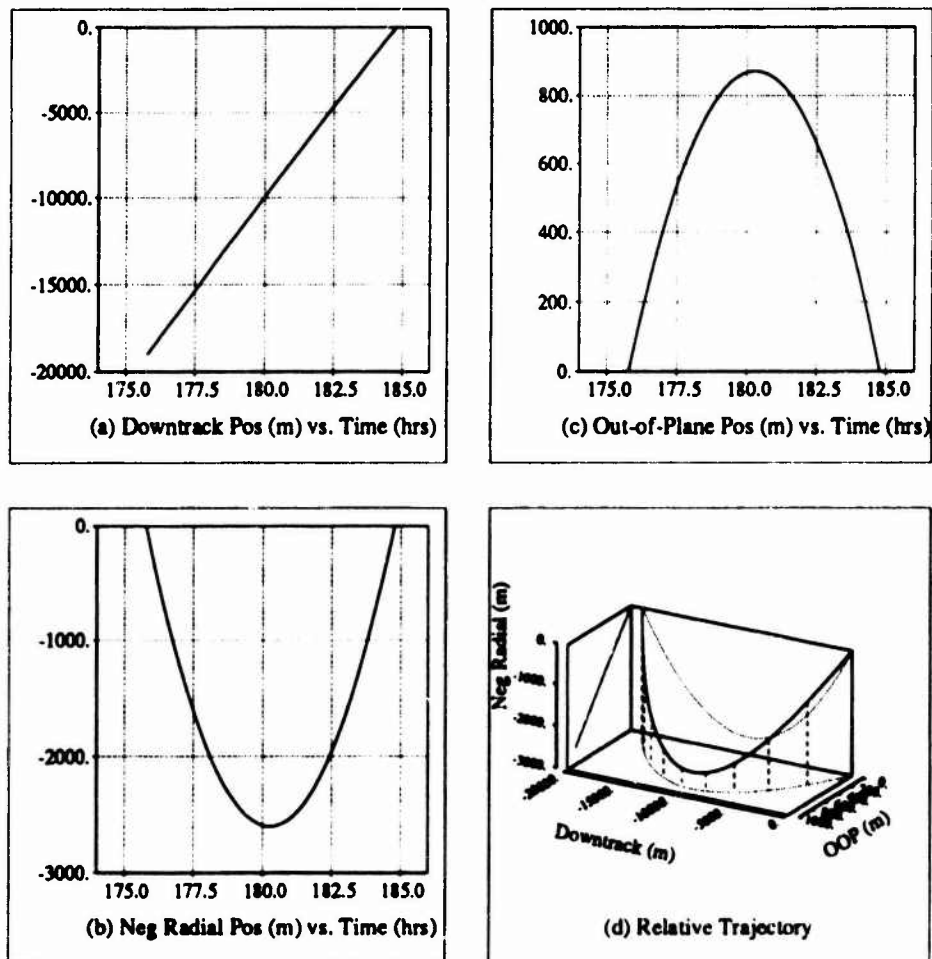


Figure 6.2: Planar Circular Orbit Reference Relative Trajectory  
(IC=180.00 deg, INC=22.85 deg, TT=9 hrs)

Table 6.1: Propulsion Requirements Summary

Error Vector	Rendezvous Maneuver (m/s)						RCS	
	<i>TI</i>	<i>MCC1</i>	<i>MCC2</i>	<i>MCC3</i>	<i>MCC4</i>	<i>TF</i>	Total	Fuel (lbs)
<b>Circle #1</b>								
Reference	0.686	0.000	0.000	0.000	0.000	0.491	1.177	5.776
Average	0.686	0.041	0.010	0.010	0.014	0.493	1.254	6.153
<b>Circle #2</b>								
Reference	0.680	0.000	0.000	0.000	0.000	0.643	1.322	6.487
Average	0.680	0.041	0.009	0.008	0.014	0.634	1.384	6.791
<b>Halo #1</b>								
Reference	0.627	0.019	0.022	0.027	0.044	0.684	1.421	6.972
Average	0.627	0.041	0.023	0.032	0.042	0.677	1.441	7.071
<b>Halo #2</b>								
Reference	0.704	0.008	0.008	0.009	0.013	0.672	1.413	6.933
Average	0.704	0.042	0.013	0.012	0.021	0.663	1.455	7.139

cal Space Shuttle RCS jet. Table 6.2 shows the final miss distance for both demonstrations. Velocity requirements increased 12.3% from the "in-plane" relative trajectory to the "out-of-plane" relative trajectory; final miss distance increased 21.3%.

State estimation errors from the rendezvous navigation filter were also small. Figures 6.3 and 6.4 show the average state estimation error of all 13 error vectors (solid line) and the associated  $1\sigma$  standard deviation of the state (dotted line). These data are given in the LVIR coordinate frame. The rendezvous navigation filter was not substantially affected by the geometry of the relative trajectory. These state estimation errors caused the velocity requirements to increase 6.5% and 4.7% for the "in-plane" and "out-of-plane" profiles, respectively. Final miss distance also increased to 12.7 m and 15.3 m for these profiles, respectively.

Even though these increases due to relative trajectory differences and rendezvous navigation filter state estimation errors are significant, it should be noted that the absolute propulsion requirements and final miss distance

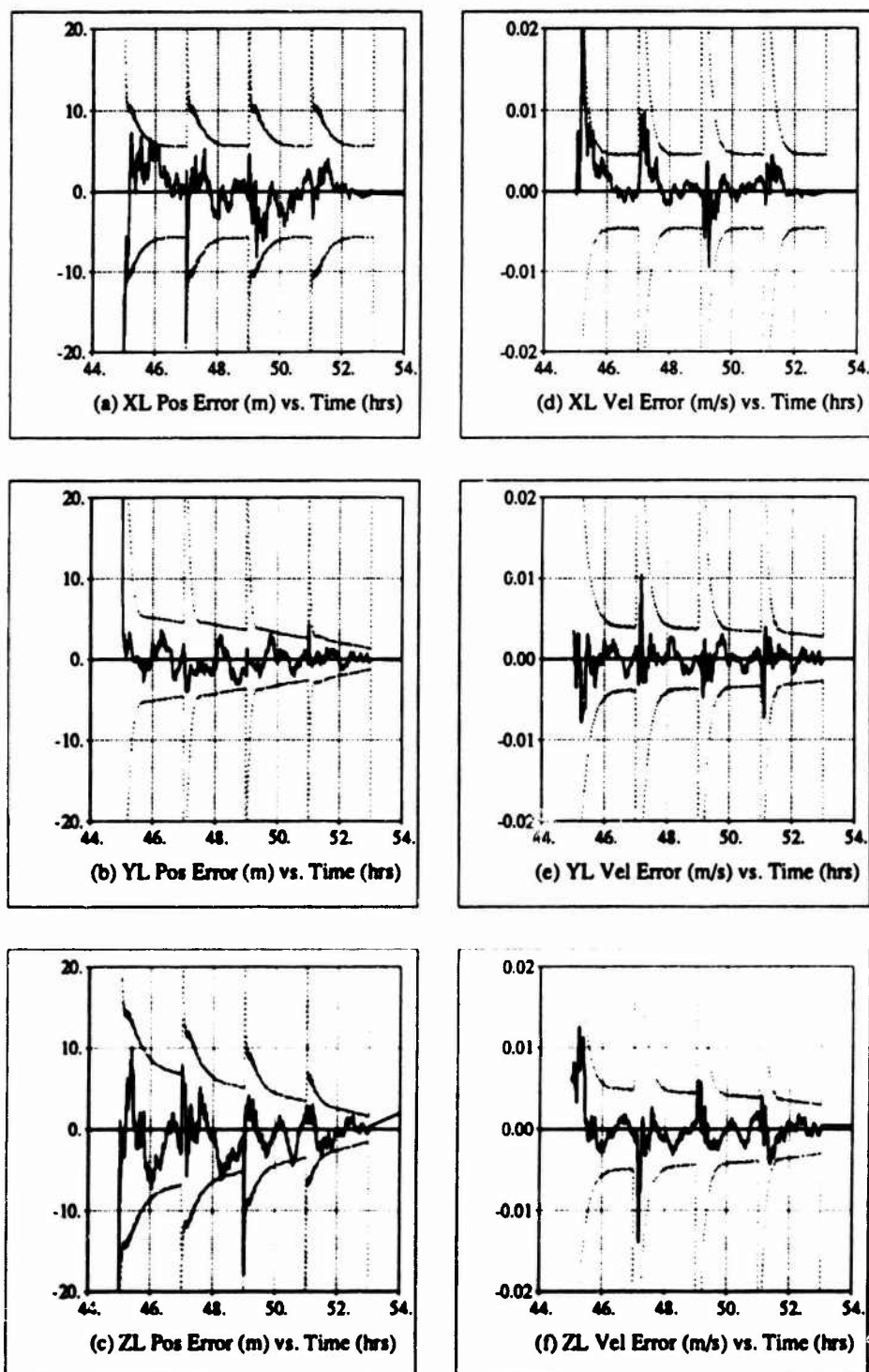


Figure 6.3: Planar Circular Orbit Average Chaser Vehicle State Estimation Error (IC=46.08 deg, INC=22.85 deg, TT=9 hrs)

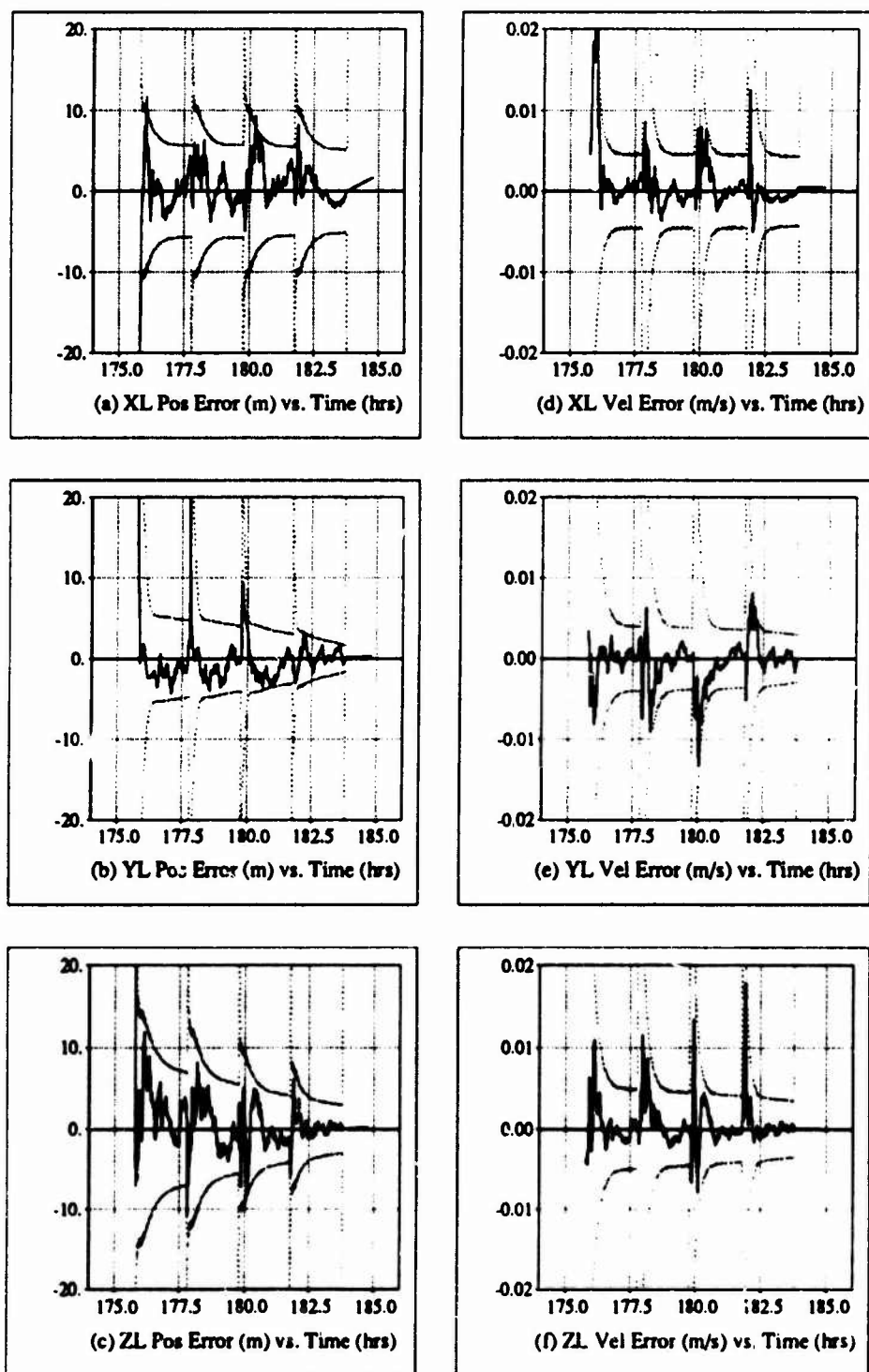


Figure 6.4: Planar Circular Orbit Average Chaser Vehicle State Estimation Error (IC=180.00 deg, INC=22.85 deg, TT=9 hrs)

Table 6.2: Final Miss Distance Summary

	Final Miss Distance (m)			
	Downtrack	Out-of-Plane	Radial	Total
<b>Circle #1</b>				
Reference	0.000	-0.001	0.000	0.001
Average Magnitude	4.919	7.204	6.983	12.666
<b>Circle #2</b>				
Reference	0.000	0.000	-0.001	0.001
Average Magnitude	8.086	9.779	5.686	15.362
<b>Halo #1</b>				
Reference	-7.673	19.394	0.124	20.857
Average Magnitude	9.160	19.585	9.303	25.924
<b>Halo #2</b>				
Reference	-4.834	-3.191	-0.885	5.859
Average Magnitude	5.898	10.222	5.036	14.109

were small in each profile.

## 6.2 $\mathcal{H}_2$ Guided Halo Orbit Demonstration

Figure 6.5 shows the reference relative trajectory for profile 1; Fig. 6.6 applies to profile 2. In both profiles, the chaser vehicle initiated the rendezvous profile approximately 19 km behind and slightly above the target vehicle. The trajectories clearly show the same characteristic as the planar circular orbit with respect to the radial component of the rendezvous profile. Not-so-obvious is why the maximum out-of-plane position did not follow the same trend. This exception is explained by noting that for the planar circular orbit, the  $\xi$ -axis velocity component of the chaser vehicle was zero prior to the  $T/I$  maneuver and after the  $T/I$  maneuver, the chaser vehicle moved in the negative  $\xi$  direction. However, for the  $\mathcal{H}_2$  guided halo orbit, the  $\xi$ -axis velocity component of the chaser vehicle was positive prior to the  $T/I$  maneuver. After the  $T/I$  maneuver, the chaser vehicle again moved in the

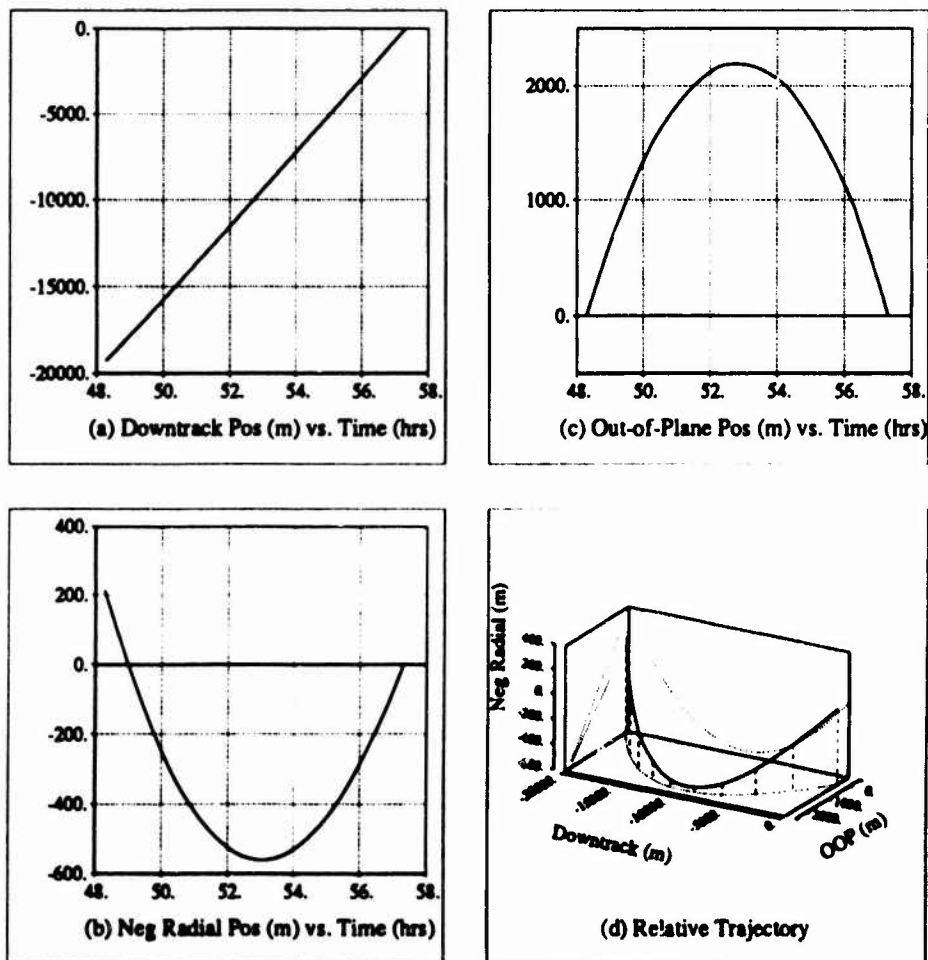


Figure 6.5:  $\mathcal{H}_2$  Guided Halo Orbit Reference Relative Trajectory  
(IC=46.08 deg, TT=9 hrs)

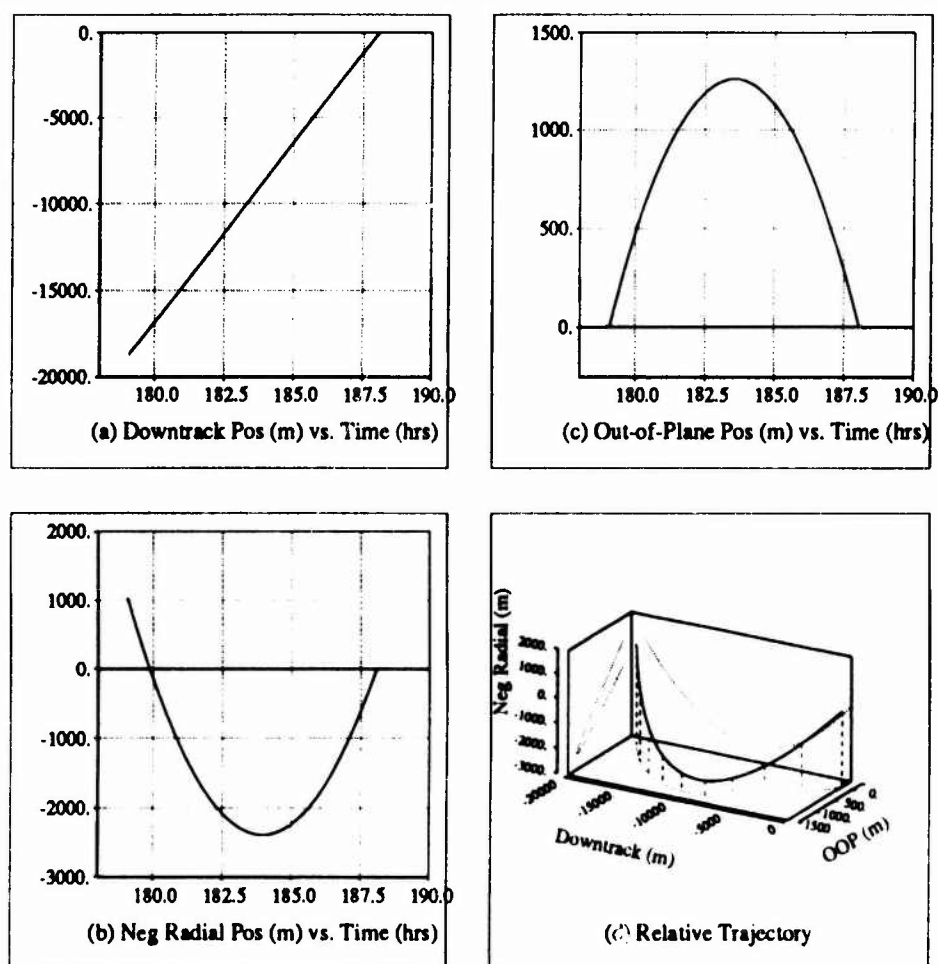


Figure 6.6:  $\mathcal{H}_2$  Guided Halo Orbit Reference Relative Trajectory  
(IC=180.00 deg, TT=9 hrs)

negative  $\xi$  direction. Hence, the pre-*TI*  $\xi$ -axis velocity opposed a portion of the post-*TI* motion and less total out-of-plane relative motion resulted. In both profiles, orbital mechanics effects are seen.

The effect of these relative trajectory differences was also present in the propulsion requirements and final miss distance. Essentially the same trends as for the planar circular orbit demonstration were seen. State estimation errors from the rendezvous navigation filter were also small just as in the planar circular orbit demonstration; Figs. 6.7 and 6.8 give the average state estimation error of all 13 error vectors (solid line) and the associated  $1\sigma$  standard deviation of the state (dotted line). These data are given in the LVIR coordinate frame. Again, the rendezvous navigation filter performance was not affected by the geometry of the relative trajectory. The state estimation errors caused the velocity requirements to increase 1.4% and 3.0% for profiles 1 and 2, respectively. Final miss distance also increased 24.3% and 140.8% for these profiles, respectively. When considering the absolute magnitude of the parameters, these increases are approximately the same as for the planar circular orbit demonstration.

As before, these increases are significant, but it should be emphasized that the absolute propulsion requirements and final miss distance remained small in both profiles.



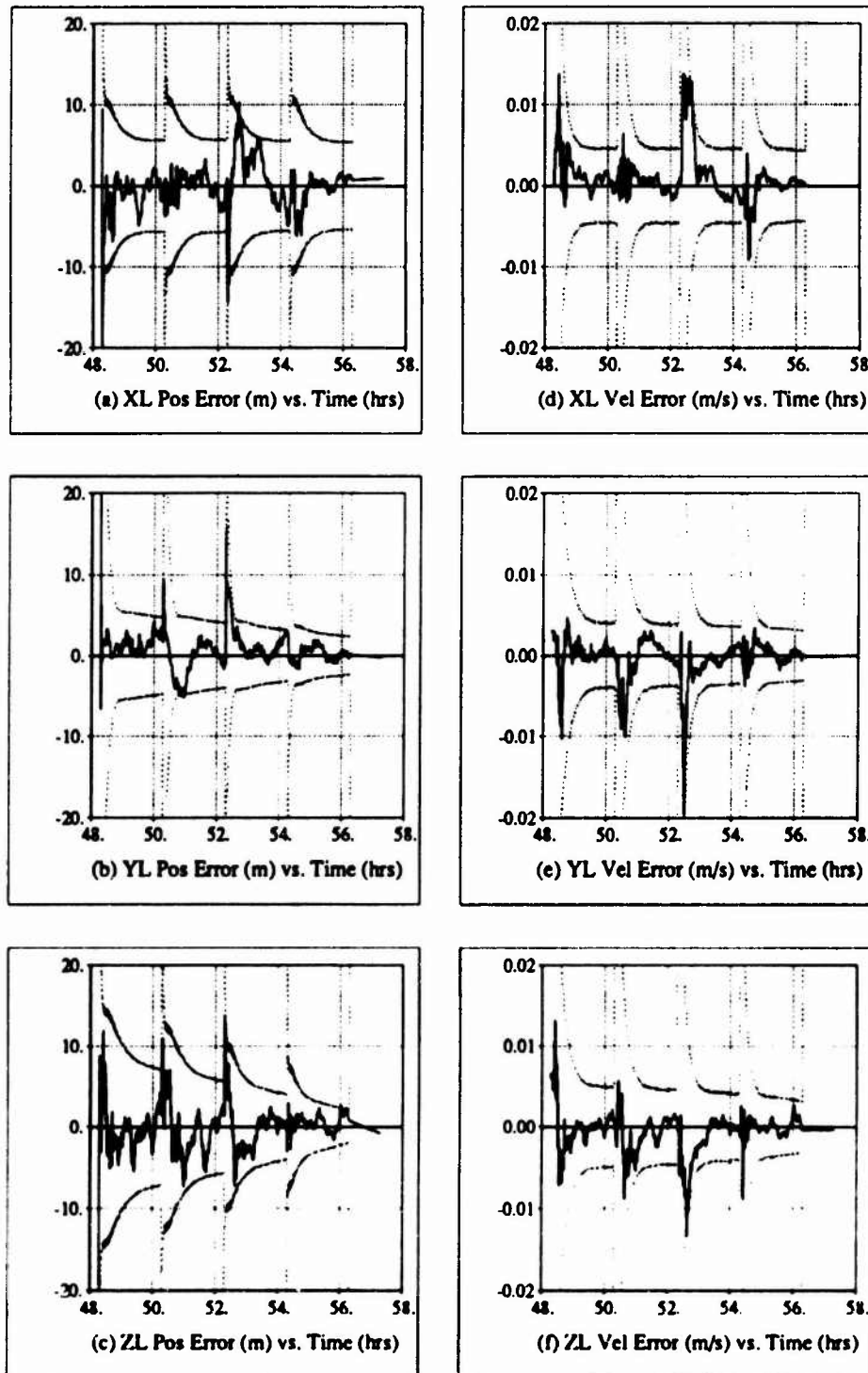


Figure 6.7:  $\mathcal{H}_2$  Guided Halo Orbit Average Chaser Vehicle State Estimation Error (IC=46.08 deg, TT=9 hrs)

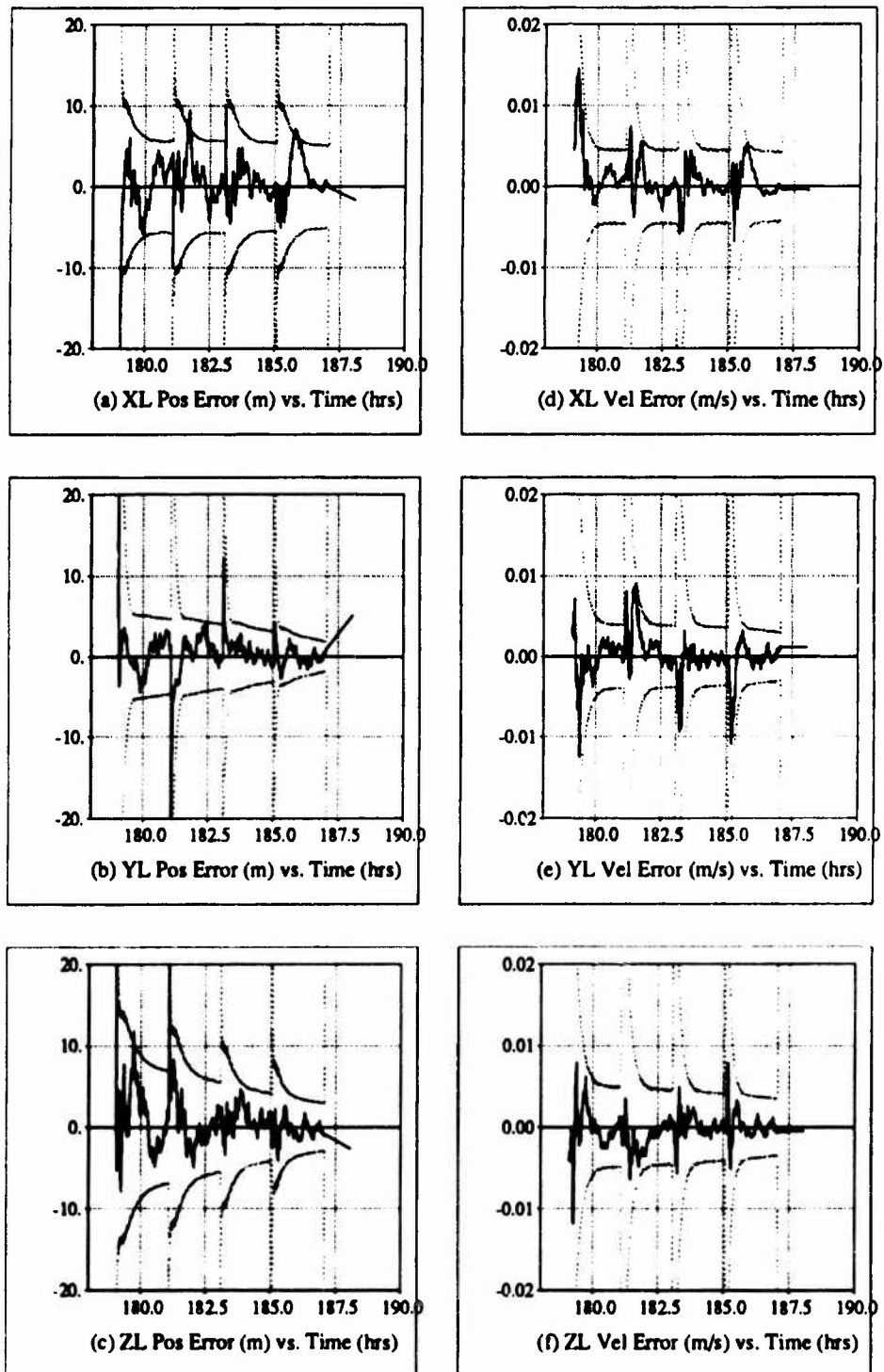


Figure 6.8:  $\mathcal{H}_2$  Guided Halo Orbit Average Chaser Vehicle State Estimation Error (IC=180.00 deg, TT=9 hrs)

## Chapter 7

### Nonlinear Simulation Package

This simulation package consists of three executable executive programs, associated subroutines, and numerous data plotting command files. The pre-processor program is an interactive parameter input program used to define approximately 500 selectable parameters required by the main simulation. The post-processor program edits stored data and computes variables of interest such as the statistics on the measurement residuals from the rendezvous navigation filter. All source code is written in FORTRAN; the data plotting command files use the XGRAMI application.

This chapter begins by describing the general capabilities of the simulation package. The functional modules of the main simulation are then discussed. Lastly, the pre-processor and post-processor programs are outlined.

#### 7.1 General Capabilities

The scenario being simulated is the terminal phase rendezvous between a chaser and target vehicle in the circular restricted three-body problem. The target and chaser vehicles are assumed, initially, to be in small radius halo orbits about the translunar equilibrium point in the Earth-Moon three-body system. Parameters identifying the specific three-body system are selectable. The type of translunar halo orbit is selectable between a planar circular orbit and a  $\mathcal{H}_2$  guided halo orbit. If a  $\mathcal{H}_2$  guided halo orbit is selected, the target and chaser vehicles can be placed in independent orbits. If a planar circular

orbit is selected, the chaser vehicle is initialized at a selectable offset position from the target vehicle in a coelliptic orbit.

The main simulation computes *TI* and *TF* maneuvers plus up to eight midcourse correction (*MCC1* – *MCC8*) maneuvers. All maneuvers are modeled impulsively. The *TI* maneuver may occur any time after the initial state vector time for the chaser vehicle. Up to five distinct sensor passes may occur prior to each maneuver except *TI*. Times for all maneuvers plus sensor pass start and stop times are selectable. The initial vector state vector time for the chaser and target vehicles and the *TI* time-of-ignition (*TIG*) are in absolute time; all other times are relative to *TI TIG*.

Five coordinate frames are used in the simulation; all computations are done in the inertial coordinate frame.

1. Inertial coordinate frame: Centered at the translunar equilibrium point with the  $\xi$ -axis pointing along a line from the Earth to the Moon, the  $\eta$ -axis in the Earth-Moon plane and pointing in the direction of the Moon's orbital motion, and the  $\zeta$ -axis completing the right-handed coordinate system.
2. Local vertical inertial rectangular (LVIR) coordinate frame: Centered at either vehicle with the radial-axis along the negative position vector, the out-of-plane-axis along the crossproduct vector of the negative position and velocity vectors, and the downtrack-axis completing the right-handed coordinate system.
3. Target centered curvilinear coordinate frame: Centered at the target vehicle. The radial distance is defined as the distance between the target vehicle, when propagated in a circular orbit to a matching phase angle

with the chaser vehicle, and the chaser vehicle in a radial direction. The out-of-plane distance is defined as the distance between the target vehicle and the chaser vehicle in the out-of-plane direction. The downtrack distance is defined as the curvilinear distance along the propagated circular target orbit. The positive direction for all three axes is defined in the same manner as the LVIR coordinate frame.

4. Body centered coordinate frame: Centered at the chaser vehicle and transformed from the LVIR coordinate frame by a yaw-pitch-roll set of Euler angles.
5. Sensor centered coordinate frame: Centered at a specified point in the body centered coordinated frame and transformed from the body centered coordinate frame by a yaw-pitch-roll set of Euler Angles.

## 7.2 Main Simulation Functional Description

The main simulation consists of five primary modules plus several support modules. Figure 7.1 shows an overview of how these five modules interact to form the guidance and navigation system. Figures 7.2 and 7.3 summarize how the target, chaser and estimated trajectories are initialized and integrate from the initial condition (*IC*) to the beginning of the rendezvous profile (*TI*) and finally to the time of rendezvous (*TF*).

### 7.2.1 Target Vehicle Environment Module

Figure 7.4 gives the functional description of the target vehicle module. The target vehicle can be placed in an  $\mathcal{H}_2$  guided halo orbit or in a planar circular orbit by a selectable flag. In either case, the target vehicle remains

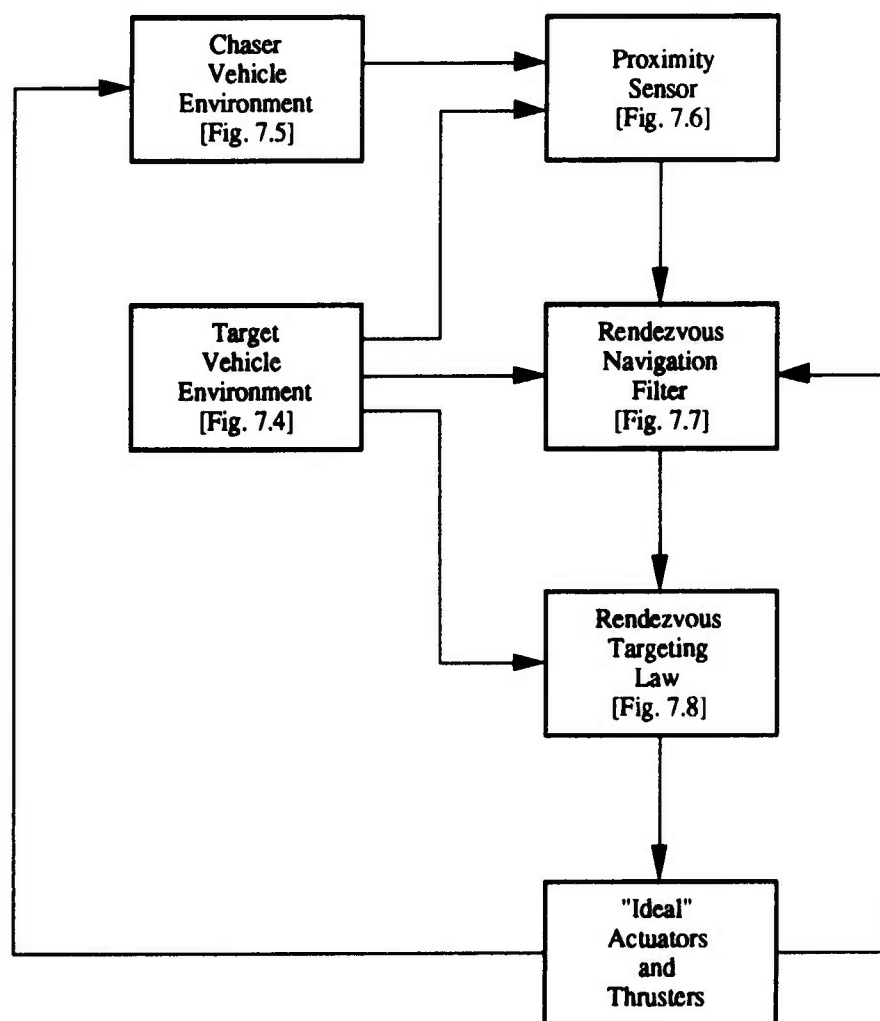
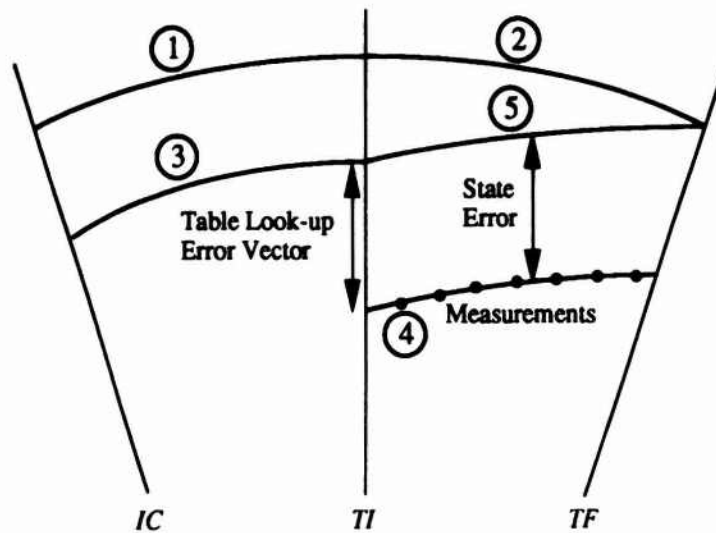


Figure 7.1: Guidance and Navigation System Functional Description



① Target Vehicle Propagation  
 $\dot{x}_t = f_1(x_t) + B_G u_t + w_{dt}$   
 $w_{dt} \sim N(0, \Pi_{dt} \Pi_{dt}^T)$

② Target Vehicle Environment  
 $\dot{x}_t = f_1(x_t) + B_G u_t + w_{dt}$   
 $w_{dt} \sim N(0, \Pi_{dt} \Pi_{dt}^T)$

③ Chaser Vehicle Propagation  
 $\dot{x}_c = f_1(x_c) + B_G u_c + w_{dc}$   
 $w_{dc} \sim N(0, \Pi_{dc} \Pi_{dc}^T)$

④ Chaser Vehicle Environment  
 $\dot{x}_c = f_1(x_c) + w_e$   
 $w_e \sim N(0, \Pi_e \Pi_e^T)$

⑤ State Estimate  
 $\dot{\hat{z}} = f_2(\hat{z})$

Figure 7.2:  $\mathcal{H}_2$  Guided Halo Orbit Trajectories

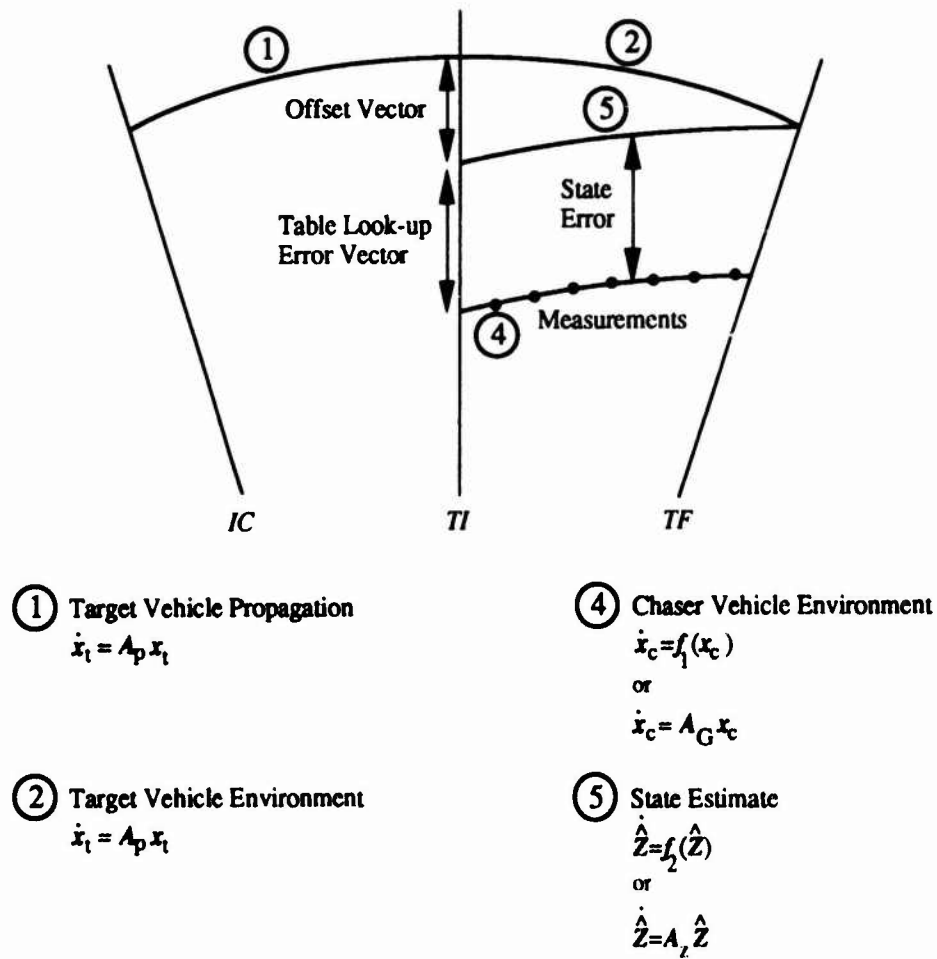
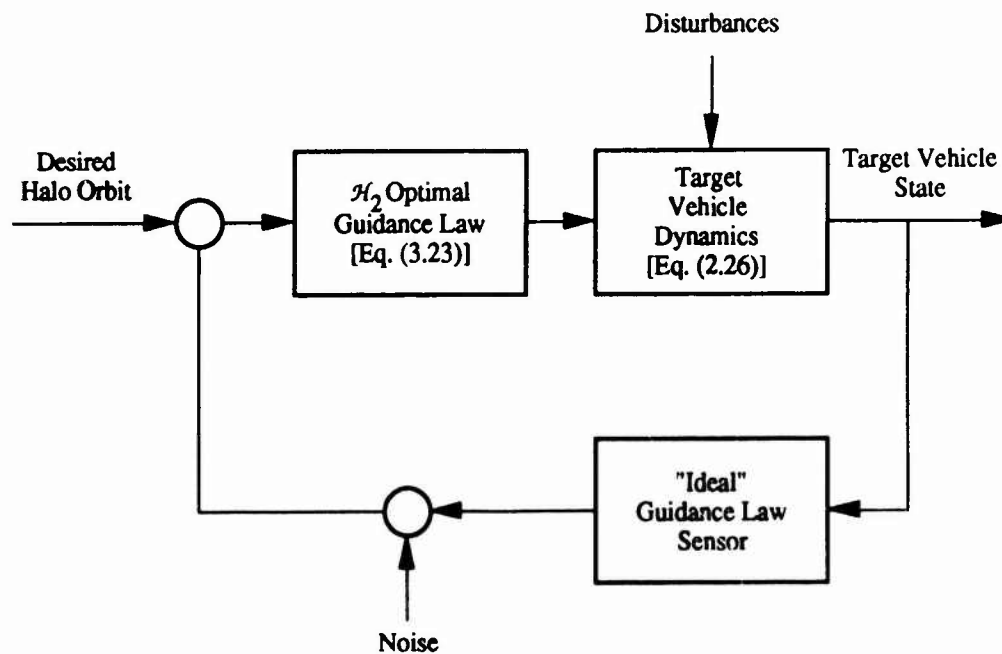
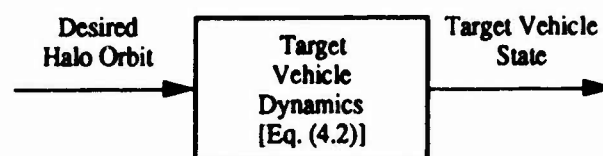


Figure 7.3: Planar Circular Orbit Trajectories



(a) Target Vehicle in  $\mathcal{H}_2$  Guided Halo Orbit

(b) Target Vehicle in Planar Circular Orbit

Figure 7.4: Target Vehicle Environment Functional Description

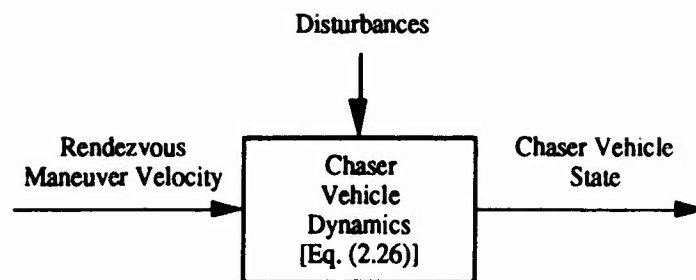
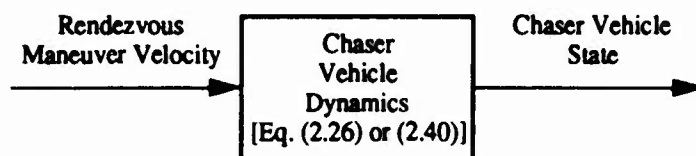
passive with respect to the rendezvous profile.

For a  $\mathcal{H}_2$  guided halo orbit, the target vehicle's initial states and time are selectable. Orbital rotation is dependent on these states. The target vehicle dynamics consists of the circular restricted three-body equations of motion. The amount of disturbances added to the target vehicle dynamics is selectable. Position measurements for the guidance law are generated assuming a "ideal" guidance law sensor. The amount of measurement noise added to these "ideal" measurements is selectable. The fixed power spectrum for the disturbances and measurement noise is selectable but must be consistent with the state space realization of the guidance law. Further, the non-dimensional frequency and radius of the desired halo orbit are selectable but must also be consistent with the guidance law.

If a planar circular orbit is selected, the orbit's orientation with respect to the  $\eta$ - $\zeta$  plane (incline angle) is specified by a selectable distance. Its orbital rotation (clockwise or counterclockwise) is controlled through a separate selectable parameter. The initial states are computed automatically using the selectable non-dimensional frequency and radius of the halo orbit in addition to its initial time. The initial time of the target vehicle is computed using the selectable chaser vehicle's  $TI$  downtrack offset position and the target vehicle's non-dimensional frequency and halo orbit radius. The target vehicle's dynamics consists of simple second order linear time invariant differential equations that are only a function of the non-dimensional frequency.

### 7.2.2 Chaser Vehicle Environment Module

Figure 7.5 depicts the functional description of the chaser vehicle module during the rendezvous profile; Fig. 7.4 (a) would apply to the chaser

(a) Target Vehicle in  $\mathcal{H}_2$  Guided Halo Orbit

(b) Target Vehicle in Planar Circular Orbit

Figure 7.5: Chaser Vehicle Environment Functional Description

vehicle prior to TI if the target vehicle is in a  $\mathcal{H}_2$  guided halo orbit. In this case, the chaser vehicle is initialize in an independent  $\mathcal{H}_2$  guided halo orbit (see Fig. 7.2). The initial chaser vehicle state and time are selectable. For integration from the initial time to  $TI$ , the chaser vehicle dynamics consists of the circular restricted three-body equations of motion plus a  $\mathcal{H}_2$  optimal guidance law. The amount of disturbances added to the chaser vehicle dynamics is selectable. The position measurements for the guidance law are generated assuming a “ideal” guidance law sensor. The amount of measurement noise added to these “ideal” measurements is selectable. The fixed power spec-

trum for the disturbances and measurement noise is selectable but must be consistent with the state space realization of the guidance law. Further, the non-dimensional frequency and radius of the desired halo orbit are selectable but must also be consistent with the guidance law.

During the rendezvous profile, the chaser vehicle is assumed to be in coasting flight. The initial state and time are taken as the last state prior to  $TI$  plus a table look-up error vector and  $TI$  TIG, respectively. The chaser vehicle dynamics consists of the circular three-body equations of motion. The amount of disturbances added to the chaser vehicle dynamics is selectable and is independent of the pre- $TI$  phase. The fixed power spectrum for the disturbances is also selectable and independent of the pre- $TI$  phase.

If the target vehicle is in a planar circular halo orbit, the chaser vehicle is initialize at  $TI$  based on selectable offsets from the target vehicle assuming a coelliptic orbit. A table look-up error vector is added to this computation (see Fig. 7.3). The chaser vehicle's time is assumed to be  $TI$  TIG. The chaser vehicle is assumed to be in coasting flight, its dynamics consists of either the nonlinear or linear circular restricted three-body equations of motion depending on a selectable flag.

### 7.2.3 Proximity Sensor Module

Figure 7.6 shows the functional description of the proximity sensor module. The proximity sensor module is modeled after the Space Shuttle rendezvous radar [44] and considers four types of measurements: relative range, relative range rate, and two line-of-sight angles. The line-of-sight angles used by the rendezvous navigation filter are roll and pitch angles in the body centered coordinate frame and are computed directly from the shaft and trunnion

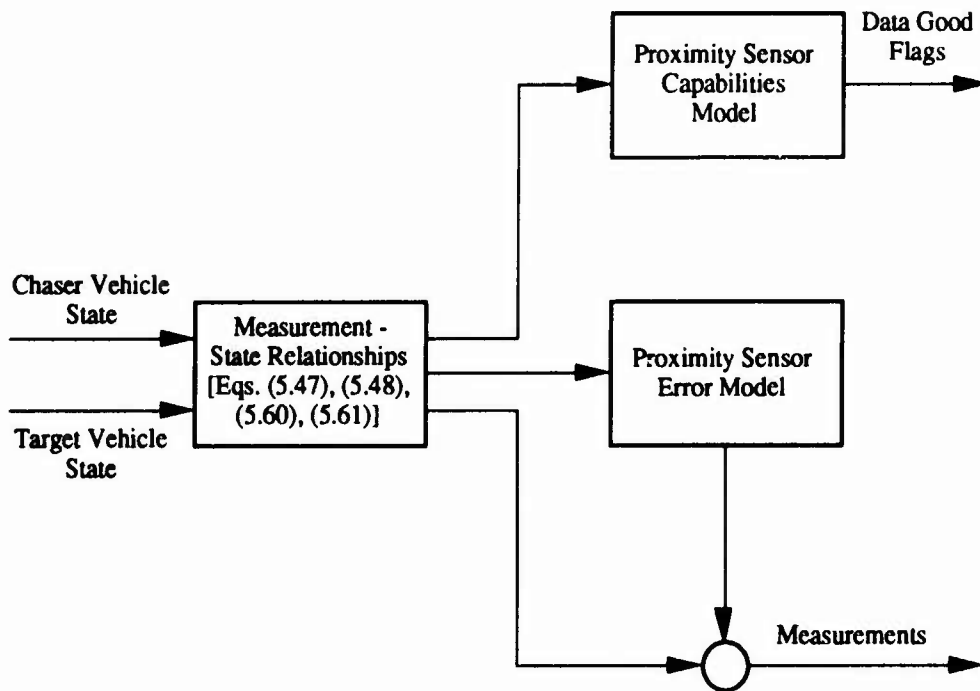


Figure 7.6: Proximity Sensor Functional Description

angles in the sensor centered coordinate frame.

All measurements are generated regardless of whether or not they are used by the rendezvous navigation filter. The "ideal" measurements are checked by the sensor capabilities model to ensure that they are within sensor hardware limits; these limits are selectable. If the generated measurement is outside of the sensor hardware limits, the data good flag associated with that measurement type is set to "bad."

The addition of random noise to the "ideal" measurements is done in the sensor error model and is selectable. Characteristics of the random noise are also selectable. The sensor error model also has the capability to add random biases to each measurement. This addition is independent of the random noise addition and is selectable. The random bias is computed only once per phase; phases are defined by the range to the target vehicle. Characteristics of the random biases are also selectable.

#### **7.2.4 Rendezvous Navigation Module**

Figure 7.7 gives the functional description of the rendezvous navigation filter. The rendezvous navigation module is formulated as a continuous dynamics, discrete measurements extended Kalman filter. Measurements are generated by the proximity sensor module and may be incorporated into the filter in any combination; that is, relative range and line-of-sight angles, or relative range and range rate, etc. The rendezvous navigation filter checks the data good flag of each measurement used; if any data good flag of a measurement selected is "bad," the entire set of measurements is rejected.

The estimated states consist of the chaser vehicle inertial state plus either, both or neither of unmodeled accelerations acting on the chaser vehi-

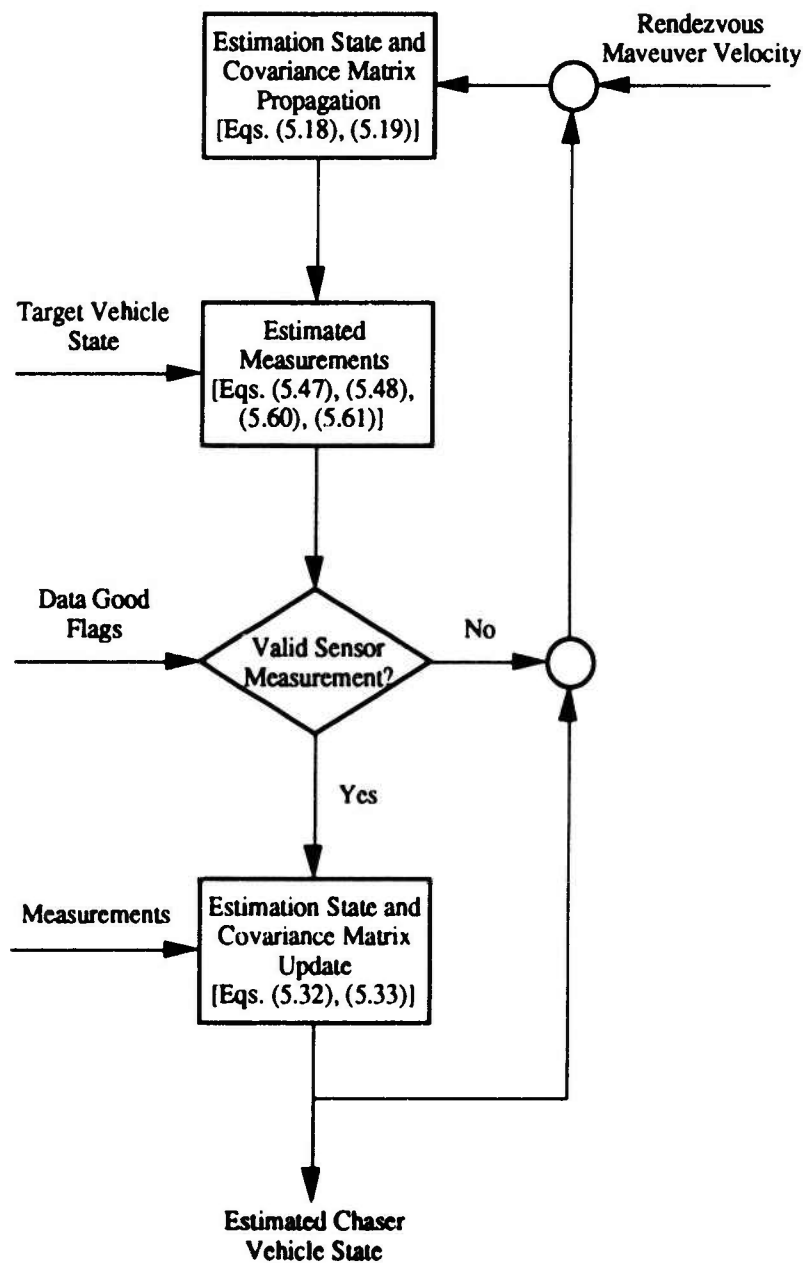


Figure 7.7: Rendezvous Navigation Functional Description

cle and measurement biases. Which states are estimated is selectable. The unmodeled accelerations and measurement biases are each modeled as a first order Gauss-Markov process with selectable time constants. Initialization of the estimated chaser vehicle states is either the pre-*TI* chaser vehicle states for a  $\mathcal{H}_2$  guided halo orbit or the pre-*TI* target vehicle states plus an offset position for a planar circular orbit (see Figs. 7.2 and 7.3). Initial values of the unmodeled accelerations and measurement biases are selectable. The initial time associated with the estimation states is *TI* TIG.

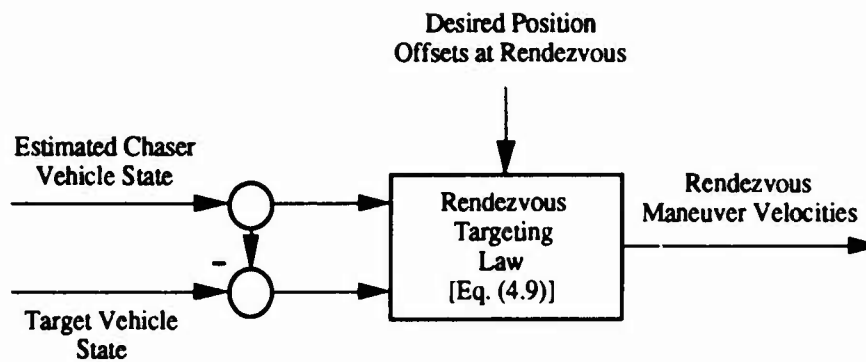
The initial covariance matrix assumes a diagonal form and has a selectable standard deviation for each estimated state. The values associated with the estimated chaser vehicle states are used to generate the table look-up error vectors for initialization of the chaser vehicle environment. The fixed power spectrum matrix for the process and measurement noise terms assume a diagonal form and have a selectable standard deviation for each parameter.

Each sensor pass is specified by start and stop times, number of measurements taken, and measurement set type. All of these parameters are selectable for each sensor pass. For each midcourse correction maneuver, the covariance matrix is enlarged to reflect the uncertainty in the maneuver execution. During this enlargement, the uncertainty in the estimated chaser vehicle velocity states is increased by a selectable amount while the overall correlation coefficient matrix is preserved.

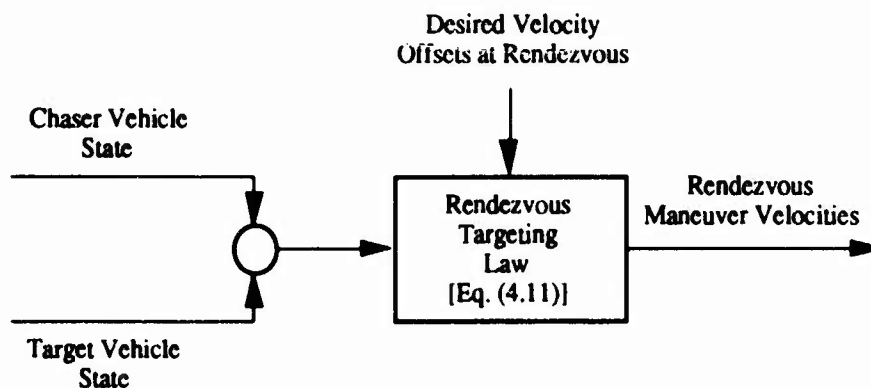
### 7.2.5 Rendezvous Targeting Module

Figure 7.8 gives the functional description of the rendezvous targeting module. The *TI* and *MCC* maneuvers are computed from the estimated chaser vehicle state and target vehicle state to satisfy the desired position off-





(a) Terminal Phase Initiation and Midcourse Correction Targeting Law



(b) Terminal Phase Final Targeting Law

Figure 7.8: Rendezvous Targeting Functional Description

set at the time of rendezvous. The position offset at the time of rendezvous is selectable.

Two rendezvous targeting laws have been implemented in the simulation for the *TI* and *MCC* maneuvers. The first law is developed in Chapter 4; the second law is an approximation of the first and consists of straight line motion. Choosing which targeting law is used is accomplished with a selectable flag. An iteration cycle eliminates the error due to the chaser vehicle linearization process in the targeting law development; the iteration tolerance and maximum number of iteration cycles are selectable.

The TF maneuver is computed to satisfy the desired velocity offsets at the time of rendezvous; these offsets are selectable. The chaser vehicle and target vehicle states are used in this computation.

#### **7.2.6 Support Modules**

A Runge-Kutta 7(8) numerical integrator is used for all integration. The initial time step, absolute error and relative error are selectable. Each integration interval may be broken up into sub-intervals for data storage. The number of sub-intervals is selectable and applies to all integration intervals except those intervals in the middle of a sensor pass.

All noises used in this simulation are generated by an IMSL pseudo-random number generator from a standard normal distribution using an acceptance-rejection method. The seed for the IMSL pseudo-random number generator is selectable.

Available output from the main simulation consists of digital data displays, plots, and data files. The first two digital data displays provide a maneuver summary of the rendezvous profile; each maneuver is detailed in terms

of the velocity required and relative position at the time of the maneuver. Two additional displays are available which list any proximity sensor measurements that were rejected and the final measurement residual statistics. Seventy plots are available which show the relative trajectory; environment and estimated state time histories; and estimation error, covariance, and correlation coefficient time histories. Eighteen raw data files can be store by the main simulation; selectable data storage flags are used to designate which data is stored for each individual profile executed.

### **7.3 Pre-Processor Program**

The pre-processor program is an interactive parameter input program used to define approximately 500 selectable parameters required by the main simulation. For example, these parameters specify how many rendezvous maneuvers and sensor passes are to be executed as well as the times associated with these maneuvers and passes. They define the initial chaser and target vehicle conditions and orbits. They also control the capabilities and characteristics of the rendezvous navigation filter and the proximity sensor. Table 7.1 lists the main menu options for the pre-processor program. When the pre-processor program is exited, two data files are stored with the updated values of all parameters; these data files are used to initialize the main simulation.

### **7.4 Post-Processor Program**

The post-processor program edits stored data and computes variables of interest such as the statistics on the measurement residuals from the rendezvous navigation filter; this program is also completely interactive. Sixteen of the 18 raw data files can be edited in the sense that data from the raw

Table 7.1: Pre-Processor Program Main Menu

Module	
1	Rendezvous Parameters (TIGs)
2	Rendezvous Targeting Parameters
3	Sensor Passes (Time)
4	Chaser Vehicle Halo Orbit Parameters
5	Chaser Vehicle Initial Conditions
6	Chaser Vehicle <i>TI</i> Error Vectors
7	Target Vehicle Halo Orbit Parameters
8	Target Vehicle Initial Conditions
9	Filter Covariance <i>TI</i> Conditions
10	Filter Unmodeled Acceleration <i>TI</i> Conditions
11	Filter Measurement Bias and Noise <i>TI</i> Conditions
12	Filter Process Noise <i>TI</i> Conditions
13	Filter Error Plot Scales (Inertial)
14	Filter Error Plot Scales (LVIR)
15	Sensor Biases
16	Sensor Errors
17	Sensor Limits
18	Three-Body System Parameters
19	Numerical Integrator Parameters
20	Data Storage Flags
21	Miscellaneous Parameters
99	Exit Program

data file will be stored in a processed data file at a selectable interval. In this fashion very large data files can be reduced for plotting purposes. These raw data files are never written over or deleted.

The data file containing the plotting scales for the estimation error plots can be completely edited. This is allowed so that specific areas on the estimation error plots can be enlarged without re-executing the main simulation or editing the plotting command file. The last raw data file (for miscellaneous parameter storage) can not be edited. Table 7.2 lists the main menu for the post-processor program and which raw data files are available for editing. The type of data stored in each file is also given.

Table 7.2: Post-Processor Program Main Menu

	Data File	Data Type
1	chaser_env.dat	Chaser Environment
2	chaser_est.dat	Estimated States
3	chaser_guid.dat	Chaser Guidance States
4	tgt_env.dat	Target Environment
5	tgt_guid.dat	Target Guidance States
6	relmo.dat	Relative Motion Data
7	err_inertial.dat	Inertial Estimation Error
8	cov_inertial.dat	Inertial Covariance
9	cc_inertial.dat	Inertial Correlation Coefficient
10	err_lvir.dat	LVIR Estimation Error
11	cov_lvir.dat	LVIR Covariance
12	cc_lvir.dat	LVIR Correlation Coefficient
13	scales.dat	Error Plot Scales
14	meas.dat	Measurement Data
15	residuals.dat	Measurement Residuals
16	updates.dat	State Updates
17	fom.dat	Filter Figures-of-Merit
99	Exit Program	

## Chapter 8

### Conclusions

A guidance law has been developed using  $\mathcal{H}_2$  control theory which stabilizes the translunar halo orbit in the circular restricted three-body problem. This guidance law minimizes the position deviation from the desired halo orbit plus the control acceleration. Linear simulation results validated the guidance law. Further, the halo orbit guidance problem has been formulated in the frequency-domain. Other frequency-domain design techniques, such as  $\mathcal{H}_\infty$  control theory, are now directly applicable. In addition, the effect of halo orbit frequency, position weighting factor and the amount of process or measurement noise present has been quantified.

A two spacecraft terminal phase rendezvous targeting law has been developed which is valid for the circular restricted three-body problem. This targeting law was demonstrated using a small radius translunar halo orbit. In addition, several characteristics of three-body rendezvous were observed. First, terminal phase rendezvous in the circular restricted three body problem is three-dimensional; out-of-plane relative motion with respect to the target vehicle's halo orbit occurs. Further, the relative trajectory between the chaser and target vehicles is also three-dimensional. Secondly, a trade-off exists between targeting law error, out-of-plane relative motion and the total propulsion cost of the rendezvous profile. A rendezvous profile initiated at the top or bottom of the halo orbit produces less targeting law error, but requires greater total propulsion cost and produces larger out-of-plane relative

motion; a rendezvous profile initiated on either side of the halo orbit requires less total propulsion cost and produces less out-of-plane relative motion, but has greater targeting law error. Thirdly, final out-of-plane errors generally dominate both downtrack and radial errors. Lastly, a minimum total propulsion cost rendezvous profile exists and is a function of transfer time, incline angle and initial condition angle.

A rendezvous navigation filter capable of supplying the rendezvous targeting law with chaser vehicle state information has been developed. Estimation errors converged quickly after only a few relative range and line-of-sight angle measurements were incorporated. The placement of a midcourse correction maneuver was not directly dependent on navigation errors or final position error sensitivities. Hence, the midcourse correction maneuvers were placed in the rendezvous profile based on time.

Four total cases, two rendezvous profiles for the translunar planar circular orbit and two equivalent rendezvous profiles for the  $\mathcal{H}_2$  guided translunar halo orbit, were examined to demonstrate the entire guidance and navigation system as applied to the two spacecraft terminal phase rendezvous scenario in the circular restricted three-body problem. In each case, total propulsion requirements were less than 1.5 m/s and final miss distance was less than 26 m. State estimation errors were small and showed no substantial performance degradation due to the rendezvous profile geometry. The translunar planar circular orbit displayed the same characteristics as the  $\mathcal{H}_2$  guided translunar halo orbit, although the propulsion requirements and final miss distance were generally larger in the  $\mathcal{H}_2$  guided translunar halo orbit demonstration.

A nonlinear simulation package for terminal phase rendezvous guidance and navigation system evaluation has been developed. The pre-processor



and post-processor programs are completely interactive; the main simulation program requires no interactive input. The simulation is constructed modularly so it can be adapted to different rendezvous scenarios in any three-body system with a minimum of modification. The simulation source code is fully documented and provides processing status messages at regular intervals.

## Appendix A

### State Transition Matrices

#### A.1 Linearized Equations of Motion

Using the  $A_G$  matrix given in Eq. (2.43), the state transition matrix,  $\Phi_G(t, 0)$ , can be computed from Eq. (2.47) where

$$\Phi_G(t, 0) = \begin{bmatrix} \phi_{G11} & \phi_{G12} \\ \phi_{G21} & \phi_{G22} \end{bmatrix} \quad (A.1)$$

and

$$\phi_{G11} = \begin{bmatrix} \phi_{G111} & \phi_{G112} & 0 \\ \phi_{G114} & \phi_{G115} & 0 \\ 0 & 0 & \phi_{G119} \end{bmatrix} \quad (A.2)$$

$$\begin{aligned} \phi_{G111} = & 0.667355 \exp^{2.158677t} + 0.667355 \exp^{-2.158677t} \\ & - 0.334710 \cos(1.862647t) \end{aligned} \quad (A.3)$$

$$\begin{aligned} \phi_{G112} = & -0.124821 \exp^{2.158677t} + 0.124821 \exp^{-2.158677t} \\ & + 0.289317 \sin(1.862647t) \end{aligned} \quad (A.4)$$

$$\begin{aligned} \phi_{G114} = & -0.420595 \exp^{2.158677t} + 0.420595 \exp^{-2.158677t} \\ & + 0.974880 \sin(1.862647t) \end{aligned} \quad (A.5)$$

$$\begin{aligned} \phi_{G115} = & 0.0786672 \exp^{2.158677t} + 0.0786672 \exp^{-2.158677t} \\ & + 0.842666 \cos(1.862647t) \end{aligned} \quad (A.6)$$

$$\phi_{G119} = \cos(1.786178t) \quad (A.7)$$

$$\phi_{G12} = \begin{bmatrix} \phi_{G121} & \phi_{G122} & 0 \\ \phi_{G124} & \phi_{G125} & 0 \\ 0 & 0 & \phi_{G129} \end{bmatrix} \quad (\text{A.8})$$

$$\begin{aligned} \phi_{G121} &= 0.195181 \exp^{2.158677t} - 0.195181 \exp^{-2.158677t} \\ &\quad + 0.0844681 \sin(1.862647t) \end{aligned} \quad (\text{A.9})$$

$$\begin{aligned} \phi_{G122} &= 0.123011 \exp^{2.158677t} + 0.123011 \exp^{-2.158677t} \\ &\quad - 0.246022 \cos(1.862647t) \end{aligned} \quad (\text{A.10})$$

$$\begin{aligned} \phi_{G124} &= -0.123011 \exp^{2.158677t} - 0.123011 \exp^{-2.158677t} \\ &\quad + 0.246022 \cos(1.862647t) \end{aligned} \quad (\text{A.11})$$

$$\begin{aligned} \phi_{G125} &= -0.0775268 \exp^{2.158677t} + 0.0775268 \exp^{-2.158677t} \\ &\quad + 0.716566 \sin(1.862647t) \end{aligned} \quad (\text{A.12})$$

$$\phi_{G129} = 0.559855 \sin(1.786178t) \quad (\text{A.13})$$

$$\phi_{G21} = \begin{bmatrix} \phi_{G211} & \phi_{G212} & 0 \\ \phi_{G214} & \phi_{G215} & 0 \\ 0 & 0 & \phi_{G219} \end{bmatrix} \quad (\text{A.14})$$

$$\begin{aligned} \phi_{G211} &= 1.440604 \exp^{2.158677t} - 1.440604 \exp^{-2.158677t} \\ &\quad + 0.623447 \sin(1.862647t) \end{aligned} \quad (\text{A.15})$$

$$\begin{aligned} \phi_{G212} &= -0.269448 \exp^{2.158677t} - 0.269448 \exp^{-2.158677t} \\ &\quad + 0.538895 \cos(1.862647t) \end{aligned} \quad (\text{A.16})$$

$$\begin{aligned} \phi_{G214} &= -0.907929 \exp^{2.158677t} - 0.907929 \exp^{-2.158677t} \\ &\quad + 1.815857 \cos(1.862647t) \end{aligned} \quad (\text{A.17})$$

$$\begin{aligned} \phi_{G215} &= 0.169817 \exp^{2.158677t} - 0.169817 \exp^{-2.158677t} \\ &\quad - 1.569589 \sin(1.862647t) \end{aligned} \quad (\text{A.18})$$

$$\phi_{G219} = -1.786178 \sin(1.786178t) \quad (\text{A.19})$$

$$\phi_{G22} = \begin{bmatrix} \phi_{G221} & \phi_{G222} & 0 \\ \phi_{G224} & \phi_{G225} & 0 \\ 0 & 0 & \phi_{G229} \end{bmatrix} \quad (\text{A.20})$$

$$\begin{aligned} \phi_{G221} &= 0.421333 \exp^{2.158677t} - 0.421333 \exp^{-2.158677t} \\ &\quad + 0.157334 \cos(1.862647t) \end{aligned} \quad (\text{A.21})$$

$$\begin{aligned} \phi_{G222} &= 0.265541 \exp^{2.158677t} - 0.265541 \exp^{-2.158677t} \\ &\quad + 0.458252 \sin(1.862647t) \end{aligned} \quad (\text{A.22})$$

$$\begin{aligned} \phi_{G224} &= -0.265541 \exp^{2.158677t} + 0.265541 \exp^{-2.158677t} \\ &\quad - 0.458252 \sin(1.862647t) \end{aligned} \quad (\text{A.23})$$

$$\begin{aligned} \phi_{G225} &= -0.167355 \exp^{2.158677t} - 0.167355 \exp^{-2.158677t} \\ &\quad + 1.334710 \cos(1.862647t) \end{aligned} \quad (\text{A.24})$$

$$\phi_{G229} = \cos(1.786178t). \quad (\text{A.25})$$

## A.2 Rendezvous Targeting Law

The rendezvous targeting law given in Eq. (4.9) is dependent on the state transition matrix computed from the relative state equation, Eq. (4.6).

Hence,

$$\begin{bmatrix} \dot{\phi}_{11} & \dot{\phi}_{12} & \vdots & \dot{\phi}_{13} & \dot{\phi}_{14} \\ \dot{\phi}_{21} & \dot{\phi}_{22} & \vdots & \dot{\phi}_{23} & \dot{\phi}_{24} \\ \dots & \dots & \dots & \dots & \dots \\ 0 & 0 & \vdots & \dot{\phi}_{33} & \dot{\phi}_{34} \\ 0 & 0 & \vdots & \dot{\phi}_{43} & \dot{\phi}_{44} \end{bmatrix} = \begin{bmatrix} \mathbf{A}_G & \vdots & (\mathbf{A}_G - \mathbf{A}_p) \\ \dots & \dots & \dots \\ 0 & \vdots & \mathbf{A}_p \end{bmatrix}$$

$$\times \begin{bmatrix} \phi_{11} & \phi_{12} & \vdots & \phi_{13} & \phi_{14} \\ \phi_{21} & \phi_{22} & \vdots & \phi_{23} & \phi_{24} \\ \dots & \dots & \dots & \dots & \dots \\ 0 & 0 & \vdots & \phi_{33} & \phi_{34} \\ 0 & 0 & \vdots & \phi_{43} & \phi_{44} \end{bmatrix}. \quad (\text{A.26})$$

Solving for the submatrices of interest yields

$$\phi_{11} = \begin{bmatrix} \phi_{111} & \phi_{112} & 0 \\ \phi_{114} & \phi_{115} & 0 \\ 0 & 0 & \phi_{119} \end{bmatrix} \quad (\text{A.27})$$

$$\begin{aligned} \phi_{111} = & 0.667355 \exp^{2.158677(t_2-t_1)} + 0.667355 \exp^{-2.158677(t_2-t_1)} \\ & - 0.334710 \cos(1.862647(t_2 - t_1)) \end{aligned} \quad (\text{A.28})$$

$$\begin{aligned} \phi_{112} = & -0.124821 \exp^{2.158677(t_2-t_1)} + 0.124821 \exp^{-2.158677(t_2-t_1)} \\ & + 0.289317 \sin(1.862647(t_2 - t_1)) \end{aligned} \quad (\text{A.29})$$

$$\begin{aligned} \phi_{114} = & -0.420595 \exp^{2.158677(t_2-t_1)} + 0.420595 \exp^{-2.158677(t_2-t_1)} \\ & + 0.974880 \sin(1.862647(t_2 - t_1)) \end{aligned} \quad (\text{A.30})$$

$$\begin{aligned} \phi_{115} = & 0.078667 \exp^{2.158677(t_2-t_1)} + 0.078667 \exp^{-2.158677(t_2-t_1)} \\ & + 0.842666 \cos(1.862647(t_2 - t_1)) \end{aligned} \quad (\text{A.31})$$

$$\phi_{119} = \cos(1.786178(t_2 - t_1)) \quad (\text{A.32})$$

$$\phi_{12} = \begin{bmatrix} \phi_{121} & \phi_{122} & 0 \\ \phi_{124} & \phi_{125} & 0 \\ 0 & 0 & \phi_{129} \end{bmatrix} \quad (\text{A.33})$$

$$\begin{aligned} \phi_{121} = & 0.195181 \exp^{2.158677(t_2-t_1)} - 0.195181 \exp^{-2.158677(t_2-t_1)} \\ & + 0.084468 \sin(1.862647(t_2 - t_1)) \end{aligned} \quad (\text{A.34})$$

$$\phi_{122} = 0.123011 \exp^{2.158677(t_2-t_1)} + 0.123011 \exp^{-2.158677(t_2-t_1)}$$

$$-0.246022 \cos(1.862647(t_2 - t_1)) \quad (\text{A.35})$$

$$\begin{aligned} \phi_{124} = & -0.123011 \exp^{2.158677(t_2 - t_1)} - 0.123011 \exp^{-2.158677(t_2 - t_1)} \\ & + 0.246022 \cos(1.862647(t_2 - t_1)) \end{aligned} \quad (\text{A.36})$$

$$\begin{aligned} \phi_{125} = & -0.077527 \exp^{2.158677(t_2 - t_1)} + 0.077527 \exp^{-2.158677(t_2 - t_1)} \\ & + 0.716566 \sin(1.862647(t_2 - t_1)) \end{aligned} \quad (\text{A.37})$$

$$\phi_{129} = 0.559855 \sin(1.786178(t_2 - t_1)) \quad (\text{A.38})$$

$$\phi_{13} = \begin{bmatrix} \phi_{131} & \phi_{132} & 0 \\ \phi_{134} & \phi_{135} & 0 \\ 0 & 0 & \phi_{139} \end{bmatrix} \quad (\text{A.39})$$

$$\begin{aligned} \phi_{131} = & 0.667335 \exp^{2.158677(t_2 - t_1)} + 0.667335 \exp^{-2.158677(t_2 - t_1)} \\ & - 0.334710 \cos(1.862647(t_2 - t_1)) - \cos(f(t_2 - t_1)) \end{aligned} \quad (\text{A.40})$$

$$\begin{aligned} \phi_{132} = & -0.124820 \exp^{2.158677(t_2 - t_1)} + 0.124820 \exp^{-2.158677(t_2 - t_1)} \\ & + 0.289316 \sin(1.862647(t_2 - t_1)) \end{aligned} \quad (\text{A.41})$$

$$\begin{aligned} \phi_{134} = & -0.420595 \exp^{2.158677(t_2 - t_1)} + 0.420595 \exp^{-2.158677(t_2 - t_1)} \\ & + 0.974860 \sin(1.862647(t_2 - t_1)) \end{aligned} \quad (\text{A.42})$$

$$\begin{aligned} \phi_{135} = & 0.078667 \exp^{2.158677(t_2 - t_1)} + 0.078667 \exp^{-2.158677(t_2 - t_1)} \\ & + 0.842666 \cos(1.862647(t_2 - t_1)) - \cos(f(t_2 - t_1)) \end{aligned} \quad (\text{A.43})$$

$$\phi_{139} = \cos(1.786178(t_2 - t_1)) - \cos(f(t_2 - t_1)) \quad (\text{A.44})$$

$$\phi_{14} = \begin{bmatrix} \phi_{141} & \phi_{142} & 0 \\ \phi_{144} & \phi_{145} & 0 \\ 0 & 0 & \phi_{149} \end{bmatrix} \quad (\text{A.45})$$

$$\begin{aligned} \phi_{141} = & 0.195181 \exp^{2.158677(t_2 - t_1)} - 0.195181 \exp^{-2.158677(t_2 - t_1)} \\ & + 0.084468 \sin(1.862647(t_2 - t_1)) - \frac{1}{f} \sin(f(t_2 - t_1)) \end{aligned} \quad (\text{A.46})$$

$$\begin{aligned}\phi_{142} = & 0.123011 \exp^{2.158677(t_2 - t_1)} + 0.123011 \exp^{-2.158677(t_2 - t_1)} \\ & - 0.246022 \cos(1.862647(t_2 - t_1))\end{aligned}\quad (\text{A.47})$$

$$\begin{aligned}\phi_{144} = & -0.123011 \exp^{2.158677(t_2 - t_1)} - 0.123011 \exp^{-2.158677(t_2 - t_1)} \\ & + 0.246022 \cos(1.862647(t_2 - t_1))\end{aligned}\quad (\text{A.48})$$

$$\begin{aligned}\phi_{145} = & -0.077526 \exp^{2.158677(t_2 - t_1)} + 0.077526 \exp^{-2.158677(t_2 - t_1)} \\ & + 0.716565 \sin(1.862647(t_2 - t_1)) - \frac{1}{f} \sin(f(t_2 - t_1))\end{aligned}\quad (\text{A.49})$$

$$\phi_{149} = 0.559855 \sin(1.786178(t_2 - t_1)) - \frac{1}{f} \sin(f(t_2 - t_1)).\quad (\text{A.50})$$

## Appendix B

### Halo Orbit Guidance Law Data

#### B.1 Representative $\mathcal{H}_2$ Guidance Law

The mid-range weighting parameters guidance law has the realization

$$\mathbf{K}_{halo} = \left[ \begin{array}{c|c} \mathbf{A}_K & \mathbf{B}_K \\ \hline \mathbf{C}_K & \mathbf{0} \end{array} \right] \quad (\text{B.1})$$

where Eqs. (3.24), (3.21) and (3.20) yield, respectively,

$$\mathbf{A}_K = \left[ \begin{array}{ccc} -91.9740 & 0.0011 & 0 \\ 0.0011 & -91.8698 & 0 \\ 0 & 0 & -91.8680 \\ -3533.1400 & 80.3422 & 0 \\ 76.7122 & -3518.3800 & 0 \\ 0 & 0 & -4066.0300 \\ 1.0000 & 0 & 0 \\ 0 & 1.0000 & 0 \\ 0 & 0 & 1.0000 \\ -14.1038 & 44.3486 & 0 \\ -2.0000 & 0 & 0 \\ 0 & 0 & -33.0702 \end{array} \right] \quad (\text{B.2})$$

$$\mathbf{B}_K = \left[ \begin{array}{ccc} 91.9740 & -0.0011 & 0 \\ -0.0011 & 91.8698 & 0 \\ 0 & 0 & 91.8680 \\ 3525.7600 & 76.5037 & 0 \\ -76.7122 & 3516.1900 & 0 \\ 0 & 0 & 3516.0200 \end{array} \right] \quad (\text{B.3})$$

$$\mathbf{C}_K = \left[ \begin{array}{ccc} -14.7617 & 156.8460 & 0 \\ 0 & 0 & -546.8190 \\ -14.1038 & 42.3486 & 0 \\ 0 & 0 & -33.0702 \end{array} \right] \quad (\text{B.4})$$



The transfer function matrix can be computed from the state space realization using

$$\mathbf{K}_{TF} = \mathbf{C}_K(s\mathbf{I} - \mathbf{A}_K)^{-1}\mathbf{B}_K + \mathbf{D}_K. \quad (\text{B.5})$$

Noting  $\mathbf{D}_K = \mathbf{0}$ , Eq. (B.5) yields

$$\mathbf{K}_{TF} = \begin{bmatrix} k_{11} & k_{12} & 0 \\ 0 & 0 & k_{23} \end{bmatrix} \quad (\text{B.6})$$

where

$$k_{11} = \frac{-54333.24(s + 1.06)(s^2 + 97.62s + 3832.80)}{(s^2 + 98.92s + 3813.24)(s^2 + 99.02s + 4573.70)} \quad (\text{B.7})$$

$$k_{12} = \frac{162235.98(s + 3.39)(s^2 + 91.28s + 3481.78)}{(s^2 + 98.92s + 3813.24)(s^2 + 99.02s + 4573.70)} \quad (\text{B.8})$$

$$k_{23} = \frac{-166510.64(s + 11.49)}{(s^2 + 124.94s + 7104.12)}. \quad (\text{B.9})$$

## B.2 Representative Time Histories

Figure B.1 shows steady state time histories for the system states; Fig. B.2 gives the estimation error. In these plots, (a-c) apply to the position states while (d-f) apply to the velocity states. Figure B.3 shows steady state time histories for the control acceleration required to produce the steady state positions and velocities.

## B.3 Representative Halo Orbits

Figure B.4 shows the front view of halo orbits with varying amounts of noise included in the simulation; Fig. B.5 gives the side view for the same cases.

## **B.4 Noise Statistics**

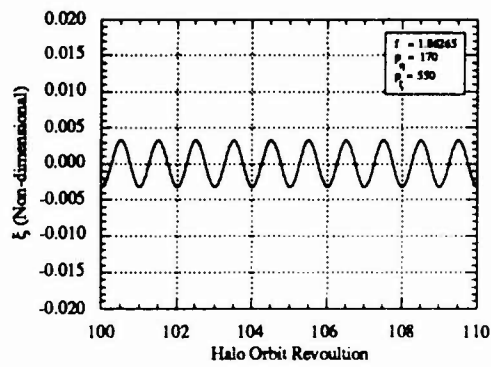
Figure B.6 shows the average standard deviation of the position and velocity states as a function of the standard deviation of the process noise. In both figures, the fixed power spectrum of the measurement noise is assumed to be  $2.665 \text{ m}^2/\text{s}$  in each axis.

## **B.5 Halo Orbit Frequency Parametric Study**

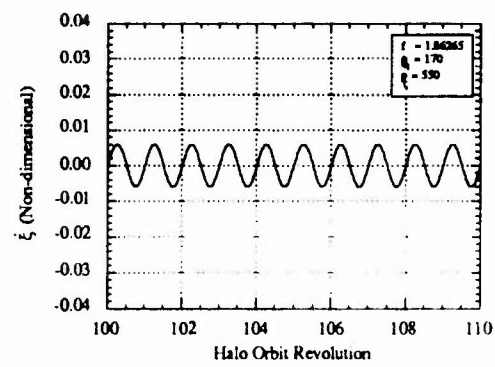
Figures B.7 and B.8 show the geometry and orientation of the halo orbit as a function of non-dimensional frequency. Figures B.9 and B.10 give the velocity required as a function of non-dimensional frequency in the  $\xi$  and  $\zeta$ -axes, respectively; Fig. B.11 applies to the total velocity required. In all these figures, (a-c) apply to cases with constant weighting in the  $\eta$ -axis and (d-f) apply to cases with constant weighting in the  $\zeta$  axis.

## **B.6 Control Weighting Factors Parametric Study**

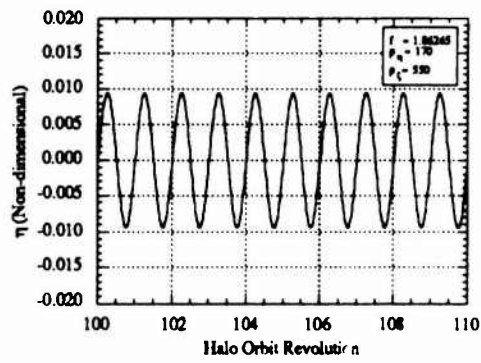
Figure B.12 shows the effect of the weighting factor in the  $\eta$ -axis for constant values of halo orbit frequency and weighting factor in the  $\zeta$ -axis. Figure B.13 shows the effect of the weighting factor in the  $\zeta$ -axis for constant values of halo orbit frequency and weighting factor in the  $\eta$ -axis.



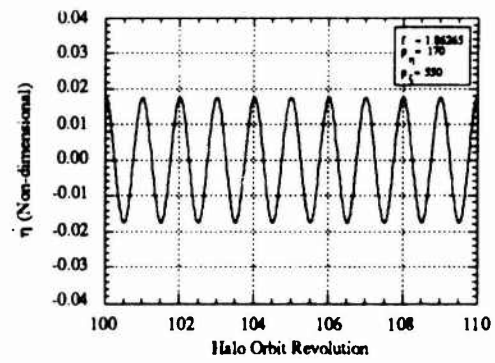
(a)



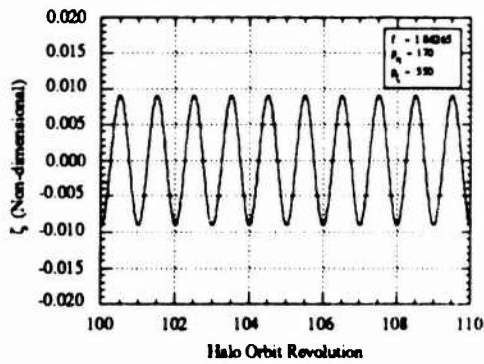
(d)



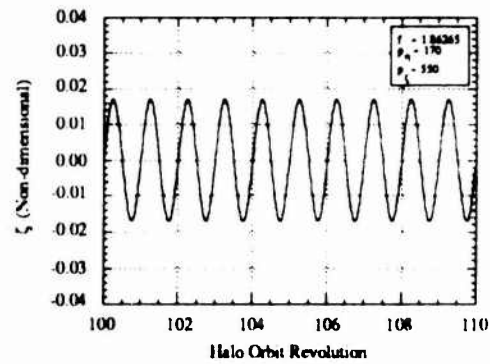
(b)



(e)



(c)



(f)

Figure B.1: Steady State Position and Velocity

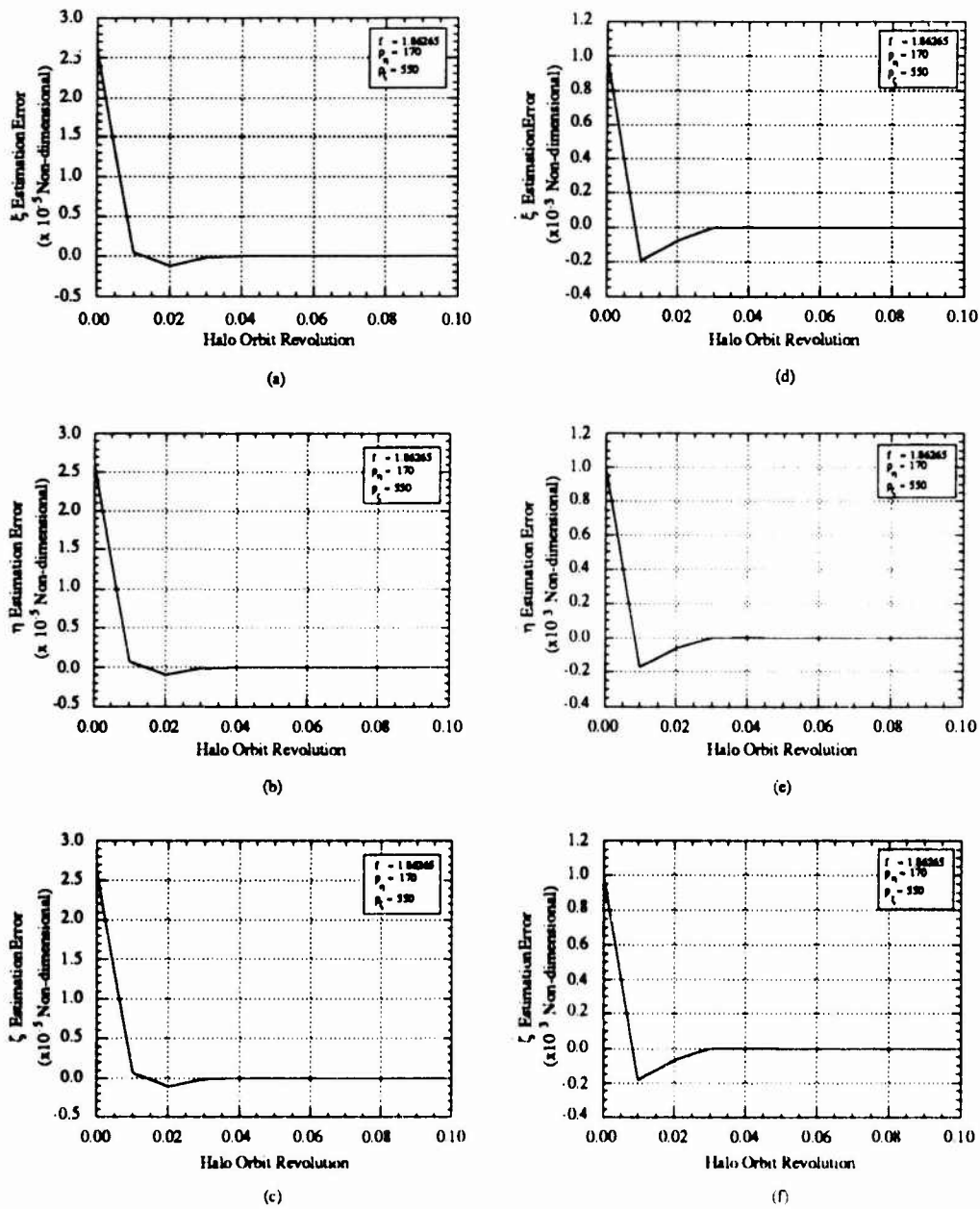
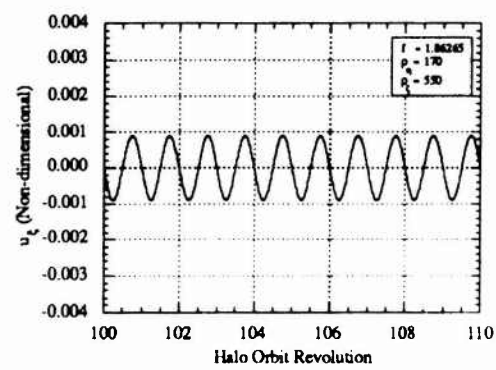
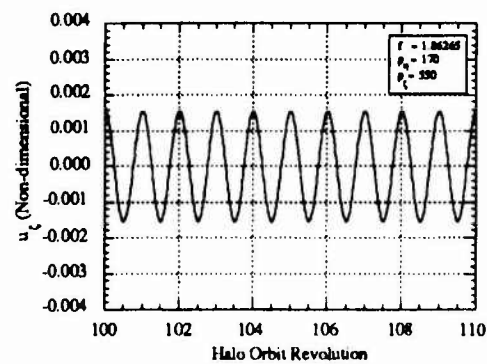


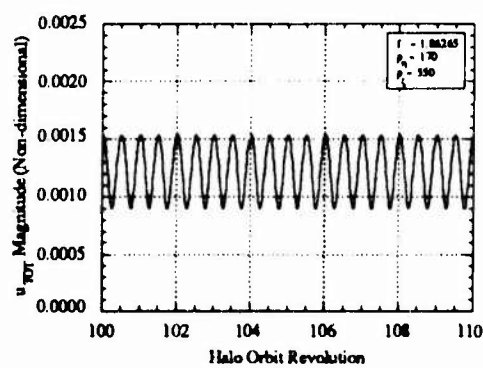
Figure B.2: Position and Velocity Estimation Error



(a)

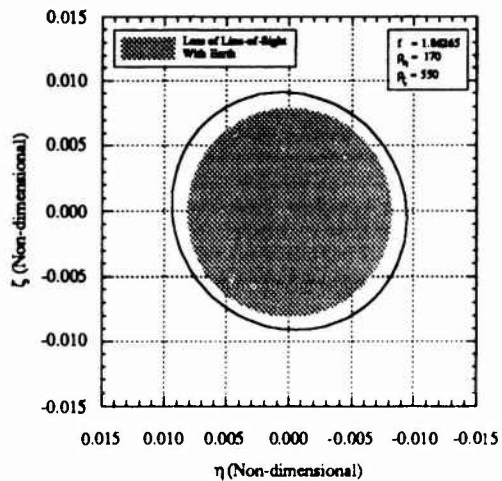


(b)



(c)

Figure B.3: Steady State Control Acceleration



(a) No Process Noise, No Measurement Noise

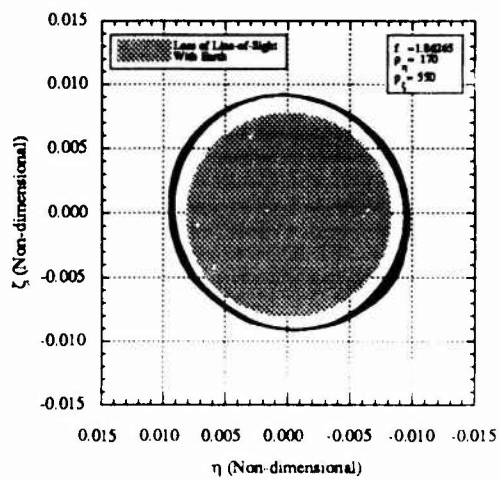
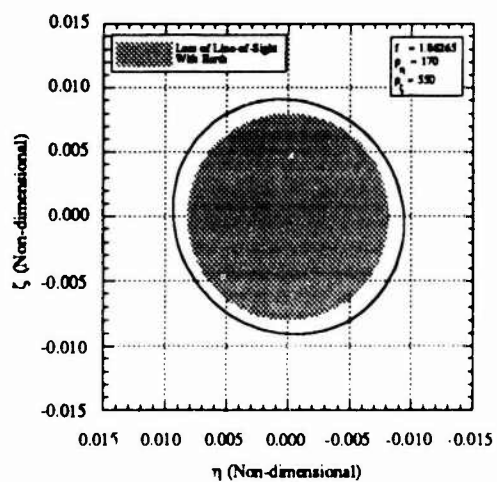
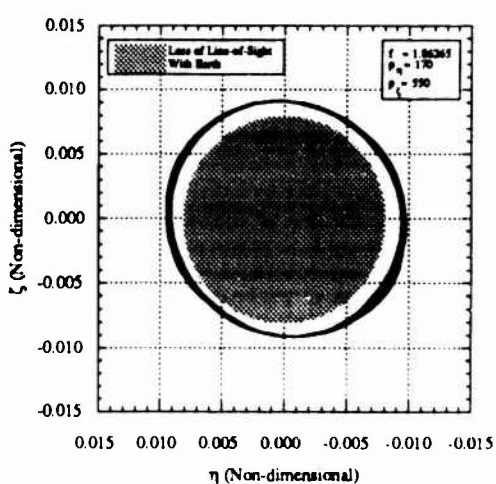
(c)  $3\sigma$  Process Noise, No Measurement Noise(b) No Process Noise,  $3\sigma$  Measurement Noise(d)  $3\sigma$  Process Noise,  $3\sigma$  Measurement Noise

Figure B.4: Halo Orbit Geometry as a Function of Noise

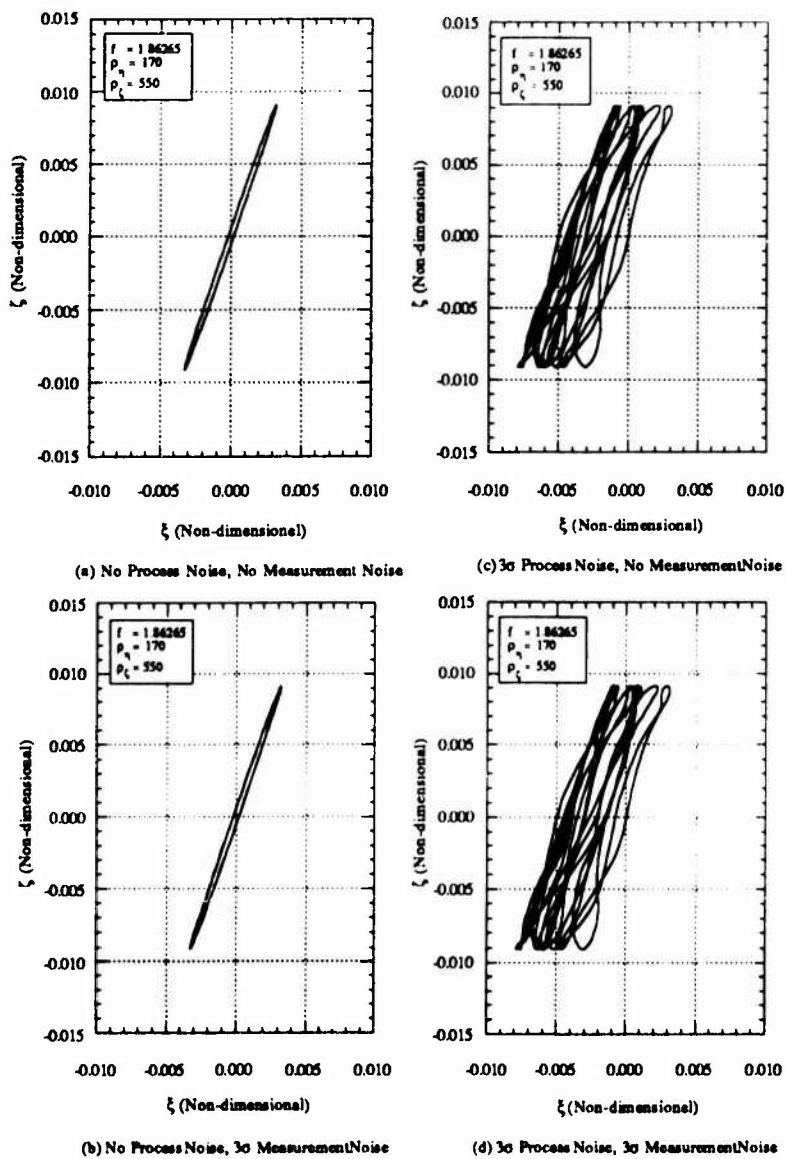
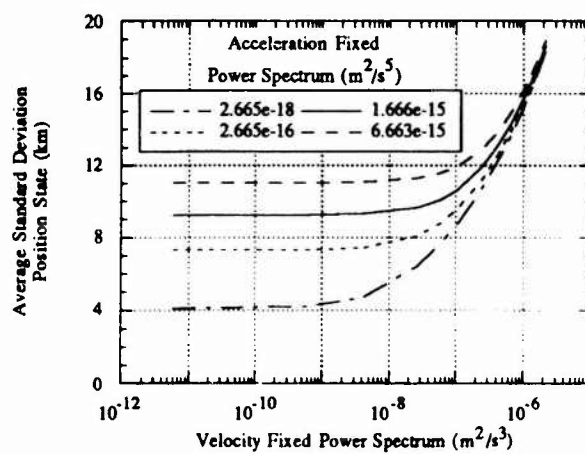
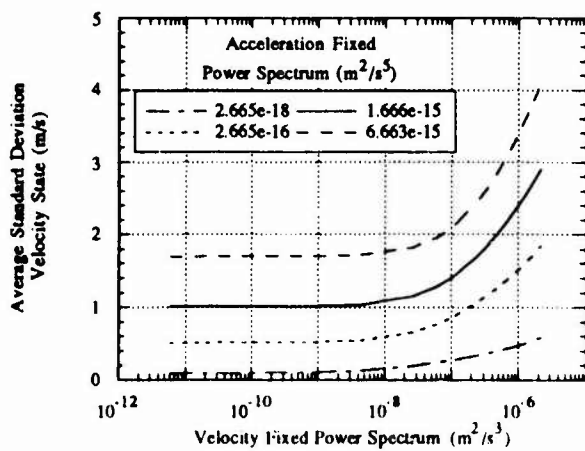


Figure B.5: Halo Orbit Orientation as a Function of Noise



(a)



(b)

Figure B.6: Noise Statistics



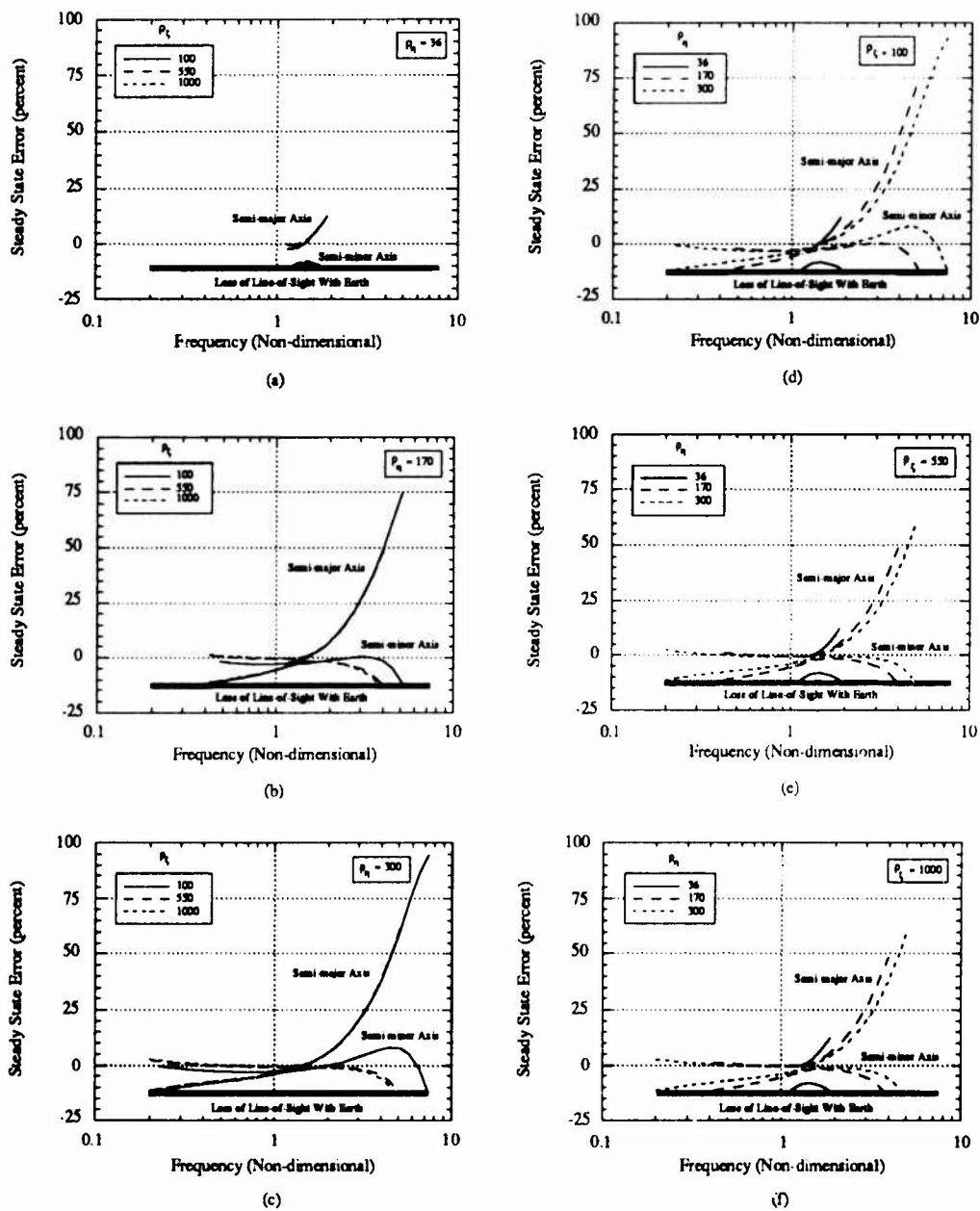


Figure B.7: Halo Orbit Geometry as a Function of Frequency

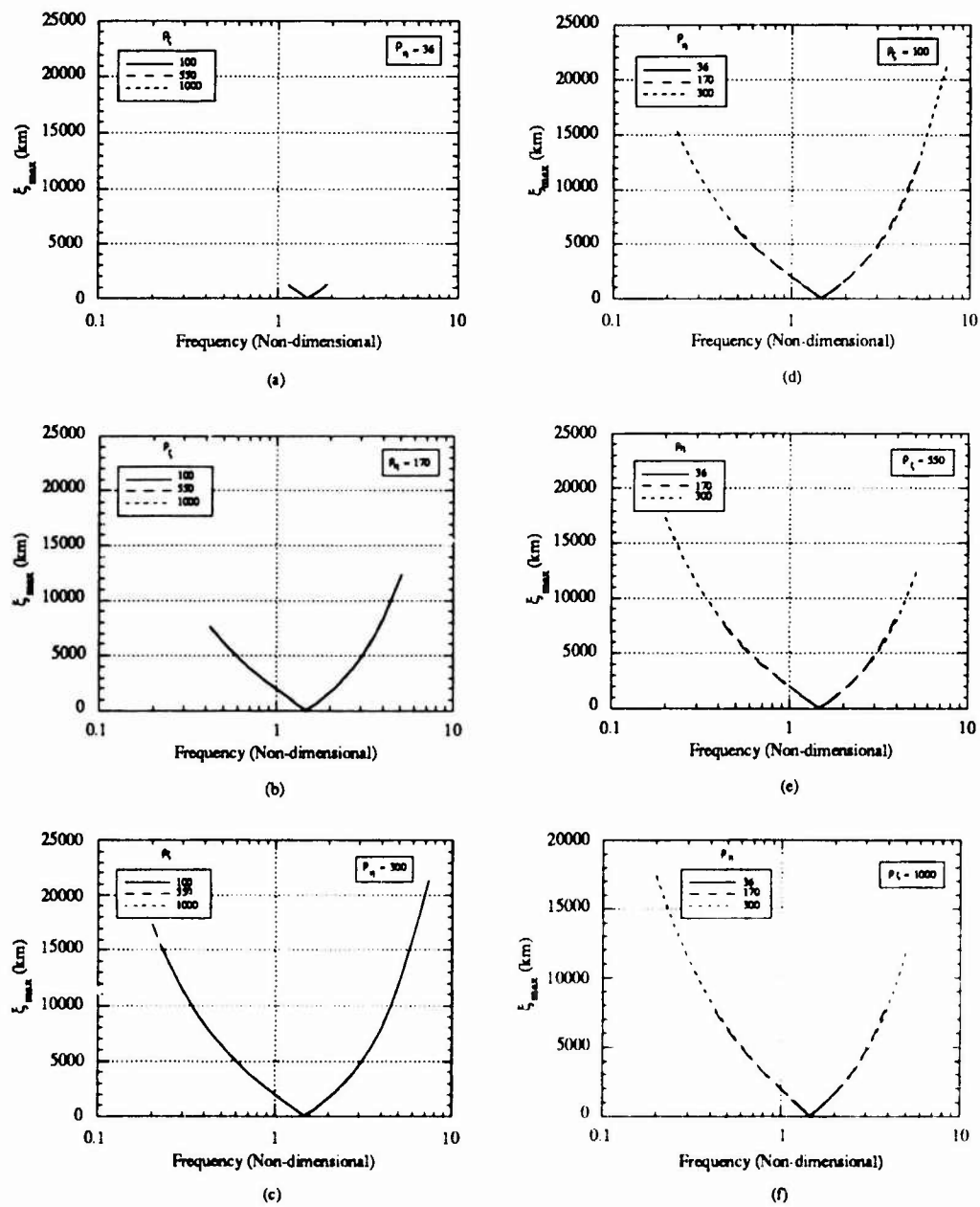
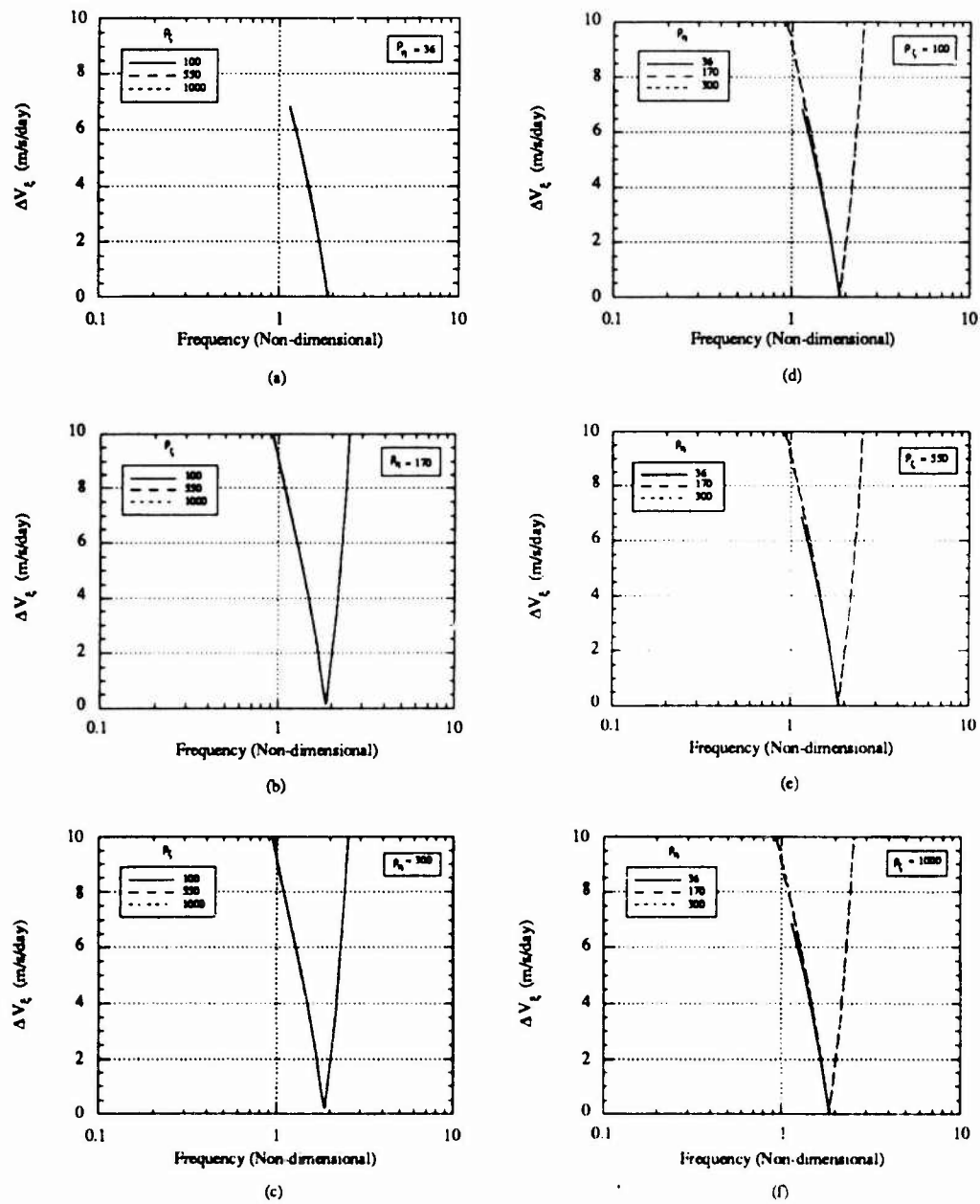
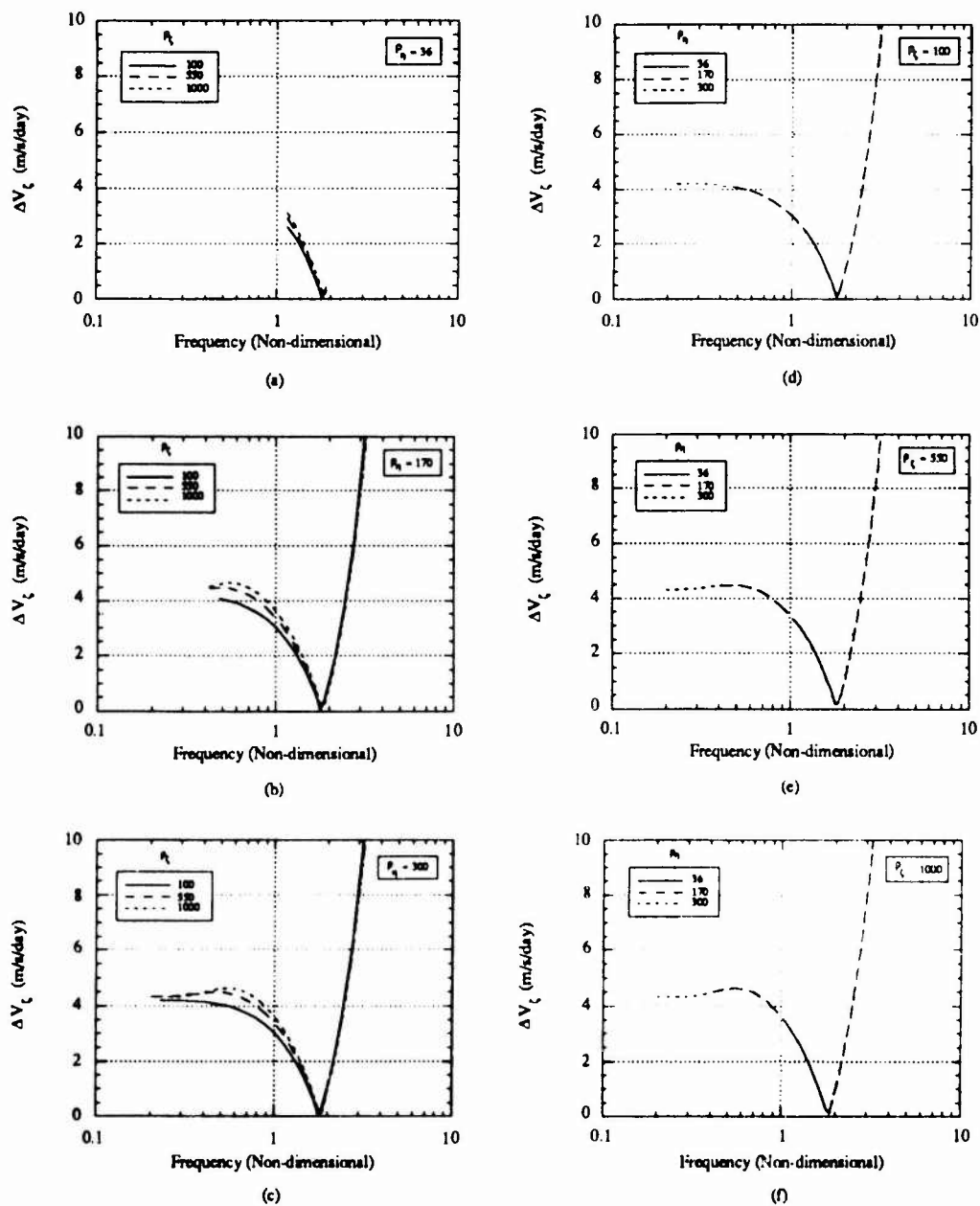


Figure B.8: Halo Orbit Orientation as a Function of Frequency

Figure B.9: Velocity Required in the  $\xi$  Axis

Figure B.10: Velocity Required in the  $\zeta$ -Axis

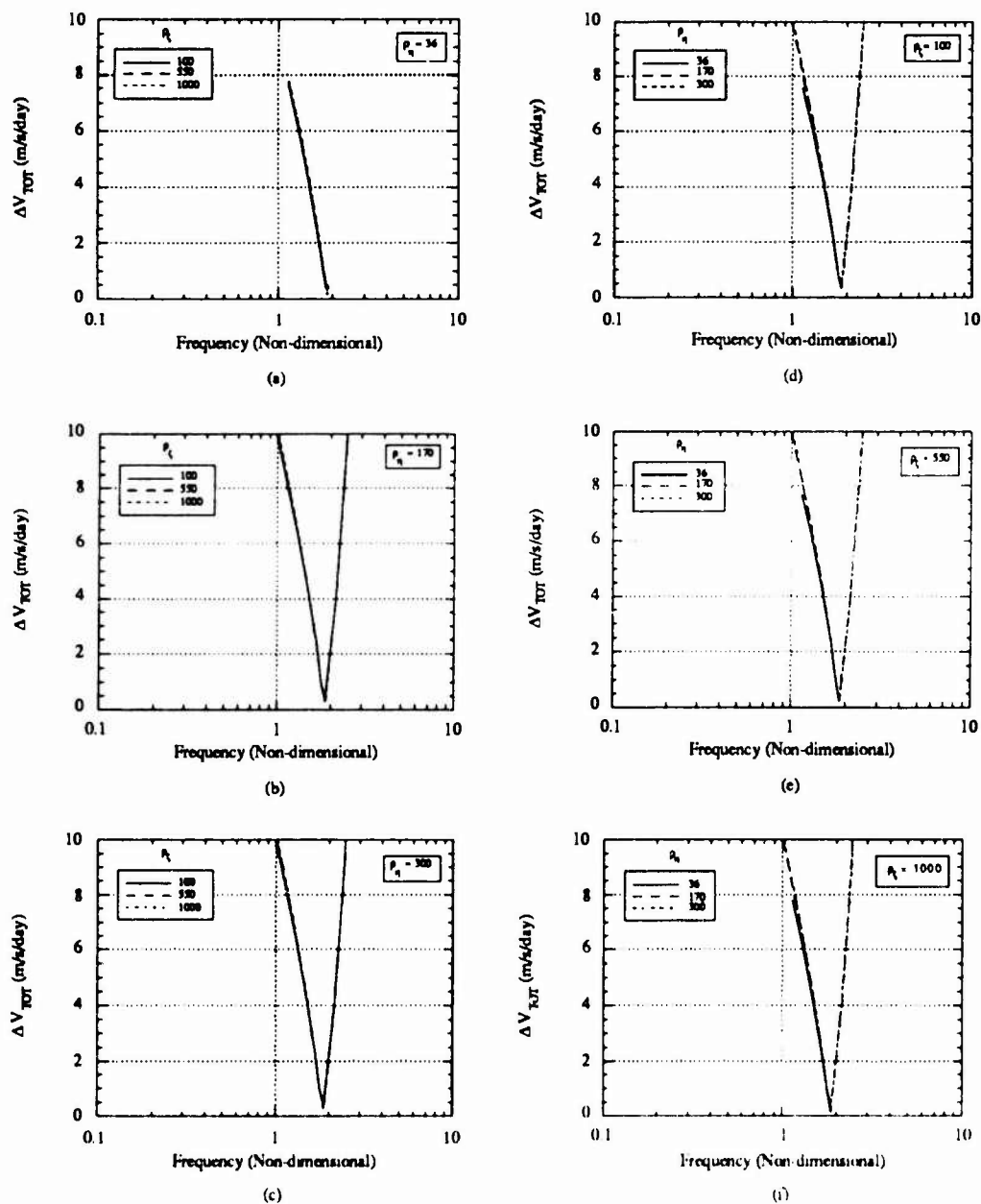
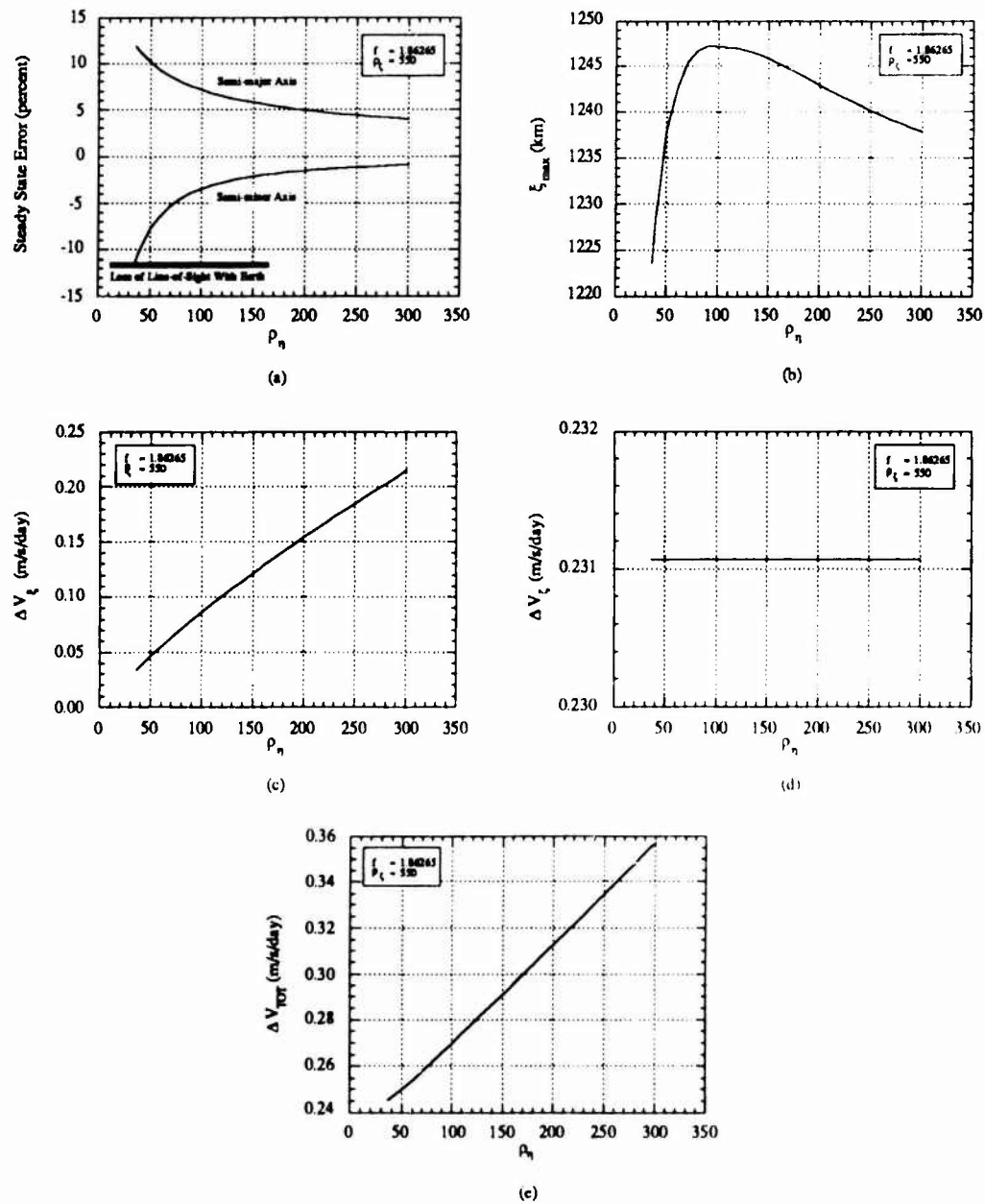
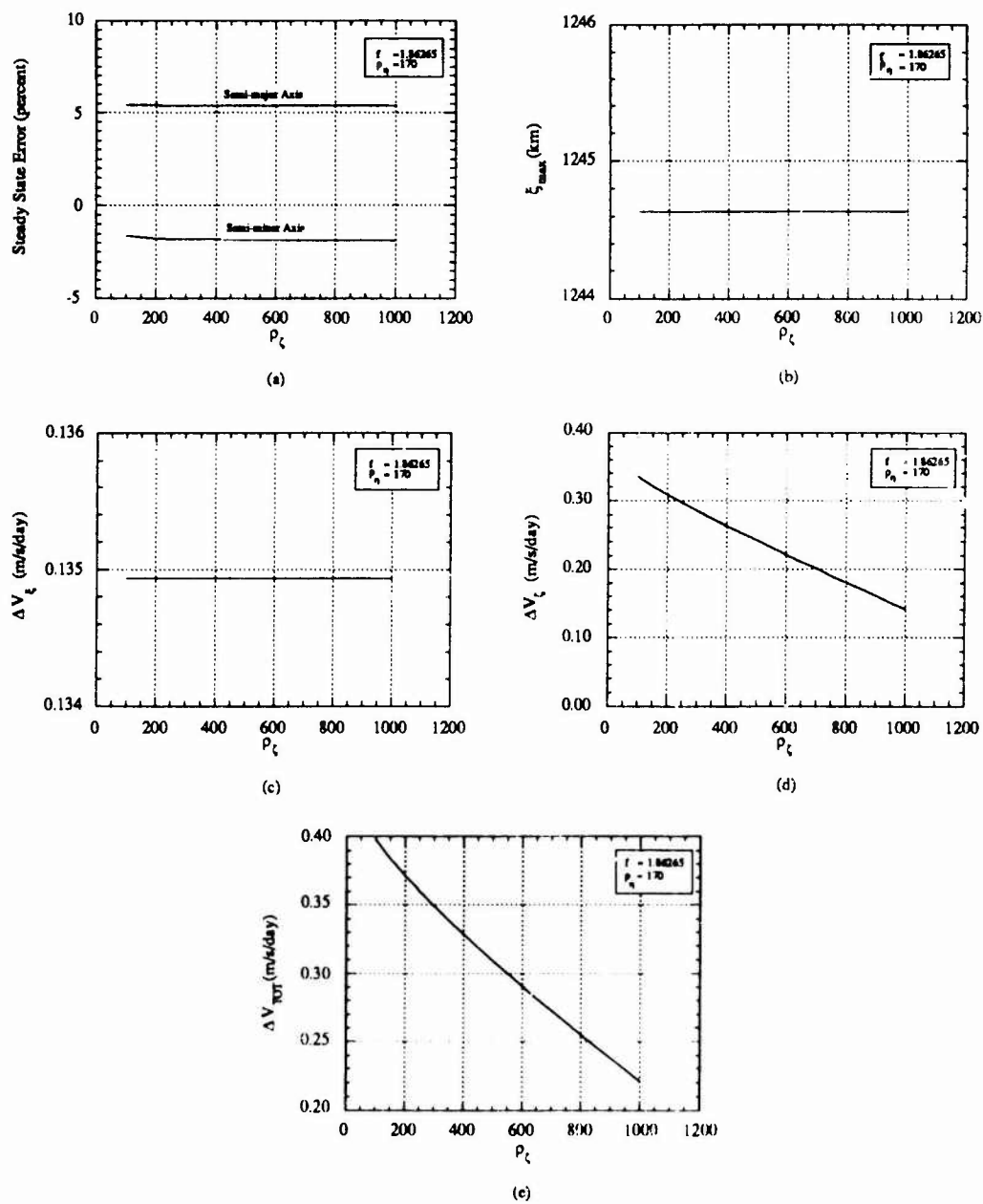


Figure B.11: Total Velocity Required

Figure B.12:  $\rho_n$  Parametric Study

Figure B.13:  $\rho_\zeta$  Parametric Study

## **Appendix C**

### **Rendezvous Navigation Filter Monte Carlo Data**

#### **C.1 Individual Error Vector Plots**

Figures C.1 - C.13 show the estimation error (solid line) from the rendezvous navigation filter of the chaser vehicle's inertial state for each of the 13 errors vectors selected. Range and line-of-sight angle measurements were incorporated into the rendezvous navigation filter once every minute. In these plots, (a-c) apply to the position estimation error while (d-f) apply to the velocity estimation error. The  $1\sigma$  standard deviation of the state (dotted lines) are also included on the plots.

#### **C.2 Sensitivity Matrix Data**

Figures C.14 - C.16 show the time histories of the individual elements of the sensitivity matrix. These figures apply to changes in downtrack, out-of-plane and radial velocity, respectively.



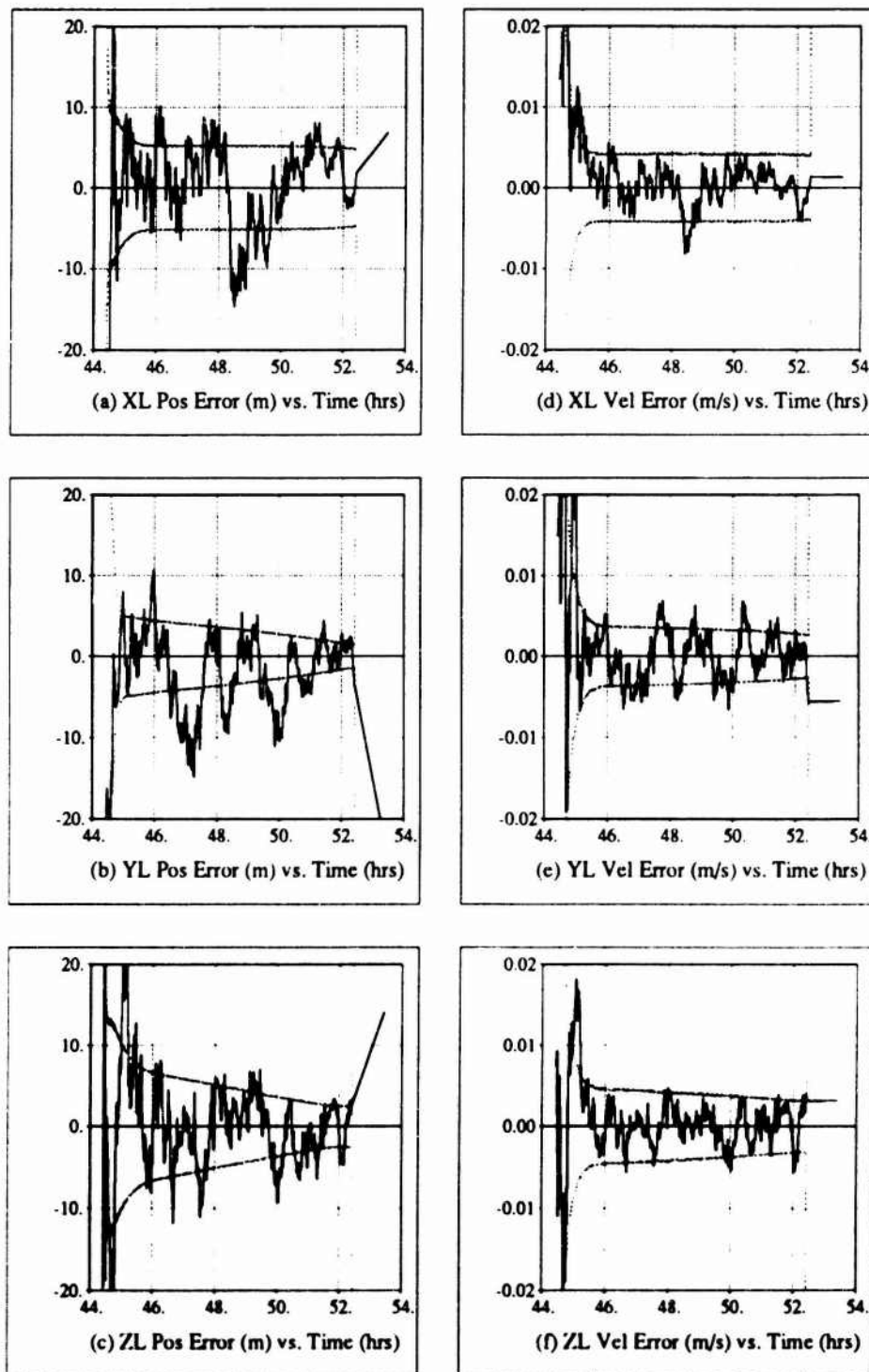


Figure C.1: Chaser Vehicle State Estimation Error (Error Vector 1)

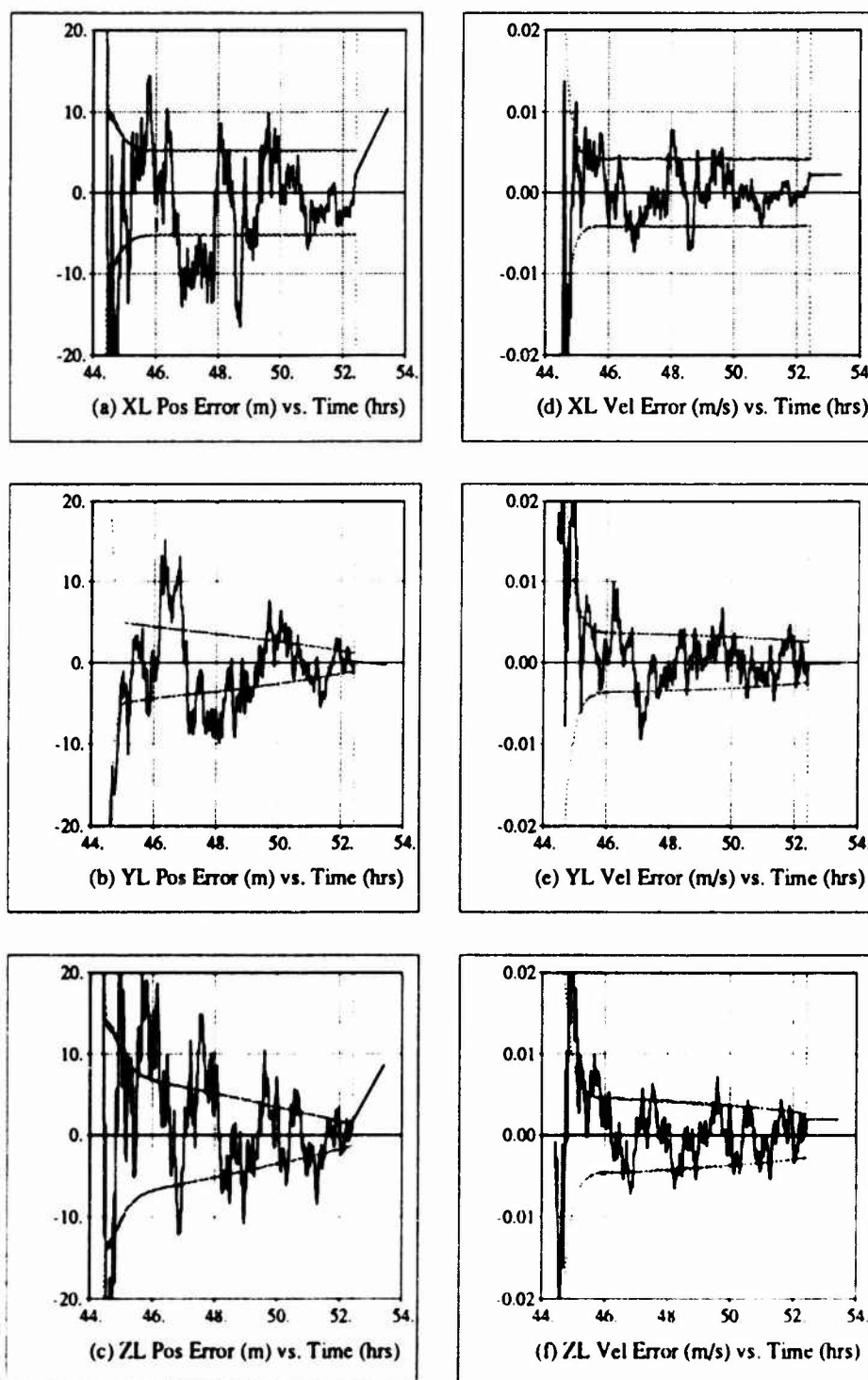


Figure C.2: Chaser Vehicle State Estimation Error (Error Vector 2)

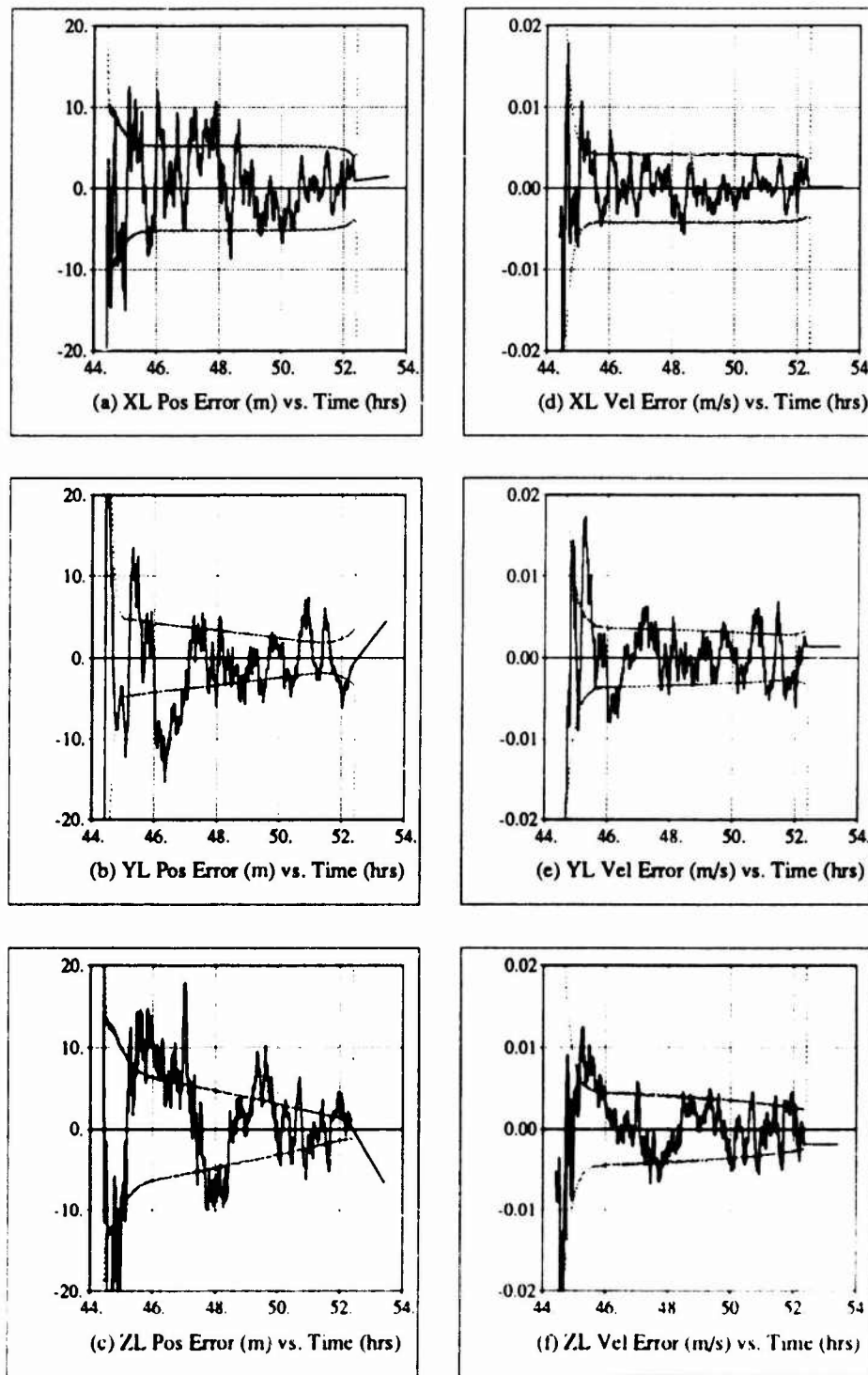


Figure C.3: Chaser Vehicle State Estimation Error (Error Vector 3)

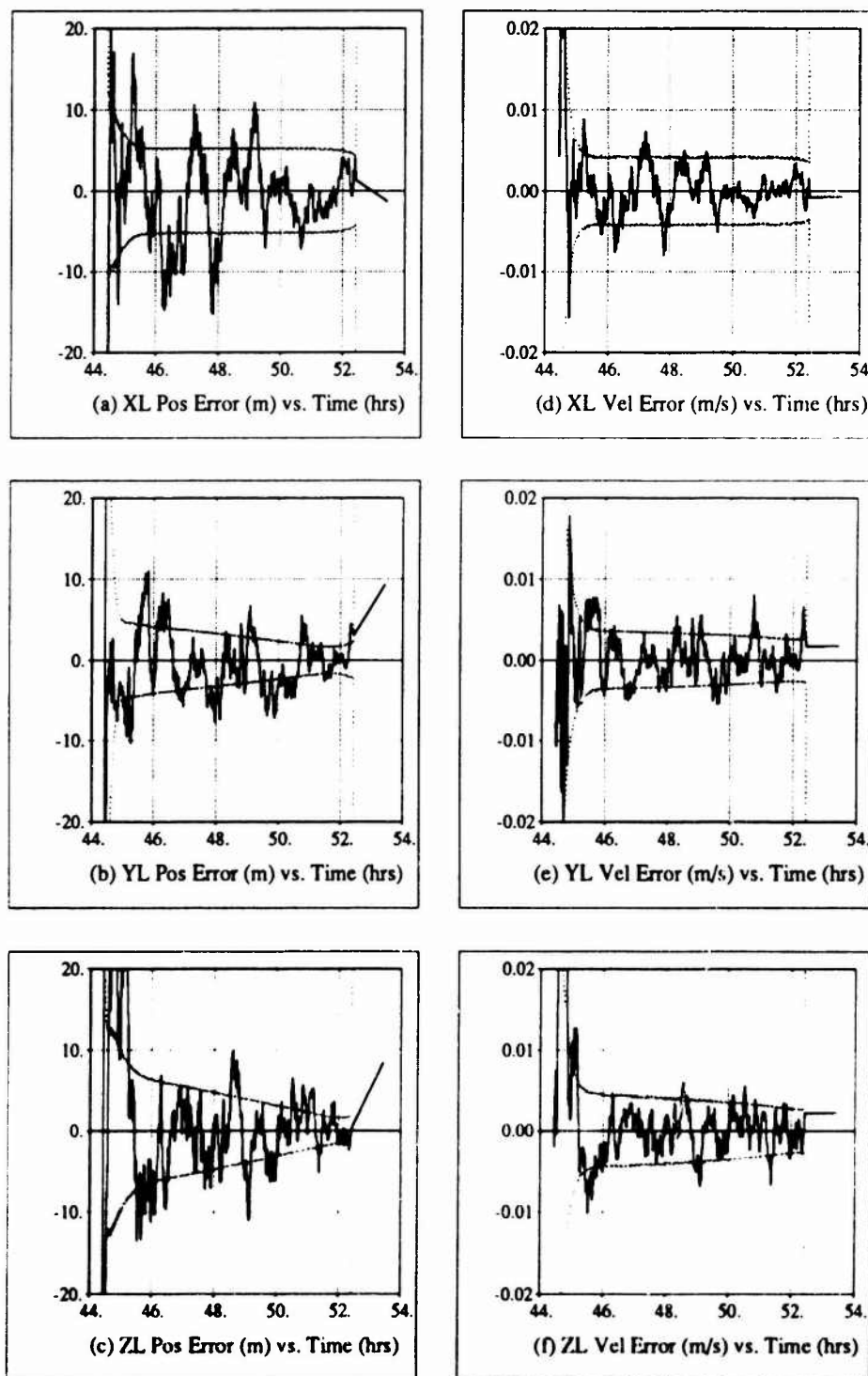


Figure C.4: Chaser Vehicle State Estimation Error (Error Vector 4)

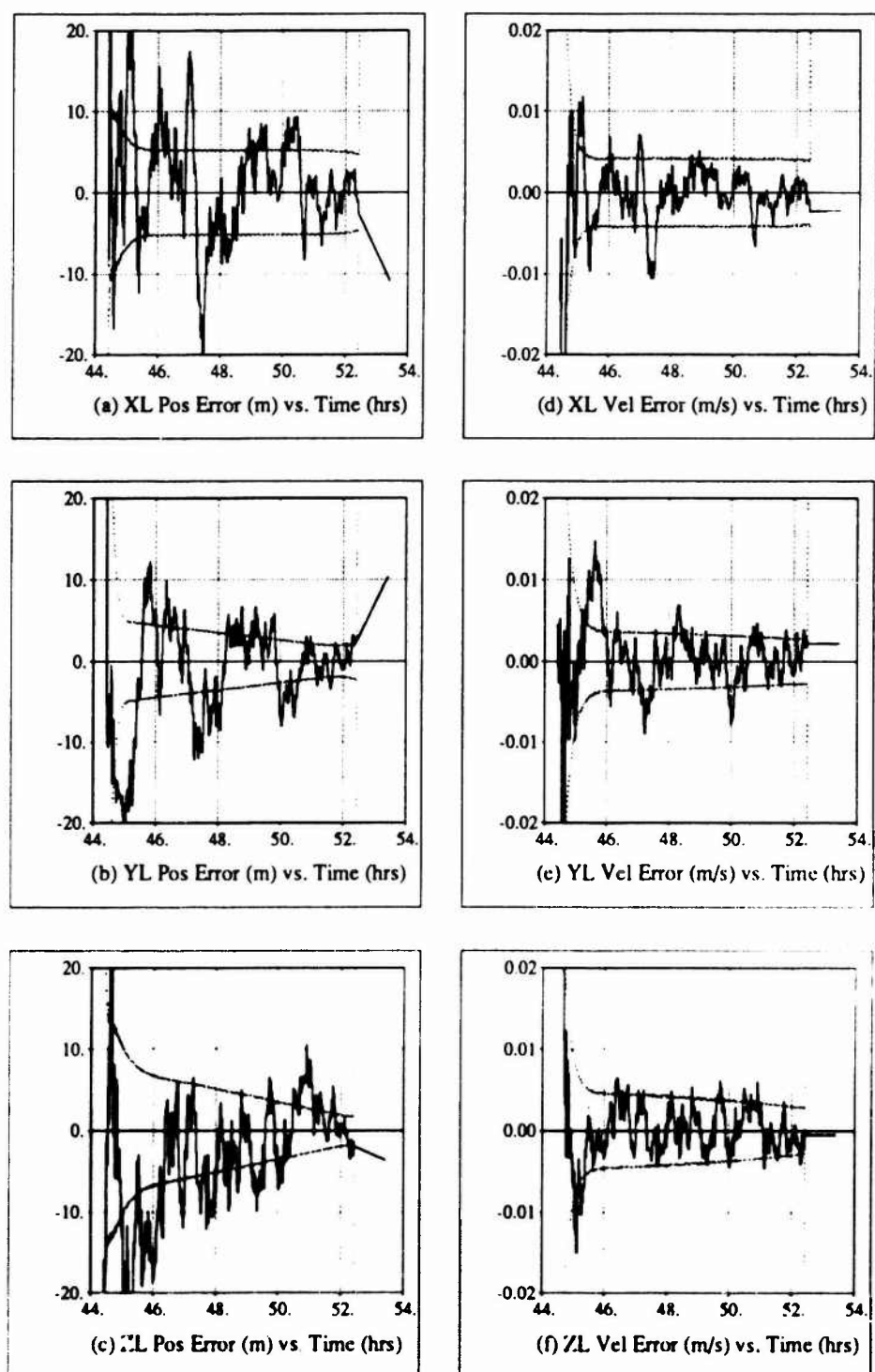


Figure C.5: Chaser Vehicle State Estimation Error (Error Vector 5)

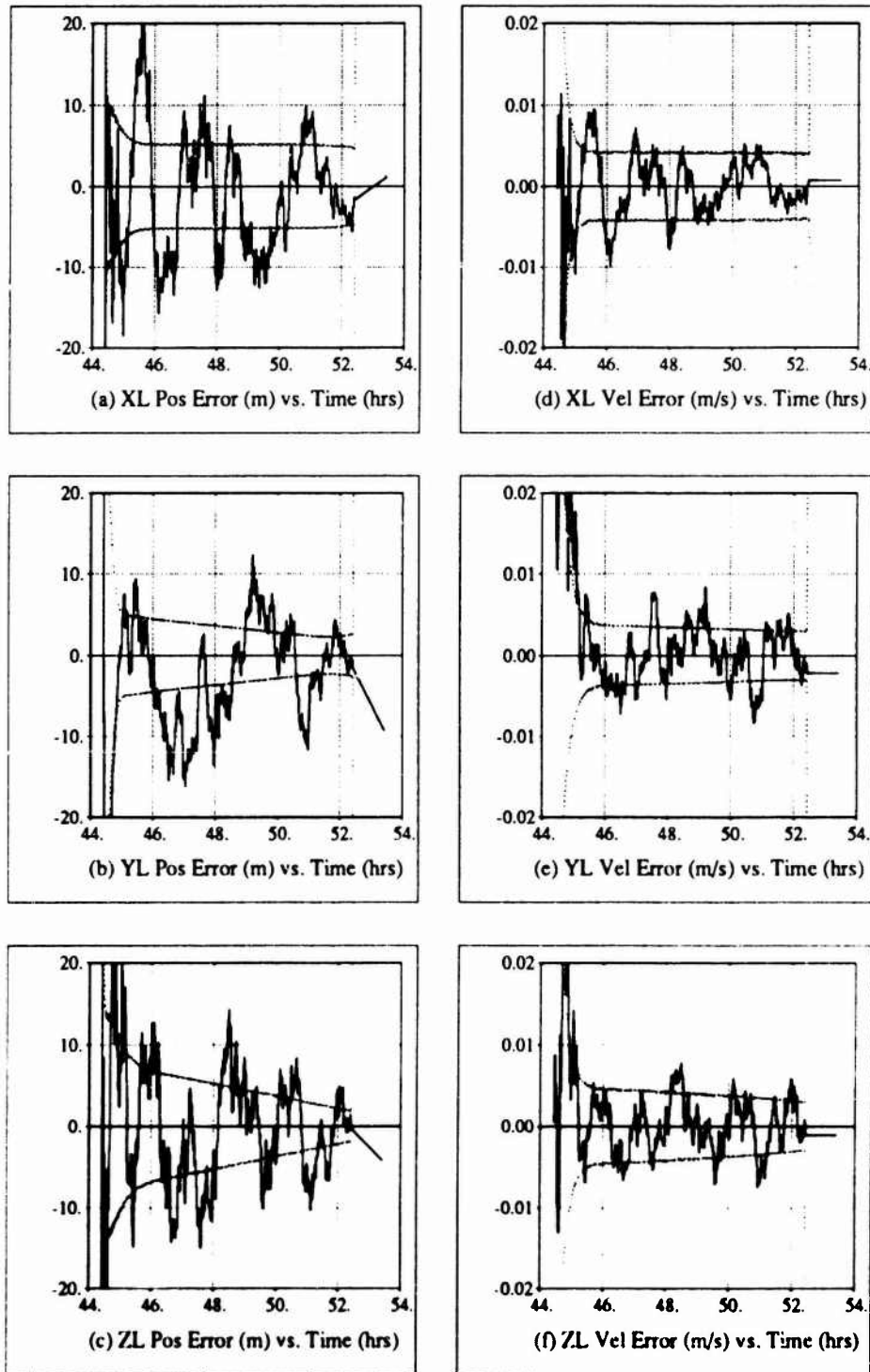


Figure C.6: Chaser Vehicle State Estimation Error (Error Vector 6)

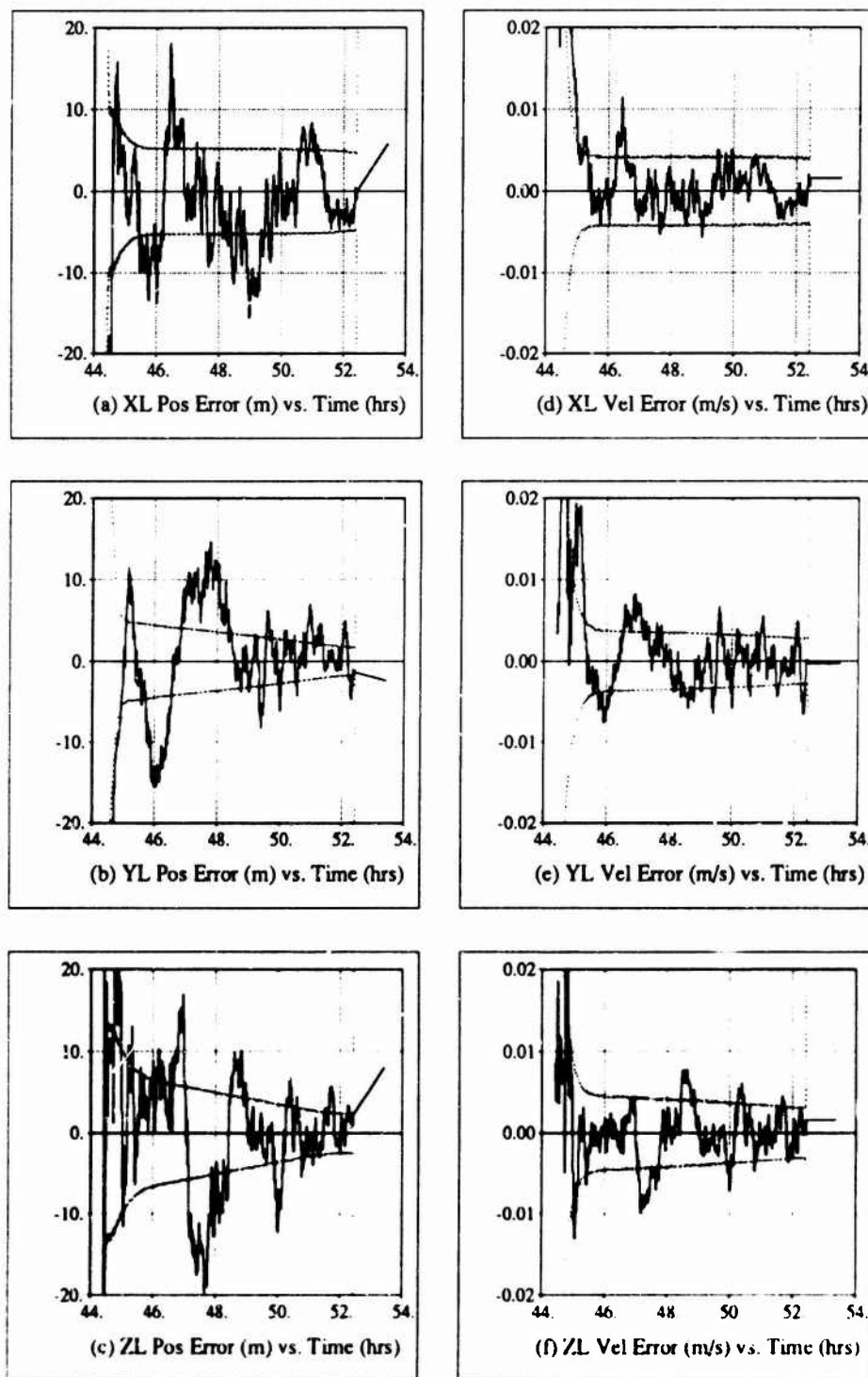


Figure C.7: Chaser Vehicle State Estimation Error (Error Vector 7)

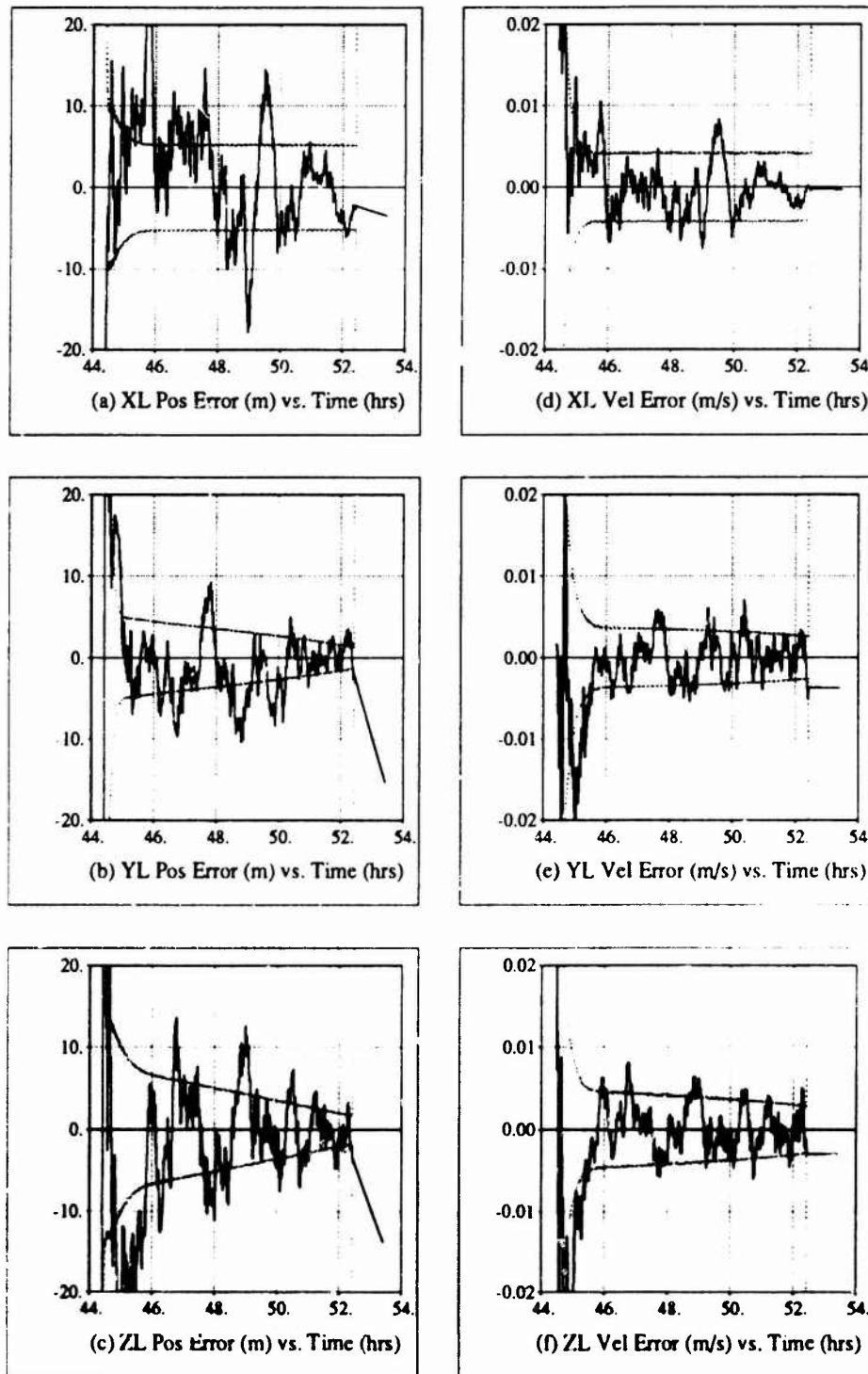


Figure C.8: Chaser Vehicle State Estimation Error (Error Vector 8)



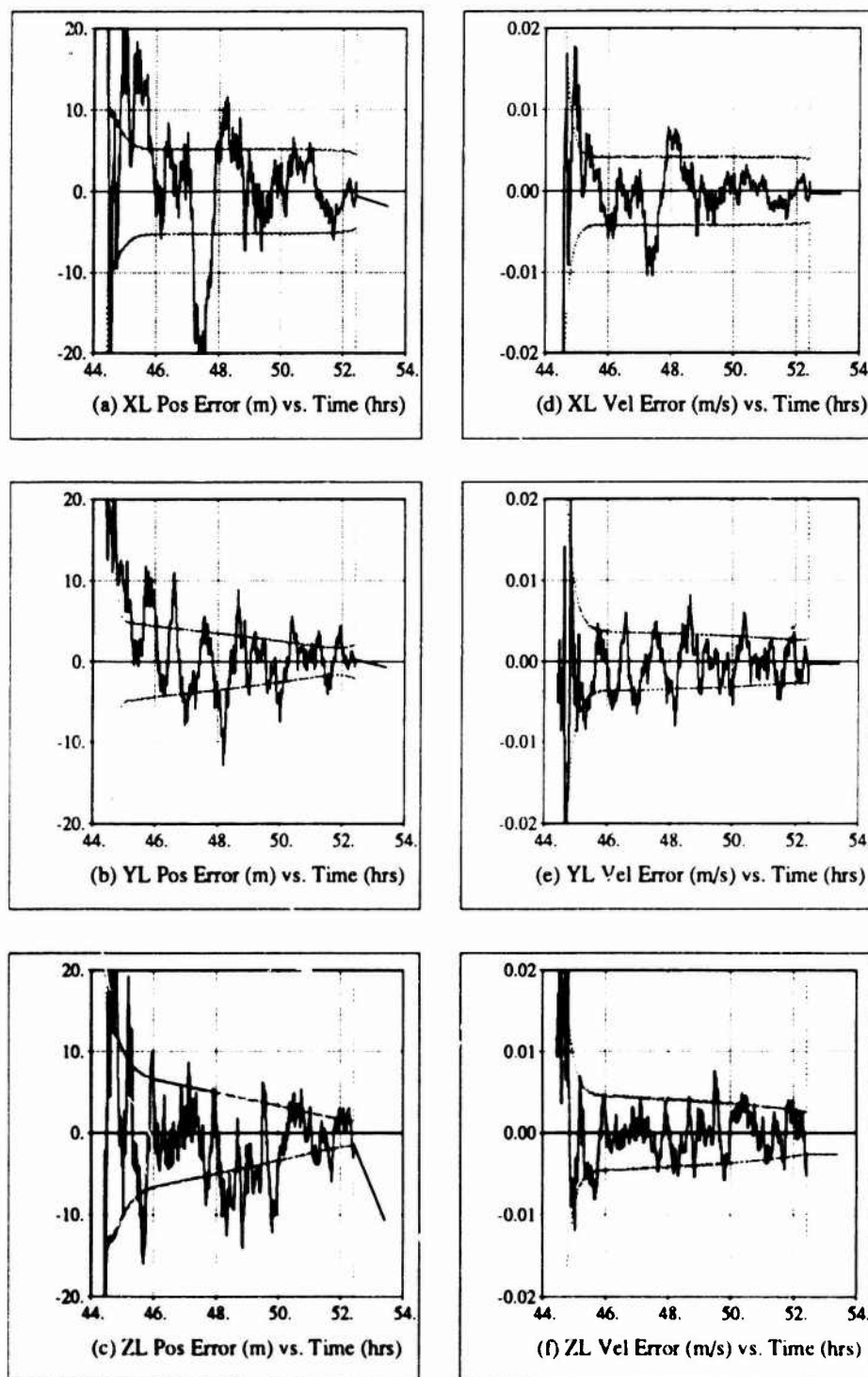


Figure C.9: Chaser Vehicle State Estimation Error (Error Vector 9)

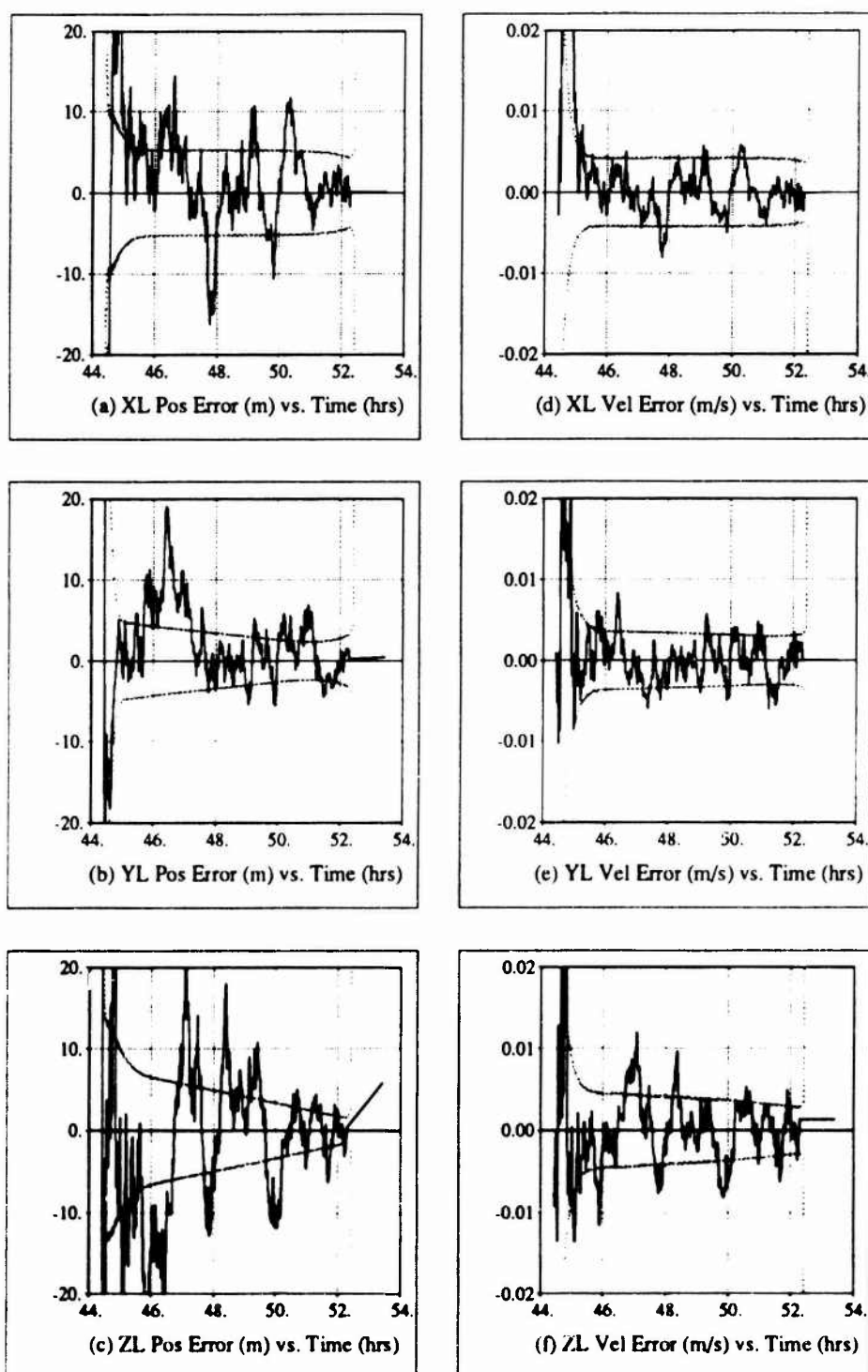


Figure C.10: Chaser Vehicle State Estimation Error (Error Vector 10)

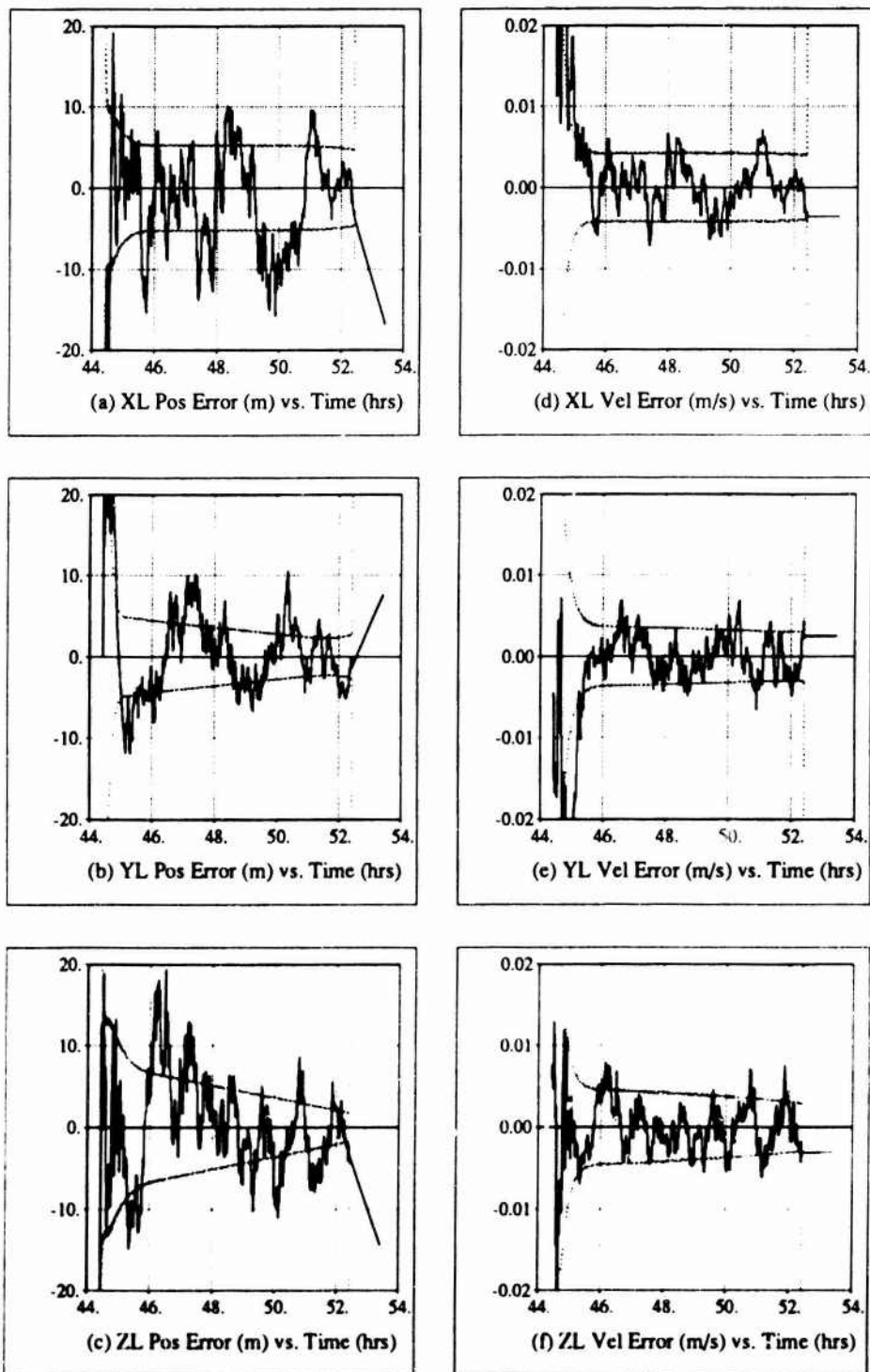


Figure C.11: Chaser Vehicle State Estimation Error (Error Vector 11)

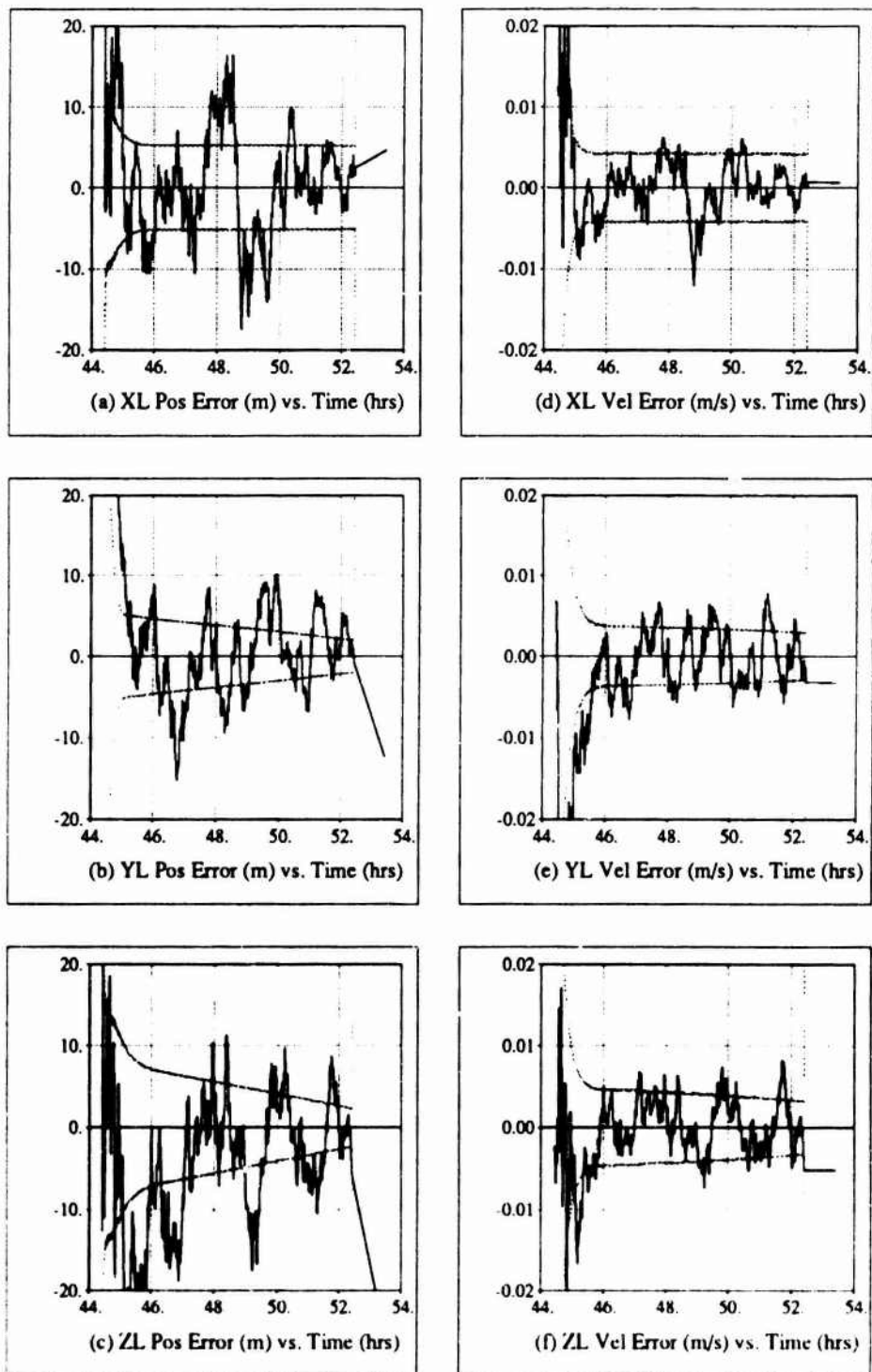


Figure C.12: Chaser Vehicle State Estimation Error (Error Vector 12)

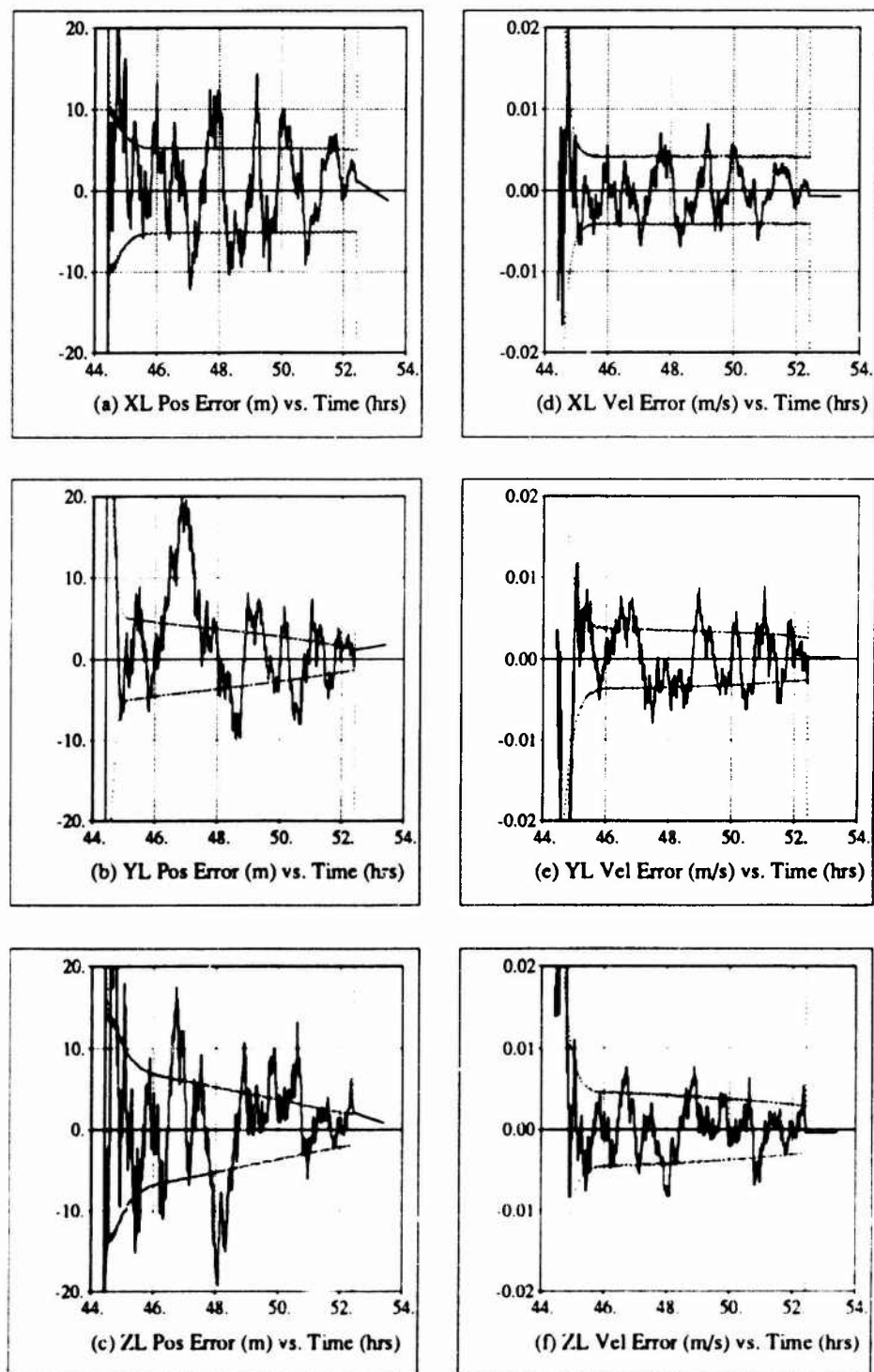


Figure C.13: Chaser Vehicle State Estimation Error (Error Vector 13)

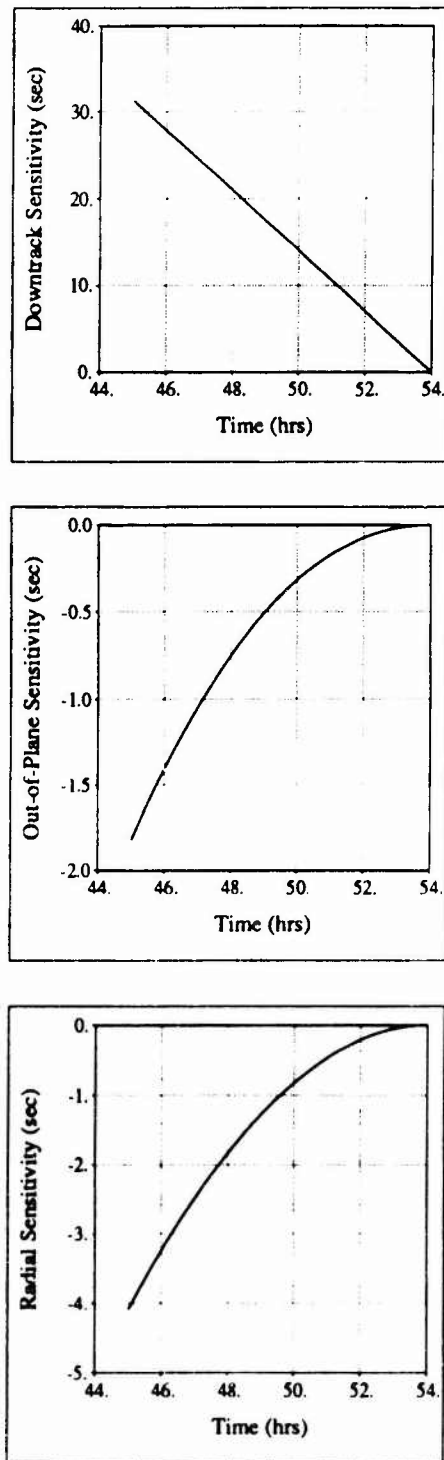


Figure C.14: Final Position Error Sensitivity to a Change in Downtrack Velocity

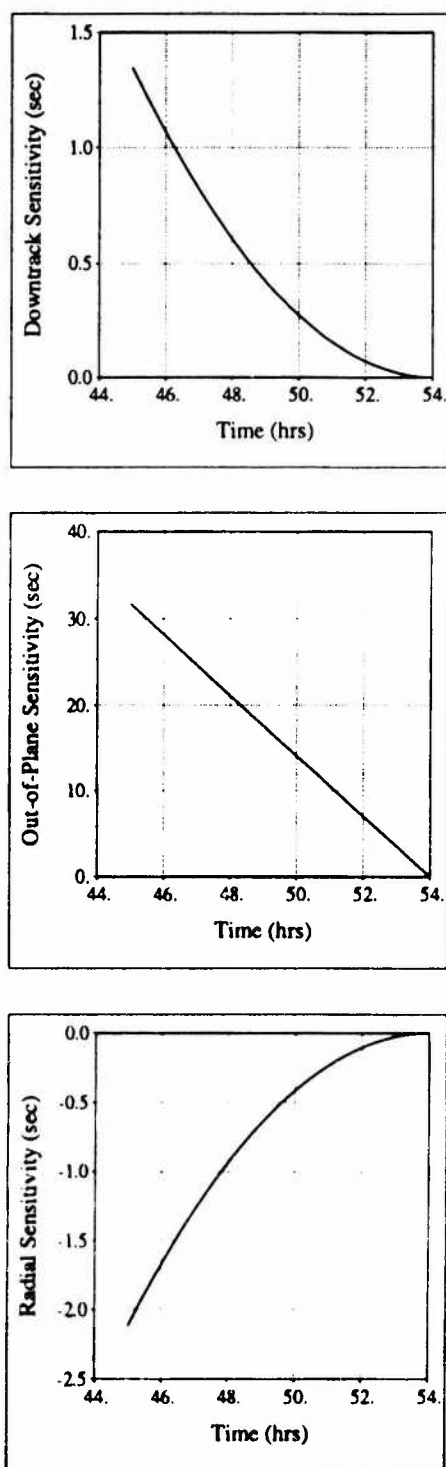


Figure C.15: Final Position Error Sensitivity to a Change in Out-of-Plane Velocity

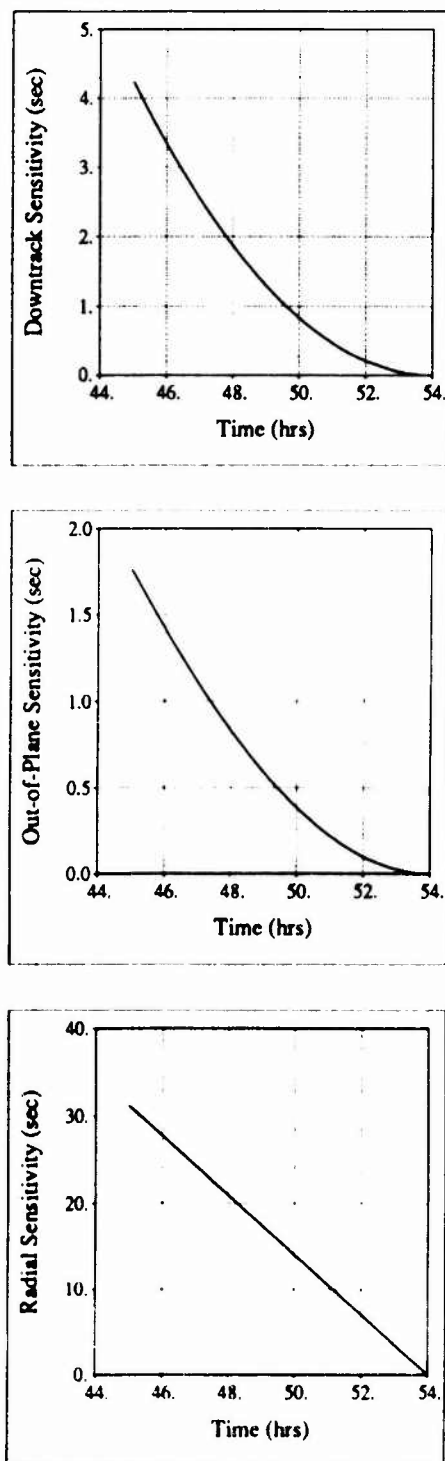


Figure C.16: Final Position Error Sensitivity to a Change in Radial Velocity



## Appendix D

### Applications Monte Carlo Data

#### D.1 Planar Circular Orbit (Profile 1)

Table D.1 summarizes the propulsion requirements for the individual simulations of the planar circular orbit for profile 1. Table D.2 gives the final miss distance data for these same simulations.

#### D.2 Planar Circular Orbit (Profile 2)

Table D.3 summarizes the propulsion requirements for the individual simulations of the planar circular orbit for profile 2. Table D.4 gives the final miss distance data for these same simulations.

#### D.3 $\mathcal{H}_2$ Guided Halo Orbit (Profile 1)

Table D.5 summarizes the propulsion requirements for the individual simulations of the  $\mathcal{H}_2$  guided halo orbit for profile 1. Table D.6 gives the final miss distance data for these same simulations.

#### D.4 $\mathcal{H}_2$ Guided Halo Orbit (Profile 2)

Table D.7 summarizes the propulsion requirements for the individual simulations of the  $\mathcal{H}_2$  guided halo orbit for profile 2. Table D.8 gives the final miss distance data for these same simulations.

Table D.1: Planar Circular Orbit Propulsion Requirement (IC=46.08 deg, INC=22.85 deg, TT=9 hrs)

Error Vector	Rendezvous Maneuver (m/s)						RCS	
	<i>TI</i>	<i>MCC1</i>	<i>MCC2</i>	<i>MCC3</i>	<i>MCC4</i>	<i>TF</i>	Total	Fuel (lbs)
Reference	0.686	0.000	0.000	0.000	0.000	0.491	1.177	5.776
1	0.686	0.032	0.009	0.016	0.018	0.487	1.247	6.119
2	0.686	0.016	0.003	0.014	0.017	0.500	1.236	6.065
3	0.686	0.055	0.006	0.010	0.017	0.454	1.228	6.026
4	0.686	0.046	0.008	0.009	0.005	0.453	1.207	5.923
5	0.686	0.036	0.013	0.013	0.021	0.504	1.272	6.242
6	0.686	0.066	0.014	0.012	0.010	0.523	1.310	6.428
7	0.686	0.033	0.018	0.010	0.006	0.477	1.230	6.036
8	0.686	0.013	0.010	0.014	0.022	0.478	1.223	6.001
9	0.686	0.039	0.002	0.007	0.016	0.492	1.242	6.094
10	0.686	0.056	0.018	0.005	0.014	0.490	1.268	6.222
11	0.686	0.047	0.009	0.007	0.008	0.496	1.252	6.143
12	0.686	0.072	0.006	0.010	0.011	0.554	1.339	6.570
13	0.686	0.018	0.012	0.007	0.019	0.504	1.246	6.114
Average Magnitude	0.686	0.041	0.010	0.010	0.014	0.493	1.254	6.153

Table D.2: Planar Circular Orbit Final Miss Distance (IC=46.08 deg, INC=22.85 deg, TT=9 hrs)

Error Vector	Final Miss Distance (m)			
	Downtrack	Out-of-Plane	Radial	Total
Reference	0.000	-0.001	0.000	0.001
1	2.615	14.744	-3.113	15.295
2	-12.508	-2.864	-9.094	15.728
3	-3.617	-13.090	-6.687	15.138
4	-5.347	2.661	-12.409	13.771
5	9.999	-5.066	8.739	14.213
6	2.108	-4.856	-5.405	7.566
7	-3.099	-6.349	-13.804	15.507
8	-0.730	9.458	9.759	13.610
9	-0.977	-7.665	-4.359	8.872
10	10.051	-0.343	-2.663	10.403
11	4.840	-5.942	8.540	11.171
12	-3.581	9.121	3.776	10.502
13	4.469	11.498	2.437	12.574
Average Magnitude	4.919	7.204	6.983	12.666

Table D.3: Planar Circular Orbit Propulsion Requirements (IC=180.00 deg, INC=22.85 deg, TT=9 hrs)

Error Vector	Rendezvous Maneuver (m/s)						RCS	
	<i>TI</i>	<i>MCC1</i>	<i>MCC2</i>	<i>MCC3</i>	<i>MCC4</i>	<i>TF</i>	Total	Fuel (lbs)
Reference	0.680	0.000	0.000	0.000	0.000	0.643	1.322	6.487
1	0.680	0.035	0.005	0.008	0.010	0.610	1.348	6.614
2	0.680	0.009	0.008	0.010	0.017	0.649	1.372	6.732
3	0.680	0.058	0.013	0.007	0.013	0.665	1.435	7.041
4	0.680	0.042	0.011	0.009	0.020	0.662	1.423	6.982
5	0.680	0.036	0.012	0.004	0.009	0.640	1.381	6.776
6	0.680	0.060	0.007	0.012	0.023	0.634	1.415	6.943
7	0.680	0.039	0.009	0.005	0.013	0.622	1.368	6.712
8	0.680	0.014	0.006	0.003	0.012	0.632	1.346	6.605
9	0.680	0.038	0.010	0.011	0.006	0.628	1.372	6.732
10	0.680	0.059	0.004	0.007	0.020	0.650	1.420	6.968
11	0.680	0.049	0.009	0.008	0.013	0.611	1.370	6.722
12	0.680	0.073	0.010	0.005	0.012	0.619	1.399	6.865
13	0.680	0.019	0.007	0.015	0.014	0.616	1.350	6.624
Average								
Magnitude	0.680	0.041	0.009	0.008	0.014	0.634	1.384	6.791

Table D.4: Planar Circular Orbit Final Miss Distance (IC=180.00 deg, INC= 22.85 deg, TT=9 hrs)

Error Vector	Final Miss Distance (m)			
	Downtrack	Out-of-Plane	Radial	Total
Reference	0.000	0.000	-0.001	0.001
1	6.641	12.333	-2.685	14.262
2	-14.683	-8.169	-3.234	17.111
3	4.325	-4.754	8.704	10.820
4	-6.652	-3.291	-7.559	10.593
5	1.331	-12.208	7.675	14.481
6	13.045	14.898	-3.024	20.032
7	-12.729	-15.405	-1.809	20.065
8	4.467	2.851	6.503	8.389
9	-21.063	-15.329	-4.528	26.441
10	6.461	-5.222	-5.814	10.140
11	-5.767	-1.066	-9.905	11.511
12	-1.938	6.628	6.501	9.485
13	6.021	24.977	5.973	26.378
Average Magnitude	8.080	9.779	5.686	15.362

Table D.5:  $\mathcal{H}_2$  Guided Halo Orbit Propulsion Requirements (IC=46.08 deg, TT=9 hrs)

Error Vector	Rendezvous Maneuver (m/s)						RCS	
	<i>TI</i>	<i>MCC1</i>	<i>MCC2</i>	<i>MCC3</i>	<i>MCC4</i>	<i>TF</i>	Total	Fuel (lbs)
Reference	0.627	0.019	0.022	0.027	0.044	0.684	1.421	6.972
1	0.627	0.041	0.018	0.031	0.038	0.671	1.426	6.997
2	0.627	0.012	0.026	0.026	0.043	0.692	1.425	6.992
3	0.627	0.064	0.024	0.031	0.061	0.643	1.451	7.120
4	0.627	0.038	0.019	0.032	0.045	0.637	1.398	6.860
5	0.627	0.028	0.018	0.032	0.040	0.686	1.432	7.026
6	0.627	0.061	0.035	0.031	0.036	0.690	1.480	7.262
7	0.627	0.041	0.035	0.032	0.046	0.670	1.452	7.125
8	0.627	0.034	0.018	0.029	0.049	0.677	1.434	7.036
9	0.627	0.023	0.023	0.035	0.038	0.666	1.412	6.928
10	0.627	0.039	0.023	0.030	0.030	0.649	1.398	6.860
11	0.627	0.040	0.022	0.035	0.033	0.667	1.424	6.987
12	0.627	0.074	0.026	0.026	0.061	0.748	1.562	7.664
13	0.627	0.033	0.016	0.040	0.027	0.700	1.443	7.080
Average Magnitude	0.627	0.041	0.023	0.032	0.042	0.677	1.441	7.071

Table D.6:  $\mathcal{H}_2$  Guided Halo Orbit Final Miss Distance ( $IC=46.08$  deg,  $TT=9$  hrs)

Error Vector	Final Miss Distance (m)			
	Downtrack	Out-of-Plane	Radial	Total
Reference	-7.673	19.394	0.124	20.857
1	-10.865	26.681	3.703	29.046
2	-15.263	12.383	22.215	29.662
3	-11.777	10.377	-25.045	29.558
4	-7.798	4.792	17.163	19.451
5	-2.458	9.457	-3.898	10.520
6	4.001	32.472	-4.514	33.027
7	-10.714	20.000	-9.875	24.745
8	-9.348	8.864	4.978	13.811
9	-5.351	24.825	-4.748	25.835
10	-21.348	31.346	-1.280	37.947
11	-5.276	36.849	8.084	38.093
12	-1.354	24.097	10.064	26.149
13	-13.530	12.465	-5.375	19.166
Average Magnitude	9.160	19.585	9.303	25.924

Table D.7:  $\mathcal{H}_2$  Guided Halo Orbit Propulsion Requirements (IC=180.00 deg, TT=9 hrs)

Error Vector	Rendezvous Maneuver (m/s)						RCS	
	<i>TI</i>	<i>MCC1</i>	<i>MCC2</i>	<i>MCC3</i>	<i>MCC4</i>	<i>TF</i>	Total	Fuel (lbs)
Reference	0.704	0.008	0.008	0.009	0.013	0.672	1.413	6.933
1	0.704	0.029	0.020	0.003	0.032	0.655	1.442	7.076
2	0.704	0.029	0.007	0.012	0.037	0.687	1.476	7.242
3	0.704	0.055	0.012	0.017	0.026	0.694	1.509	7.404
4	0.704	0.048	0.009	0.024	0.003	0.691	1.481	7.267
5	0.704	0.051	0.011	0.014	0.014	0.664	1.457	7.149
6	0.704	0.059	0.013	0.021	0.016	0.651	1.465	7.188
7	0.704	0.025	0.009	0.010	0.026	0.650	1.424	6.987
8	0.704	0.007	0.016	0.011	0.013	0.656	1.408	6.909
9	0.704	0.040	0.021	0.012	0.021	0.663	1.460	7.164
10	0.704	0.064	0.013	0.010	0.024	0.684	1.498	7.350
11	0.704	0.054	0.012	0.009	0.013	0.640	1.433	7.031
12	0.704	0.070	0.017	0.007	0.029	0.640	1.468	7.203
13	0.704	0.013	0.015	0.010	0.013	0.646	1.400	6.870
Average Magnitude	0.704	0.042	0.013	0.012	0.021	0.663	1.455	7.139



Table D.8:  $\mathcal{H}_2$  Guided Halo Orbit Final Miss Distance ( $IC=180.00$  deg,  $TT=9$  hrs)

Error Vector	Final Miss Distance (m)			
	Downtrack	Out-of-Plane	Radial	Total
Reference	-4.834	-3.191	-0.885	5.859
1	-2.708	-5.606	0.918	6.293
2	4.658	1.088	-2.222	5.274
3	-4.074	-11.543	0.630	12.257
4	5.344	3.019	-4.398	7.551
5	-7.830	-18.871	3.705	20.764
6	-4.654	2.036	7.515	9.070
7	-2.251	8.457	0.655	8.776
8	-12.955	-10.494	-1.436	16.734
9	6.421	-26.408	19.593	33.504
10	-13.834	-16.410	5.362	22.122
11	-1.925	-11.195	-14.518	18.434
12	-5.174	-3.076	3.882	7.162
13	-4.848	-14.685	0.639	15.478
Average Magnitude	5.898	10.222	5.036	14.109

## Bibliography

- [1] von Braun, W. and Ryan, C., "Can We Get to Mars?," Collier's Magazine, April 30, 1954, pp. 22-29.
- [2] "Report of the Advisory Committee On the Future of the U.S. Space Program," Washington, DC, December, 1990.
- [3] "Report of the 90-Day Study on Human Exploration of the Moon and Mars," NASA, November, 1989.
- [4] "America at the Threshold: Report of the Synthesis Group on America's Space Exploration Initiative," U.S. Government Printing Office, Washington, DC, May, 1991.
- [5] Bordano, A., et al, "Lunar Navigation Infrastructure (Concepts and Issues)," Presented at NASA Johnson Space Center, January 15, 1992.
- [6] Breakwell, J. V. and Brown, J. V., "The 'Halo' Family of 3-Dimensional Periodic Orbits in the Earth-Moon Restricted 3-Body Problem," *Celestial Mechanics*, Vol. 20, No. 4, November, 1979. pp.389-404.
- [7] Breakwell, J. V., Kamel, A. A., and Ratner, M. J., "Station-Keeping for a Translunar Communication Station," *Celestial Mechanics*, Vol. 10, No. 3, November, 1974, pp. 357-373.
- [8] Colombo, G., "The Stabilization of an Artificial Satellite at the Inferior Conjunction Point of the Earth-Moon System," Smithsonian Institution Astrophysical Observatory, SAO Special Report No. 80, September, 1961.

- [9] Dusek, H. M., "Motion in the Vicinity of Libration Points of a Generalized Restricted Three-Body Model," Presented at the AIAA/ION Astrodynamics Specialist Conference, AIAA Paper No. 65-682, Monterey, CA, September, 1965.
- [10] Euler, E. A. and Yu, E. Y., "Optimal Station-keeping at Collinear Points," Presented at the AIAA/AAS Astrodynamics Conference, AIAA Paper No. 69-906, Princeton, NJ, August, 1969.
- [11] Farquhar, R. W., "Station-keeping in the Vicinity of Collinear Libration Points with an Application to a Lunar Communications Problem," *AAS Science and Technology Series*, Vol. II, 1966, pp. 519-535.
- [12] Farquhar, R. W., "The Control and Use of Libration-Point Satellites", NASA TR-R-346, September, 1970.
- [13] Farquhar, R. W., "The Utilization of Halo Orbits in Advanced Lunar Operations", NASA TN-D-6365, July, 1971.
- [14] Farquhar, R. W., "A Halo-Orbit Lunar Station", *Astronautics and Aeronautics*, Vol. 10, No. 6, June, 1972, pp. 59-63.
- [15] Farquhar, R. W. and Kamel, A. A., "Quasi-Periodic Orbits About the Translunar Libration Point," *Celestial Mechanics*, Vol. 7, No. 4, June 1973, pp. 458-473.
- [16] Farquhar, R. W., Muhonen, D. P., and Richardson, D. L. "Mission Design for a Halo Orbiter of the Earth," *Journal of Spacecraft and Rockets*, Vol. 14, No. 3, March, 1977, pp. 170-177.
- [17] Fraietta, M. F. and Bond, V. R., "Libration Point Stationkeeping In The Earth-Moon System", McDonnell Douglas Space System Company.

- Houston, TX, TM-3.50.01-09, June, 1991. (see also "Station Keeping near the Unstable Libration Points of the Restricted Three-Body Problem", NASA-JSC-24597, October, 1990.)
- [18] Heppenheimer, T. A., "Optimal Controls for Out-of-Plane Motion about the Translunar Libration Point," *Journal of Spacecraft and Rockets*, Vol. 7, No. 9, September, 1970, pp. 1000-1092.
  - [19] Howell, K. C., "Three-Dimensional, Periodic, 'Halo' Orbits," *Celestial Mechanics*, Vol. 32, No. 1, January, 1984, pp. 53-71.
  - [20] Howell, K. C. and Breakwell, J. V., "Almost Rectilinear Halo Orbits," *Celestial Mechanics*, Vol. 32, No. 1, January, 1984, pp. 29-52.
  - [21] Howell, K. C. and Pernicka, H. J., "Numerical Determination of Lissajous Trajectories in the Restricted Three-Body Problem," *Celestial Mechanics*, Vol 41, No. 1-4, 1987/1988, pp. 107-124.
  - [22] Krasilnikow, P. S. and Kunitsyn, A. L., "On the Stabilization of the Collinear Libration Points of the Restricted Circular Three-Body Problem," *Celestial Mechanics*, Vol. 15, No. 1, February, 1977, pp. 41-51.
  - [23] Paul, E. W. and Shapiro, G., "Stabilization of the Lagrangian Solutions of the Three Body Problem," *Astronautica Acta*, Vol. 11, No. 6, 1965, pp. 410-417.
  - [24] Porter, J. D., "Final Report for Lunar Libration Point Flight Dynamics Study", NASA-CR-130135, April, 1969.
  - [25] Simó, C., Gómez, G., Llibre, J., Martínez, R., and Rodríguez, J., "On the Optimal Station Keeping Control of Halo Orbits," *Acta Astronautica*, Vol. 15, No. 6/7, 1987, pp. 391-397.

- [26] Vonbun, F. O., "A Hummingbird for the  $L_2$  Lunar Libration Point", NASA-TN-D-4468, April, 1968.
- [27] Bond, V. R., Sponaugle, S. J., Fraietta, M. F. and Everett, S. F., "Cislunar Libration Point as a Transportation Node for Lunar Exploration," Presented at the AAS/AIAA Spaceflight Mechanics Meeting, AAS Paper No. 91-103, Houston, TX, February, 1991.
- [28] Broucke, R., "Traveling Between the Lagrange Points and the Moon," *Journal of Guidance and Control*, Vol. 2, No. 4, July-August, 1979, pp. 257-263.
- [29] Edelbaum, T. N., "Libration Point Rendezvous," Analytical Mechanics Associates, Inc., Cambridge, MA, Report No. 70-12, February, 1970.
- [30] Korsmeyer, D. J., "Trajectory Determination and Characterization of Cislunar Low-Thrust Spacecraft," Presented at the Lunar Bases and Space Activities in the 21st Century Symposium, Houston, TX, April, 1988.
- [31] Marinescu, A., "Low-Thrust Maneuvers Near the Libration Points," *Journal of Guidance and Control*, Vol. 2, No. 2, March-April, 1979, pp. 119-122.
- [32] Marinescu, A. and Dumitrescu, D., "Optimal Low-Thrust Maneuvers Near the Libration Points," *Journal of Guidance and Control*, Vol. 2, No. 6, November-December, 1980, pp. 596-597.
- [33] Popescu, M., "Optimal Transfer from Collinear Libration Points with Limited Rotation Speed," *Journal of Guidance, Control, and Dynamics*, Vol. 12, No. 1, January-February, 1989, pp. 119-121.

- [34] Popescu, M., "Optimal Trajectories in the Transfer Problem of Space Vehicles from Lagrangian Collinear Points," Presented at the 42nd Congress of the International Astronautical Federation, IAF-91-343, Montreal, Canada, October, 1991.
- [35] Gingiss, A. J., "Navigation Analysis of Earth-Moon Libration Point Missions," Master's Thesis, Massachusetts Institute of Technology, The Charles Stark Draper Laboratory Report CSDL-T-1133, Cambridge, MA, June, 1992.
- [36] Szebehely, V., *Theory of Orbits: The Restricted Problem of Three Bodies*, Academic Press, 1967.
- [37] *The Astronomical Almanac*, U.S. Government Printing Office, Washington, DC, 1991.
- [38] Doyle, J. C., Glover, K., Khargonekar, P. P., and Francis, B. A., "State-Space Solutions to Standard  $\mathcal{H}_2$  and  $\mathcal{H}_\infty$  Control Problem", *IEEE Transactions on Automatic Control*, Vol. 34, No. 8, August 1989, pp. 831-847.
- [39] Dailey, R. L., "Lecture Notes for the Workshop on  $\mathcal{H}_\infty$  and  $\mu$  Methods for Robust Control", 1990 American Control Conference, San Diego, CA, May 1990.
- [40] Muller, Jr., E. S. and Kachmar, P. M., "The Apollo Rendezvous Navigation Filter Theory, Description and Performance," The Charles Stark Draper Laboratory, Cambridge, MA, R-649, June, 1970.
- [41] Gelb, A. (ed.), *Applied Optimal Estimation*, The M.I.T. Press, Cambridge, MA, 1974.

- [42] Potter, J. E., "Error Ellipsoids," The Massachusetts Institute of Technology Instrumentation Laboratory, Cambridge, MA, Space Guidance Analysis Memo 29, November, 1962.
- [43] Hitzl, D. L., "A Note on Equiprobability Ellipsoids," *The Journal of the Astronautical Sciences*, Vol. 40, No. 1, January-March, 1992, pp. 165-170.
- [44] "Onboard Navigation System Characteristics," NASA-JSC-14675, Rev. 1, December, 1981.
- [45] Laurie, R. J. and Sterzer, F., "Advanced Multipurpose Rendezvous Tracking System Study," NASA-CR-167706, June, 1982.

## Vita

Brian Leigh Jones was born on [REDACTED]

PII Redacted

[REDACTED]

Science in Aerospace Engineering degree from North Carolina State University and a commission in the United States Air Force. In December 1980, he earned a Master of Science in Aeronautical Engineering degree from the Air Force Institute of Technology. Subsequently, he was assigned to the National Aeronautics and Space Administration at Johnson Space Center, Houston, Texas, as a Space Shuttle mission controller. During this assignment, he participated in 16 missions making flight control recommendations during Space Shuttle trajectory operations. In June 1986, he reported to Edwards AFB, California, where one year later, he graduated from the United States Air Force Test Pilot School. Remaining at Edwards AFB, he was assigned to the F-15 Combined Test Force where he was responsible for the engineering planning, execution, data analysis and technical reporting of 24 avionics, armament and weapons system flight test programs for the F-15E Strike Eagle. In August 1990, he entered The University of Texas at Austin pursuing the Doctor of Philosophy degree.

PII Redacted

Permanent address: [REDACTED]  
[REDACTED]

This dissertation was typeset<sup>1</sup> with L<sup>A</sup>T<sub>E</sub>X by the author.

---

<sup>1</sup>L<sup>A</sup>T<sub>E</sub>X document preparation system was developed by Leslie Lamport as a special version of Donald Knuth's T<sub>E</sub>X program for computer typesetting. T<sub>E</sub>X is a trademark of the American Mathematical Society. The L<sup>A</sup>T<sub>E</sub>X macro package for The University of Texas at Austin dissertation format was written by Khe-Sing The.